

OCEAN

ENGINEERING

GROUP

A viscous/inviscid interactive approach and its
application to hydrofoils and propellers with
non-zero trailing edge thickness

Yulin Pan

August 2009

Report No. 09-4

**ENVIRONMENTAL AND WATER RESOURCES ENGINEERING
DEPARTMENT OF CIVIL, ARCHITECTURAL
AND ENVIRONMENTAL ENGINEERING
THE UNIVERSITY OF TEXAS AT AUSTIN**

Austin, TX 78712

Copyright
by
Yulin Pan
2009

**A viscous/inviscid interactive approach and its
application to wetted or cavitating hydrofoils and
propellers with non-zero trailing edge thickness**

APPROVED BY

SUPERVISING COMMITTEE:

Supervisor: _____
Spyros A. Kinnas

Reader: _____
Robert Moser

**A viscous/inviscid interactive approach and its
application to wetted or cavitating hydrofoils and
propellers with non-zero trailing edge thickness**

by

Yulin Pan, B.S.

THESIS

Presented to the Faculty of the Graduate School of

The University of Texas at Austin

in Partial Fulfillment

of the Requirements

for the Degree of

MASTER OF SCIENCE in Engineering

THE UNIVERSITY OF TEXAS AT AUSTIN

August 2009

Dedicated to family.

Acknowledgments

I wish to express my deep appreciation to my advisor, Professor Spyros A. Kinnas, for his continuous support and guidance throughout the first two years of my graduate study. I definitely have benefited greatly through working with him. Besides the insightful ideas in my research, he showed me the qualities a good researcher should have - perseverance, prudence, curiosity, creativity, etc. These things will help me greatly in the rest of my graduate study, and even future career. I also direct my gratitude to Professor Robert Moser, for his reviewing of this thesis and two valuable classes in fluid mechanics.

I am also very grateful to my friends in the Computational Hydrodynamics Laboratory. Their invaluable help in many aspects makes my life in Texas more memorable. I would especially thank Vimal Vinayan, Hong Sun and Lei He, for their tireless answering of my questions, and Sowmitra Singh for discussing problems in the class. In addition, I want to thank all my friends for their friendship and assistance.

Gratitude also goes to Bernie Boudreaux, Sally Boudreaux and everybody in the life group, for so many wonderful Friday nights full of joy. Your kindness makes Austin the second “home” for me. Special thanks goes to Allyson Li, for so much encouragement and support for my work.

Finally, I would like to take this chance to thank my family members.

Life is full of uncertainties. It was my family who keep supporting me over these years, including several most difficult situations in my life. I am greatly indebted to my parents - Zhigang Pan and Peixuan Ma. Without their love and understanding, I would never become the person who I am today.

This work is supported by Phase V of the “University/Navy/Industry Consortium on Cavitation of High Speed Propulsors” with the following members: American Bureau of Shipping, Daewoo Shipbuilding & Marine Engineering Co. Ltd., Kawasaki Heavy Industries Ltd., Naval Surface Warfare Center Carderock Division, Rolls-Royce Marine AB, Rolls-Royce Marine AS, Samsung Heavy Industries Co. Ltd., SSPA AB, VA Tech Escher Wyss GmbH, Wärtsilä Propulsion Netherlands BV, Wärtsilä Propulsion AS, Wärtsilä CME Zhenjiang Propeller Co. Ltd. and Wärtsilä Lips Defense S.A.S. Partial support for this research was also provided by the U.S. Office of Naval Research (contract N00014-07-1-0616).

A viscous/inviscid interactive approach and its application to wetted or cavitating hydrofoils and propellers with non-zero trailing edge thickness

Yulin Pan, M.S.E.

The University of Texas at Austin, 2009

Supervisor: Spyros A. Kinnas

Traditional boundary element methods (BEM) coupled with integral boundary layer solvers can efficiently model flows around hydrofoils and propellers with sharp trailing edges. However, numerical prediction of the performances of propellers with non-zero trailing edge thickness has long been a difficult problem, due to the flow separation behind the trailing edge. In the present work, a viscous/inviscid interactive (VII) approach is first applied to predict the performances of hydrofoils and propellers with non-zero trailing edge thickness. The emphasis has been put on developing VII BEM models for flow separation.

The investigation starts from a 2D hydrofoil. The current method uses an iterative scheme to find a non-lifting closing extension behind the finite trailing edge. Two kinds of schemes are applied for the iteration process respectively. (1) A flap extension with one or two degrees of freedom, running

in fully-wetted condition to find a non-lifting extension. (2) The extension is treated like a cavity surface, but with a non-constant cavity pressure distribution. The results from these schemes are compared with those from a commercial RANS Solver (Fluent). The correlation between the Fluent and BEM results shows that the current method (with both kinds of iteration schemes) gives results within reasonable accuracy, at a very small fraction of the computational effort.

Next, the current schemes using flap extensions are extended to 3D propeller flows. The 3D models are developed so that all the span-wise strips of the propeller satisfy similar conditions to those used in 2D. A propeller with significant non-zero trailing edge thickness is analyzed, using several 3D models, and the results are compared with existing experimental data.

Finally, the VII BEM solver is also applied to hydrofoils with partial-cavitation, and the results are compared with those from a RANS solver coupled with a mixture model.

Table of Contents

Acknowledgments	v
Abstract	vii
List of Tables	xii
List of Figures	xiii
Nomenclature	xvii
Chapter 1. Introduction	1
1.1 Motivation and Background	1
1.2 Objectives and Organization	3
Chapter 2. Literature and Method Review	5
2.1 Boundary Element Method	5
2.1.1 Governing equation	7
2.1.2 Boundary conditions	8
2.2 The 2D integral boundary layer analysis	8
2.3 The Viscous/Inviscid Flow Coupling	11
2.3.1 Modified Green's Formulation	12
2.3.2 The Coupling Algorithm	12
Chapter 3. Methodology and Results in 2D	14
3.1 Fluent analysis for a hydrofoil	14
3.2 Viscous/Inviscid interactive (VII) BEM approach	19
3.2.1 VII BEM Solver coupling with one degree of freedom it- eration method	19
3.2.2 VII BEM Solver coupling with two degrees of freedom iteration method	23

3.2.3	Cavity-like scheme	27
3.2.3.1	Mathematical Formulation	28
3.2.3.2	Results from Cavity-like Scheme	34
3.2.4	Correlation of all current methods with Fluent analysis .	38
3.2.5	Some other results for different angles of attacks	40
Chapter 4. Methodology and Results in 3D		43
4.1	Propeller Geometry	43
4.2	BEM-inviscid model	50
4.2.1	One degree of freedom model in 3D	50
4.2.2	Two degrees of freedom model in 3D	55
4.2.3	Solution scheme	58
4.2.4	Results and comparison	64
4.3	BEM-viscous model	68
4.3.1	A simple model	68
4.3.2	VII BEM Solver coupling with one degree of freedom model in 3D	71
4.4	Convergence study	82
4.4.1	Convergence contour for propeller A with modified blade sections	82
4.4.2	Convergence study of propeller A	85
4.4.2.1	Convergence study of propeller A with number of chord-wise elements	85
4.4.2.2	Convergence study of propeller A with number of span-wise elements	93
4.4.2.3	Convergence study of different lengths of extensions	95
Chapter 5. VII BEM Solver with application to partial-cavitating hydrofoils		99
5.1	Fluent simulation of partial cavitation	99
5.1.1	Description of Fluent cavitation model	99
5.1.2	Fluent setting	103
5.1.3	Results	106
5.2	VII BEM simulation	110

5.2.1	Inviscid solution	110
5.2.2	Viscous solution	114
5.2.2.1	Original viscous solution	114
5.2.2.2	Correction scheme I	116
5.2.2.3	Correction scheme II	120
5.2.2.4	Correction scheme III	122
5.2.3	Summary of all schemes	126
Chapter 6. Conclusions and recommendations		132
6.1	Conclusions	132
6.2	Recommendations	134
Bibliography		137
Vita		143

List of Tables

3.1	Numerical schemes used in Fluent simulation	15
3.2	Comparison of lifting force predicted by proposed methods and Fluent	39
3.3	Comparison of computational cost	39
4.1	K_T and K_Q by using different turbulent levels at $J = 0.75$. .	75
4.2	K_T and K_Q by using different numbers of chord-wise elements at $J = 0.75$	77
4.3	Computational cost for approaches in 3D	79
4.4	Convergence of K_T and K_Q with number of chord-wise elements at $J = 0.9$	88
4.5	Summary of K_T using different panels at $J = 0.75$ and $J = 0.9$	88
4.6	Convergence of K_T and K_Q with number of span-wise elements at $J = 0.9$	93
5.1	Spatial discretization in Fluent	105
5.2	Physical parameter used in the Fluent simulation	106

List of Figures

3.1	Computational domain and boundary conditions	15
3.2	Grid details near the hydrofoil and finite trailing edge (195104 elements in total)	16
3.3	Pressure distribution from Fluent; (a) on the hydrofoil (b) near the finite trailing edge	18
3.4	yplus on the hydrofoil	19
3.5	One degree of freedom closing extension behind the trailing edge	20
3.6	Comparison of results from the one degree of freedom iteration method and Fluent: (a) global result, (b) near the trailing edge	22
3.7	Two degrees of freedom closing extension behind the trailing edge	23
3.8	Comparison of results from the two degrees of freedom iteration method and Fluent: (a) global result, (b) near the trailing edge	25
3.9	Influence of extension length on C_p distribution	26
3.10	Definition of variables for cavity-like extension	29
3.11	Updated extension surface	32
3.12	Flowchart for cavity-like scheme	33
3.13	Viscous C_p distribution on the hydrofoil ($Ratio = -0.3$): (a) global result, (b) near the trailing edge	35
3.14	Influence of different values of $Ratio$ on inviscid pressure distribution, using the cavity-like scheme	36
3.15	Influence of different values of $Ratio$ on viscous pressure distribution, using the cavity-like scheme	37
3.16	Comparison of pressure distributions predicted by proposed methods and Fluent	38
3.17	Comparison of pressure distributions predicted by proposed methods and Fluent at 7 degrees angle of attack	41
3.18	Comparison of pressure distributions predicted by proposed methods and Fluent at 4 degrees angle of attack	42
4.1	The propeller A, with significant non-zero trailing edge thickness	44

4.2	Expanded view of some sections of propeller A	45
4.3	Two approximations used in the past	46
4.4	The way to close the non-zero trailing edge by using approximation 1	48
4.5	Current approach: original propeller with extensions determined by the last camber points	49
4.6	Inviscid pressure distributions on some sections for one DOF model in 3D at $J = 0.85$, span-wise positions of the strips: strip1: $r/R=0.1888$; strip5: $r/R=0.3552$; strip10: $r/R=0.5632$; strip15: $r/R=0.7712$; strip19: $r/R=0.9376$	54
4.7	Inviscid pressure distributions on some sections for two DOF model in 3D at $J = 0.9$, span-wise positions of the strips: strip1: $r/R=0.1977$; strip5: $r/R=0.4354$; strip9: $r/R=0.6731$; strip13: $r/R=0.9109$	57
4.8	The numerical derivatives $\frac{\partial \Delta p_n}{\partial y_{10}}$ by using different sizes of Δy_{10}	59
4.9	Two parts of forces and moments	62
4.10	A flowchart for the whole solution process	63
4.11	Results from one DOF inviscid model: (a) K_T , (b) K_Q	66
4.12	Pressure distributions on two arbitrary strips from approximation 1 at $J = 0.85$, span-wise positions of the strips: strip5: $r/R=0.3552$; strip15: 0.7712	67
4.13	Results predicted by the simple viscous model: (a) K_T , (b) K_Q	69
4.14	Pressure distributions on two arbitrary strips by applying XFOIL on top of one DOF inv model (non-lift), $J = 0.85$, 80×20 panels are used, span-wise positions of the strips: strip1: $r/R=0.1977$; strip13: $r/R=0.9109$	70
4.15	Pressure distributions by using VII BEM Solver coupling with non-lift condition at $J = 0.85$, 80×14 panels are used, span-wise positions of the strips: strip1: $r/R=0.1977$; strip5: $r/R=0.3552$; strip9: $r/R=0.6731$; strip13: $r/R=0.9109$	73
4.16	K_T and K_Q predicted by VII BEM Solver coupling with non-lift condition	74
4.17	Pressure distributions on one arbitrary strip of propeller A by using different turbulent levels at $J = 0.75$	76
4.18	Pressure distributions on one arbitrary strip of propeller A by using different numbers of chord-wise elements at $J = 0.75$	78
4.19	K_T and K_Q predicted by all discussed approaches	81

4.20	Error of K_T by using NACA00 sections at $J = 0.9$, modified Propeller A: (a) absolute error, (b) percentage error	83
4.21	Error of K_Q by using NACA00 sections at $J = 0.9$, modified Propeller A: (a) absolute error, (b) percentage error	84
4.22	Convergence of base pressures with number of chord-wise elements at $J = 0.9$, Propeller A	86
4.23	Convergence of pressure distributions on three arbitrary strips with number of chord-wise elements at $J = 0.9$, propeller A	89
4.24	Convergence study of K_T due to pressure distributions on pressure and suction sides at $J = 0.9$, Propeller A	91
4.25	Convergence study of K_T due to base pressure at $J = 0.9$, Propeller A	91
4.26	Comparison of two parts of K_T at the first few strips near the hub at $J = 0.9$, Propeller A	92
4.27	Convergence of base pressures with number of span-wise elements at $J = 0.9$	94
4.28	Pressure distributions on five arbitrary strips of propeller A by using different lengths of extensions at $J = 0.75$, Propeller A, span-wise positions of Propeller A: strip1: $r/R=0.1888$; strip5: $r/R=0.3552$; strip10: $r/R=0.5632$; strip15: $r/R=0.7712$; strip20: $r/R=0.9792$	98
4.29	K_T and K_Q by using different lengths of extensions at $J = 0.75$, Propeller A	98
5.1	Computational domain and boundary conditions	104
5.2	Grid near the trailing edge and leading edge: (a) leading edge, (b) trailing edge	105
5.3	Time variance of lifting coefficient for $\sigma = 0.955$: (a) global view, (b) “quasi-steady” state	107
5.4	y^+ of the first grid point near the foil	108
5.5	Pressure distribution near the cavity bubble predicted by Fluent mixture model for $\sigma = 0.955$: (a) global view of pressure distribution with contour flood, (b) local view of pressure distribution inside and outside the cavity bubble with contour lines, The units of both are Pascal.	109
5.6	Cavity surface predicted by BEM solver and volume fraction predicted by Fluent for $\sigma = 0.955$	112

5.7	Pressure distributions predicted by BEM (inviscid) and Fluent, the result of “BEM-inviscid” is obtained by running CAV2DBL (inviscid) on the compound foil obtained from PCPAN	113
5.8	Viscous solution by applying XFOIL on top of the compound foil directly, the result of BEM/XFOIL-original is obtained by running CAV2DBL (viscous) on the compound foil obtained from PCPAN	115
5.9	Viscous pressure distribution by applying correction I (Results from first and second iterations are shown)	119
5.10	Mixture velocity near the cavity predicted by Fluent mixture model	120
5.11	A hydrofoil with sheet cavitation (The picture is taken in University of Tokyo and can be found online at http://www.fluidlab.naoe.t.u-tokyo.ac.jp/Research/CavPictures/index.html.en)	121
5.12	Viscous pressure distribution by applying correction II	123
5.13	Treatment of boundary layer in Correction scheme III	124
5.14	Viscous pressure distribution by applying correction III	125
5.15	Summary of pressure distributions predicted by all schemes for $\sigma = 0.955$	128
5.16	Pressure distribution near the cavity bubble predicted by Fluent mixture model for $\sigma = 0.754$: (a) global view of pressure distribution with contour flood, (b) local view of pressure distribution inside and outside the cavity bubble with contour lines, The units of both are Pascal.	129
5.17	Cavity surface predicted by BEM solver and volume fraction predicted by Fluent for $\sigma = 0.754$	130
5.18	Summary of pressure distributions predicted by all schemes for $\sigma = 0.754$	131
6.1	Separation zone for backing condition	136

Nomenclature

Latin Symbols

C_τ	shear stress coefficient $C_\tau = \tau_{max}/(\rho U^2)$
C_f	skin-friction coefficient $C_f = \tau_{wall}/(0.5\rho U^2)$
C_p	pressure coefficient, $C_p = (P - P_o)/(0.5\rho n^2 D^2)$
D	propeller diameter, $D = 2R$
f_{max}/C	maximum camber to chord ratio
G	Green's function
h	cavity height
H	shape factor, $H = \delta^*/\theta$
J	advance ratio based on V_s , $J = V_s/(nD)$
K_Q	torque coefficient, $K_Q = Q/(\rho n^2 D^5)$
K_T	thrust coefficient, $K_T = T/(\rho n^2 D^4)$
n	propeller rotational frequency (rev/s)
P	pressure
P_o	pressure far Upstream, at the propeller axis
P_v	vapor pressure of water

\vec{q}	total velocity
\vec{q}_{in}	local inflow velocity (in the propeller fixed system)
\vec{q}_w	wake inflow velocity (in the ship fixed system)
Q	propeller torque
R	propeller radius
Re	Reynolds number
$\vec{s}, \vec{v}, \vec{n}$	non-orthogonal unit vectors along the local grid directions
S_B	blade surface
S_{WB}	wetted portion of blade surface
S_W	wake surface
t	time
T	propeller thrust
T_{max}/C	maximum thickness to chord ratio
V_s	ship speed
u_e	boundary layer edge velocity
u_τ	wall shear velocity, $u_\tau = \sqrt{\tau_{wall}/\rho}$
x, y, z	propeller fixed coordinates
y^+	non-dimensional wall distance, $y^+ = \frac{u_\tau y}{\nu}$

Greek Symbols

α	angle of attack
δ^*	displacement thickness, $\delta^* = \int (1 - \frac{u}{U_e}) dz$
Δt	time step size
ω	propeller angular velocity
ν	kinematic viscosity of water
ϕ	perturbation potential
Φ	total potential
ρ	fluid density
σ	cavitation number, $\sigma = \frac{p_\infty - p_v}{(1/2)\rho v^2}$
θ	momentum thickness, $\theta = \int \frac{u}{U_e} (1 - \frac{u}{U_e}) dz$

Superscripts

2D	two dimensional
3D	three dimensional
BEM	boundary element method
CPU	central processing unit
MIT	Massachusetts Institute of Technology
NACA	National Advisory Committee for Aeronautics
RANS	Reynolds-averaged Navier Stokes
VII	viscous/inviscid interactive

Computer Program Names

CAV2DBL	cavitating 2-dimensional with boundary layer
Fluent	A commercial RANS solver
PCPAN	2D BEM solver for partially cavitating hydrofoil flow
PROPCAV	cavitating propeller potential flow solver based on BEM
XFOIL	2D integral boundary layer analysis code

Chapter 1

Introduction

1.1 Motivation and Background

Boundary element method (BEM) has long been used as an efficient tool for modeling flows around propellers with sharp trailing edges. Coupled with an integral boundary layer solver (XFOIL), viscous effects near the propeller surface can be included. Numerical tools based on this method, such as CAV2DBL and PROPCAV coupled with XFOIL, have been found to be robust in predicting the performance of fully-wetted or cavitating hydrofoils and propellers. However, real propellers always have finite trailing edge thickness due to many reasons. For example, (1) At higher propeller radius, anti-singing edges are normally applied, which results in a small finite trailing edge thickness; (2) At lower propeller radius, relatively thick or rounded trailing edges are used due to structural reasons. Sharp trailing edges easily get damaged. No matter what the reason, this feature generates a flow separation zone behind the finite trailing edge, which makes it difficult to apply boundary element method. Other viscous flow solvers, such as RANS and LES, are more suitable for this type of open trailing edges. (For example, [Rhee et al. 2005] applies a RANS solver to a cavitating propeller with closed sections.) However, A fine grid needs to be built downstream of the trailing edge so that unsteady vortex

shedding at the trailing edge can be modeled. These methods, thus, become very expensive and time-consuming to apply to propeller design. Therefore, it is essential to develop a numerical tool based on BEM, which predicts the performances of hydrofoils and propellers with non-zero trailing edge thickness.

Experimental evidence [Russel 1958] shows that the separated zone behind the finite trailing edge forms a closed cavity that separates from the potential flow around the propeller. [Kudo and Ukon 1994] have developed a 3D vortex-lattice lifting surface method which solves the steady problem of cavitating propeller with a flow separation zone behind. Their model assumed the base pressure over the separated zone to be constant and equal to the vapor pressure. Furthermore, [Kudo and Kinnas 1995] studied the influence of the length of the separated zone, which affects the pressure and cavity length near the blade trailing edge under fully-wetted and partially-cavitating conditions. Later, [Young and Kinnas 2003b] developed a boundary element method to model supercavitating propeller flows using the same assumption. They used a closing rigid extension behind the finite trailing edge and treated the separation zone as an additional cavitation bubble. Their results showed that the geometry of the closing zone does not affect the solution as long as it is inside the supercavity bubble. However, the assumption used in these methods is not accurate enough. Also, these methods fail to apply to fully-wetted hydrofoil and propeller flows.

1.2 Objectives and Organization

The objective of the present work is to develop more rigorous explanations on the extensions, which are used for approximating the flow separation zone. Specifically, the mean closing streamlines after the finite trailing edge are represented by the rigid extension. In 2D, the results from these methods are validated by comparing with Fluent results. These methods are then applied in three dimensions, with the same assumptions applied on each strip of the propeller blade. The results are compared with experimental data in 3D.

The thesis is organized into five chapters.

Chapter 1 gives the motivation, background and objectives of this study. A review of the previous study is also included.

Chapter 2 presents a summary of literature review on boundary element method, viscous solver (XFOIL), and the coupling algorithm. The explanation of the viscous solver and the coupling algorithm is taken from [Sun 2008]

In Chapter 3, a systematic 2D study of a hydrofoil with non-zero trailing edge thickness is presented. The mathematical formulation and numerical implementation of current models are given. The validation of these models are tested by comparing the results with those from Fluent.

In Chapter 4, the models developed in 2D are extended to 3D propeller flows. The results are compared with experimental measurements and extensive convergence studies are presented.

In Chapter 5, The VII BEM solver with application to partial-cavitating

hydrofoil is discussed. The results are compared with those from a RANS mixture model.

Chapter 6 summarizes the present work and proposes the recommendations for future research.

Chapter 2

Literature and Method Review

In this chapter, a low-order potential based boundary element method, which is used to model flows around hydrofoils and propellers, is reviewed first. The theory of boundary layer analysis (XFOIL), via which the viscous effects are included, is then summarized. At last, the coupling algorithm between the inviscid and viscous solution is reviewed.

2.1 Boundary Element Method

Boundary element method has proved to be very effective in solving potential flows around hydrofoils and propellers. The perturbation potential based panel method was introduced for the analysis of non-cavitating propeller performance in steady flow by [Lee 1987, Kerwin et al. 1987]. Later, [Kinnas and Fine 1992; 1993, Fine and Kinnas 1993] developed several BEM cavitation models for analyzing flows around cavitating hydrofoils and cavitating propellers. This method was named PROPCAV. Over the years, improvements were made and new features were included in PROPCAV. The latest version is able to deal with partial cavitating, super cavitating, and surface-piecing propellers [Young and Kinnas 2003a], ducted propellers [Lee and Kinnas 2006],

tunnel effects [Lee and Kinnas 2005], tip vortex cavitation and unsteady wake alignment [Lee and Kinnas 2004] and inclusion of viscous effects via coupling with a boundary layer solver [Sun and Kinnas 2008].

The governing equations and boundary conditions in the case of non-cavitating hydrofoils and open propellers are summarized as follows for the sake of explanation. For the propeller case, a blade fixed coordinate system (x, y, z) , which rotates with the propeller, is used. Therefore, the inflow velocity \vec{q}_{in} with respect to the propeller can be expressed as the sum of the inflow wake velocity, \vec{q}_w , and the propeller's angular velocity $\vec{\omega}$, at a given location \vec{x} :

$$\vec{q}_{in}(x, y, z, t) = \vec{q}_w(x, r, \theta_B - \omega t) + \vec{\omega} \times \vec{x} \quad (2.1)$$

where $r = \sqrt{y^2 + z^2}$, $\theta_B = \arctan(z/y)$, and $\vec{x} = (x, y, z)$.

With the assumption that the resulting flow is incompressible, inviscid and irrotational, the total velocity $\vec{q}(x, y, z, t)$ at any point in the fluid domain can be expressed as follows:

$$\vec{q}(x, y, z, t) = \vec{q}_{in}(x, y, z, t) + \nabla\phi(x, y, z, t) \quad (2.2)$$

where $\phi(x, y, z, t)$ is the perturbation potential, which satisfies the Laplace's equation, i.e. the governing equation for incompressible potential flow:

$$\nabla^2\phi = 0 \quad (2.3)$$

The Green's third identity is next applied to solve the Laplace's equation for the perturbation potential in the flow domain.

2.1.1 Governing equation

The perturbation potential, $\phi(x, y, z, t)$, at any point $p(x, y, z)$ located on the wetted body (hydrofoil or propeller blade) surface, $S_{WB(t)}$, must satisfy Green's third identity:

$$\begin{aligned} \frac{\phi(\vec{x}, t)}{2} = & \int_{S_{WB(t)}} \left[-\phi_q(\vec{x}, t) \frac{\partial G(p; q)}{\partial n_q(t)} + G(p; q) \frac{\partial \phi_q(\vec{x}, t)}{\partial n_q(t)} \right] dS \\ & - \int_{S_{W(t)}} \Delta \phi_W(\vec{x}, t) \frac{\partial G(p; q)}{\partial n_q(t)} dS \end{aligned} \quad (2.4)$$

where q and p correspond to the variable point and the field point, respectively. $G(p; q)$ is the Green's function. For the 3D propeller case, $G(p; q) = -\frac{1}{4\pi R(p; q)}$; For the 2D hydrofoil case, $G(p; q) = \frac{\ln r}{2\pi}$, with $R(p; q)$ being the distance between the field point p and the variable point q . \vec{n}_q is the unit vector normal to the integration surface, with the positive direction pointing into the fluid domain. $S_{W(t)}$ is the trailing wake sheet of the propeller blade or hydrofoil. $\Delta \phi_W$ is the potential jump across the trailing wake sheet.

Equation (2.4) implies that the solution potential $\phi(\vec{x}, t)$ on the blade or hydrofoil surfaces can be expressed by distributing sources and dipoles over the wetted surface, and dipoles only on the trailing wake surfaces behind the propeller blade or hydrofoil.

2.1.2 Boundary conditions

In order to uniquely determine the solution of Equation (2.4), appropriate boundary conditions have to be applied on the exact flow domain.

1. **Kinematic boundary condition:** The flow on the wetted blade or hydrofoil is tangent to the wetted body surfaces.

$$\frac{\partial \phi}{\partial n} = -\vec{q}_{in}(x, y, z, t) \cdot \vec{n} \quad (2.5)$$

2. **Kutta condition:** The flow velocity at the trailing edge of the blade or hydrofoil is finite.

$$|\nabla \phi| < \infty \quad (2.6)$$

For the 2D hydrofoil case, a Morino's Kutta condition is applied at the trailing edge; For the 3D propeller case, an iterative pressure Kutta condition is applied at the blade trailing edge to ensure that the pressures on the suction and pressure sides are equal.[Kerwin et al. 1987, Kinnas and Hsin 1992]

3. **Condition at infinity:** The flow velocity vanishes at the far field.

$$\nabla \phi \rightarrow 0 \quad (2.7)$$

The solutions, ϕ on the wetted surface can then be determined by solving Equation (2.4) together with the boundary conditions (2.5), (2.6) and (2.7).

2.2 The 2D integral boundary layer analysis

According to Jessup's work [Jessup 1989], the viscous flow in the boundary layer of the propeller blade can be assumed to develop only along the

stream-wise direction. The growth of the boundary layer in the cross flow direction is negligible. In this study, Drela's 2D integral boundary layer analysis code (XFOIL) is used to solve the boundary layer flow along the stream-wise direction [Drela 1989]. XFOIL employs a two-equation lagged dissipation integral method including the treatment of laminar and turbulent boundary layers, and is able to represent accurately flows with limited separation regions. The prediction of transition is based on an e^N -type amplification formulation. Detailed information of this method can be found in [Drela 1989]. The boundary layer equations are summarized here for the sake of completeness.

For a given distribution of the boundary layer edge velocity U_e , the boundary layer parameters can be determined by solving the momentum integral equation (2.8) and the kinetic energy shape factor equation (2.9) with a third closure equation (2.10) or (2.11)

Momentum Equation

$$\frac{d\theta}{ds} + (2 + H)\frac{\theta}{U_e}\frac{dU_e}{ds} = \frac{C_f}{2} \quad (2.8)$$

Kinetic Energy Equation

$$\theta\frac{dH^*}{ds} + [2H^{**} + H^*(1 - H)]\frac{\theta}{U_e}\frac{dU_e}{ds} = 2C_D - H^*\frac{C_f}{2} \quad (2.9)$$

Turbulent Closure

$$\frac{\delta}{C_\tau}\frac{dC_\tau}{ds} = 5.6[C_{\tau EQ}^{1/2} - C_\tau^{1/2}] + 2\delta \times \left\{ \frac{4}{3\delta^*}\left[\frac{C_f}{2} - \left(\frac{H_k - 1}{6.7H_k}\right)^2\right] - \frac{1}{U_e}\frac{dU_e}{ds} \right\} \quad (2.10)$$

Equation (2.10) is the rate equation for the maximum shear stress coefficient C_τ , and is used when the viscous flow has transitioned to turbulent

flow. In laminar regions, a rate equation (2.11), which models the growth of the amplitude \tilde{n} of the most amplified Tollmien-Schlichting wave, is used instead.

$$\frac{d\tilde{n}}{ds} = \frac{d\tilde{n}(H_k)}{dR_{e\theta}} \frac{dR_{e\theta}(H_k, \theta)}{ds} \quad (2.11)$$

The empirical relation $d\tilde{n}(H_k)/dR_{e\theta}$ is a correlation of spatial growth rates computed from solutions to Orr-Sommerfeld equation, and $dR_{e\theta}(H_k, \theta)/ds$ is obtained from the properties of Falkner-Scan profile family. The transition point is defined by the location where \tilde{n} reaches a user-specified critical value \tilde{n}_{crit} . The parameter in practice is used to represent the background disturbance level.

Equation (2.8) and Equation (2.9) represent momentum conservation and kinetic energy along the stream-wise direction. s is the stream-wise coordinate, $\delta^* = \int (1 - \frac{u}{U_e}) dz$ is the displacement thickness. and $\theta = \int \frac{u}{U_e} (1 - \frac{u}{U_e}) dz$ is the momentum thickness, where z is the vertical distance normal to the blade. $C_f = \frac{\tau_{wall}}{0.5\rho U_e^2}$ is the friction coefficient, and $C_f = 0$ is enforced in the wake. Definition of the momentum thickness shape factor H , the kinetic energy shape factor H^* , the density shape factor H^{**} , the dissipation coefficient C_D , the shear stress coefficient $C_{\tau EQ}$, the kinematic shape factor H_k and the momentum thickness Reynolds number $R_{e\theta}$ can be found in [Sun 2008].

Three primary variables are chosen for the above boundary layer governing equations: the mass defect m , the momentum thickness θ , and the amplitude growth rate \tilde{n} for the laminar regions or the square root of the maximum shear stress coefficient $C_\tau^{1/2}$. The mass defect m is defined as the

product of edge velocity U_e and the mass displacement thickness δ^* ,

$$m = U_e \delta^* \tag{2.12}$$

For laminar flow, Equations (2.8) and (2.9) are closed with Equation (2.11) to solve for m , θ and \tilde{n} . For turbulent flow, Equations (2.8), (2.9) and (2.10) are solved for m , θ and C_τ

2.3 The Viscous/Inviscid Flow Coupling

The coupling of the outer inviscid flow and inner boundary layer flow over the propeller blade is based on the strip theory assumption [Coney 1989, Hufford et al. 1994]. The developed boundary layers are assumed to be two dimensional along strips of the propeller blade, and the boundary layer in the cross flow direction is ignored. According to [Groves and Chang 1984, Jessup 1989], these strips can be assumed to be along the constant radial direction of the propeller blade.

The inviscid model (PROPCAV) and the 2D integral boundary layer analysis (XFOIL) are strongly coupled along these blade strips through the wall transpiration model. In the wall transpiration model, "blowing" sources which represent the viscosity effects are added to the panels on the blade and wake surface. The effect of these "blowing" sources is to replace the potential flow away from the body, and to create a component of velocity normal to the body. [Lighthill 2006, Nishida and Drela 1995]

Strength of "blowing" source $\hat{\sigma}$ is related to the rate of growth of the

boundary layer, and defined as:

$$\hat{\sigma} = \frac{dm}{ds} = \frac{d(U_e \delta^*)}{ds} \quad (2.13)$$

where s is the local coordinate along each constant radial strip, U_e is the velocity at the edge of the viscous boundary layer, and δ^* is the displacement thickness.

2.3.1 Modified Green's Formulation

The outer flow, including the viscous boundary layer effects, can be represented by adding the "blowing" sources to the Green's third identity, Equation (2.4):

$$\begin{aligned} \frac{\phi(\vec{x}, t)}{2} = & \int_{S_{WB(t)}} \left[-\phi_q(\vec{x}, t) \frac{\partial G(p; q)}{\partial n_q(t)} + G(p; q) \frac{\partial \phi_q(\vec{x}, t)}{\partial n_q(t)} \right] dS \\ & - \int_{S_W(t)} \Delta \phi_W(\vec{x}, t) \frac{\partial G(p; q)}{\partial n_q(t)} dS + \int_{S_{WB(t)} \cup S_W(t)} \hat{\sigma} G(p; q) dS \end{aligned} \quad (2.14)$$

In current approach, this equation is applied in 2D along each strip and is used to develop the velocity correction equation (2.15). [Kinnas et al. 1994] Both the perturbation potential ϕ and the "blowing" source strength $\hat{\sigma}$ in Equation (2.14) are unknown and to be solved by coupling the potential and boundary layer equations.

2.3.2 The Coupling Algorithm

The integral boundary layer equations are coupled with the inviscid solution through the edge velocity of the boundary layer at each blade strip.

According to [Drela 1989], the edge velocity can be expressed in terms of the known inviscid component and a correction involving the unknown blowing sources through the mass defect:

$$U_e = U_e^{inv} + \mathfrak{S}\{m\} = U_e^{inv} + \mathfrak{S}\{U_e\delta^*\} \quad (2.15)$$

where U_e is velocity at the edge of the boundary layer along each blade strip, U_e^{inv} is the inviscid component of the edge velocity. $m = U_e\delta^*$ is the mass defect term, and \mathfrak{S} is a geometry dependent operator, which can be found in [Sun 2008]

Equation (2.15) gives the solution to the potential flow for any distribution of mass defect on the blade and wake. The system of equations is elliptic in nature because of the global influence of the mass defect m on the edge velocity U_e . The solution can be found using a Newton iterative solver [Drela 1989]. For a given distribution of U_e , the mass defect term m and the momentum thickness θ can be determined from the boundary layer equations. In the first iteration, the edge velocity distribution from the inviscid solution U_e^{inv} is used as the given U_e to solve the boundary layer equations. Once the mass defect term m is obtained, U_e will be updated via Equation (2.15), and then the boundary layer equations are solved again. The process iterates until convergence is achieved.

Chapter 3

Methodology and Results in 2D

3.1 Fluent analysis for a hydrofoil

The flow around a 2D NACA00 hydrofoil ($f_{max}/c = 2\%$; $T_{max}/C = 4\%$), with a vertical cut at 90% chord length (treated as a finite trailing edge) is modeled in Fluent. A fine grid is built around the hydrofoil, especially near the finite trailing edge (thickness = 0.9% of chord length), as shown in Figure 3.2. The Reynolds number is chosen as 10^7 and 5 degrees angle of attack is used in this case.

The details of numerical schemes used in Fluent simulation are listed in Table 3.1, and Figure 3.1 shows the computational domain with the boundary conditions. Both steady and unsteady cases are run. The unsteady results are time-averaged in a vortex shedding period, and are found not to be too different from the steady results. The reason that the unsteadiness is not that important is that the vortex shedding is not very strong behind a small finite trailing edge.

Table 3.1: Numerical schemes used in Fluent simulation

Turbulence modeling	Reynolds Stress Model (RSM)
Near wall treatment	Standard Wall Function
Unsteady formulation	First order implicit in time
Discretization of momentum, turbulent kinetic energy, turbulent dissipation rate and Reynolds stresses	Second order upwind
Discretization of pressure	Standard
Pressure-velocity coupling	SIMPLE
Residuals	all at 10^{-6}

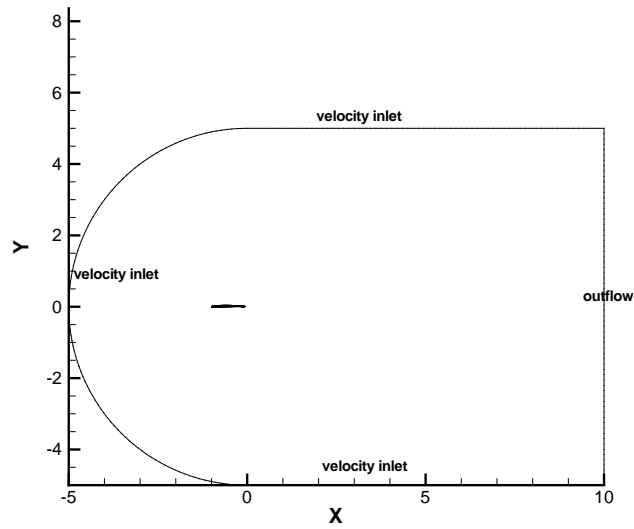


Figure 3.1: Computational domain and boundary conditions

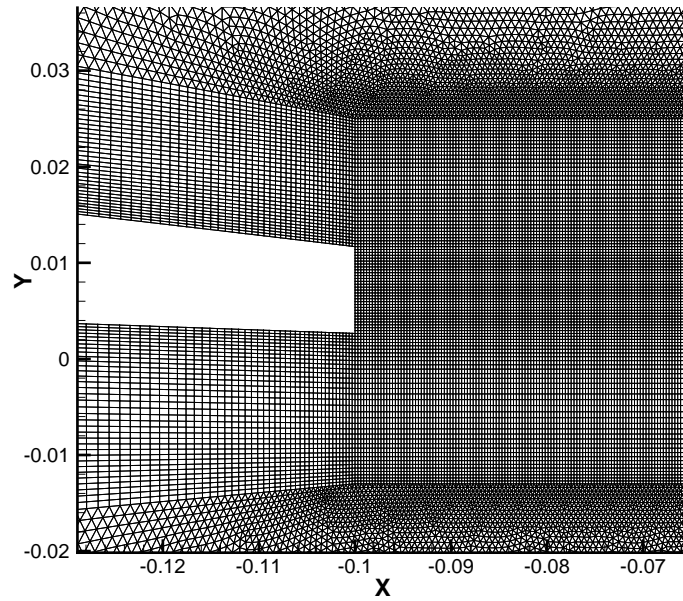
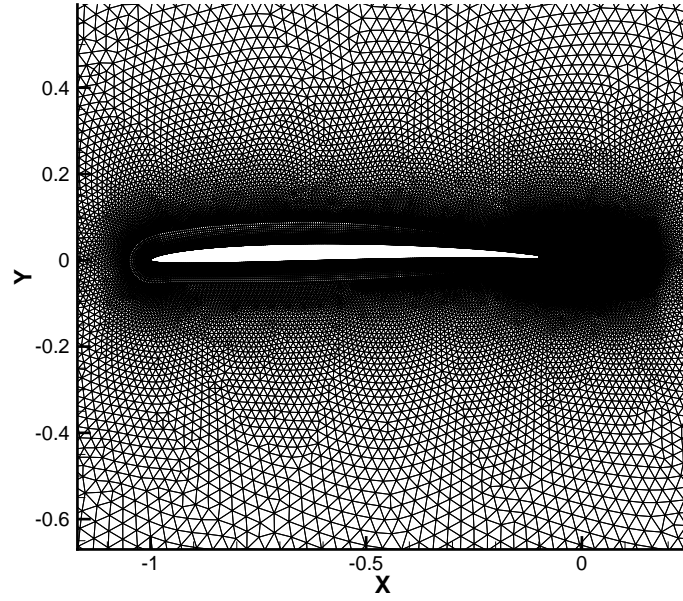


Figure 3.2: Grid details near the hydrofoil and finite trailing edge (195104 elements in total)

The pressure distributions on the hydrofoil and near the trailing edge are shown in Figure 3.3. Figure 3.3(a) shows that the pressure distribution on the upper side and lower side closes at the finite trailing edge. And Figure 3.3(a) shows that the pressures on the two sides of the surfaces of the separation zone does not change much in y direction, which excludes the lift on the separation zone. These features of pressure distribution provide the basis of the iteration process coupled in the viscous/inviscid interactive (VII) BEM approach. The closing extension used in the BEM Solver is basically an approximation of the separation zone.

As the end of the section of Fluent analysis, the y^+ of the first grid point near the hydrofoil is plotted in Figure 3.4. Most of the values fall in a reasonable region for standard wall function. Specifically, [Fluent 2007] suggests that the wall y^+ value should be close to the lower bound of the log-law region ($y^+ \approx 30$) for standard ‘wall functions.

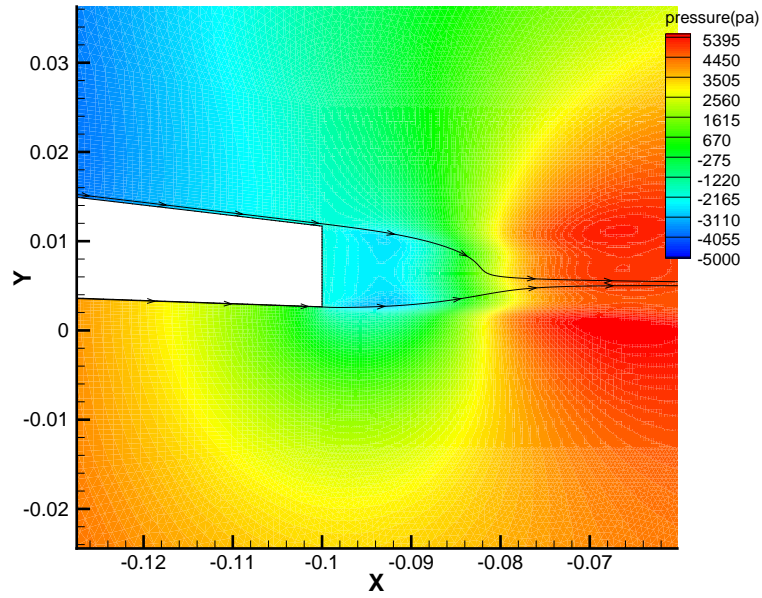
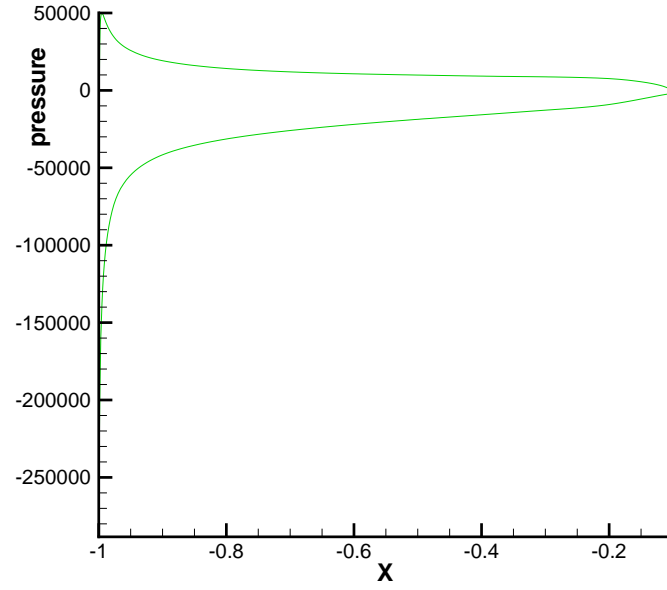


Figure 3.3: Pressure distribution from Fluent; (a) on the hydrofoil (b) near the finite trailing edge

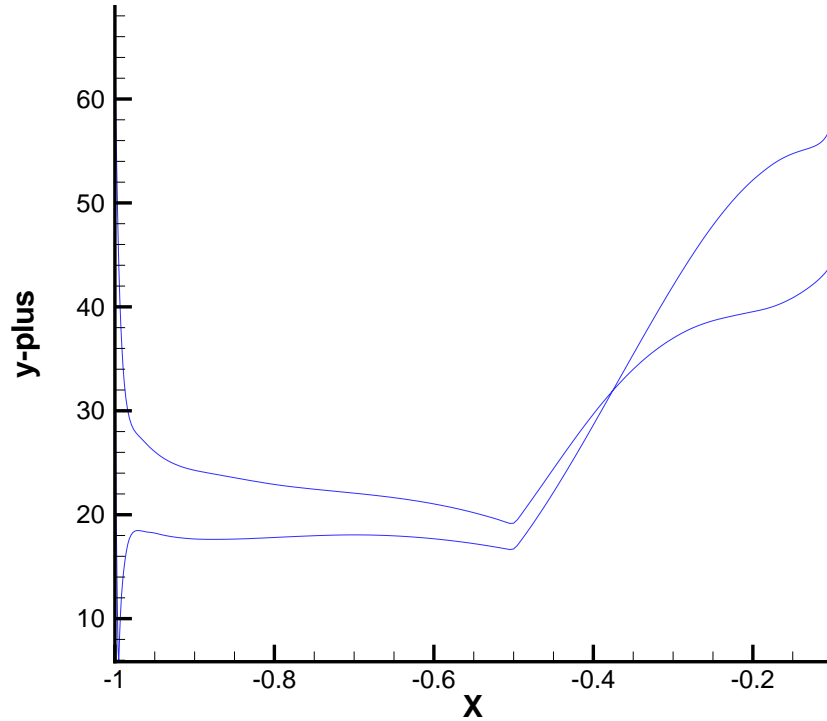


Figure 3.4: yplus on the hydrofoil

3.2 Viscous/Inviscid interactive (VII) BEM approach

3.2.1 VII BEM Solver coupling with one degree of freedom iteration method

Consider the same hydrofoil used in the Fluent analysis. A closing extension of 10% of the chord length is added behind the trailing edge and the last camber point on the extension is chosen as the control point (one degree of freedom) to control the geometry of the extension. The whole extension

is generated by interpolation of the original foil and the last point on the extension. By moving the last point up and down, the extension moves like a flapping tail, as shown in Figure 3.5. For the initial solution, the control point

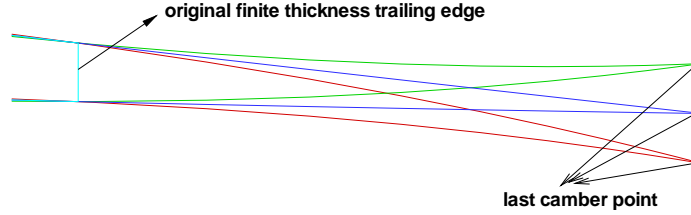


Figure 3.5: One degree of freedom closing extension behind the trailing edge

is set at an arbitrary vertical position. At each iteration, CAV2DBL (a 2D VII BEM Solver) is used to solve for the pressure distribution on the hydrofoil. This loop continues until a certain convergence condition is satisfied. There are two choices of the convergence conditions: (1) Non-lifting condition: The lifting force on the extension vanishes. (2) Pressure equivalence condition: The pressures at the two sides of the finite trailing edge are equal to each other. (Refer to Figure 3.3(a)). The Newton-Secant scheme is used to update the position of the control point at each iteration.

For this case, the convergence criterion is set as $C_L < 10e - 7$ ($C_L = \frac{Lift}{0.5 \cdot \rho \cdot U^2 \cdot chord}$) or $\Delta C_p < 10e - 5$ (The non-dimensional pressure C_p is defined as $C_p = \frac{pressure}{0.5 \cdot \rho \cdot U^2}$), It takes five iterations for non-lifting condition to converge and four iterations for pressure equivalence condition to converge, respectively.

The pressure distribution on the hydrofoil (by using both conditions)

is shown in Figure 3.6, with the comparison with Fluent result.

With sufficient grid resolution, the RANS solver is supposed to model the flow separation with greater accuracy. Therefore, in this comparison, the Fluent result is considered as the “correct” result. For the front part of the hydrofoil, the correlation of pressure distribution is good, with only a small difference. Some discrepancy exists near the actual trailing edge for both conditions, but it can be found that the converged results are much better than the initial solution for an arbitrary extension. (Note that in Figure 3.6, $x = 0.9$ is the position of the actual trailing edge.)

However, the non-lifting condition and pressure equivalence condition cannot be satisfied simultaneously in one degree of freedom iteration method. Both of them have some deficiency when applied separately. Therefore, it is necessary to develop a two degrees of freedom iteration method, in which both conditions can be satisfied simultaneously. (Two unknowns are needed for satisfying two conditions simultaneously.)

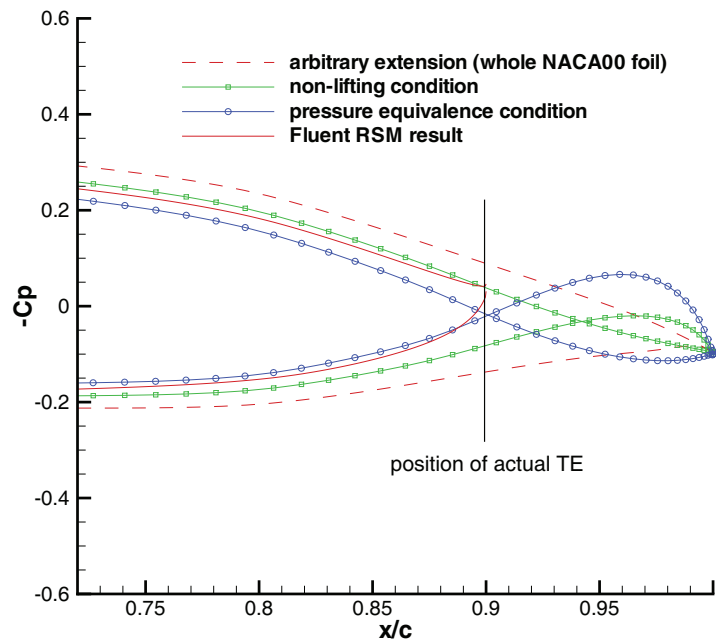
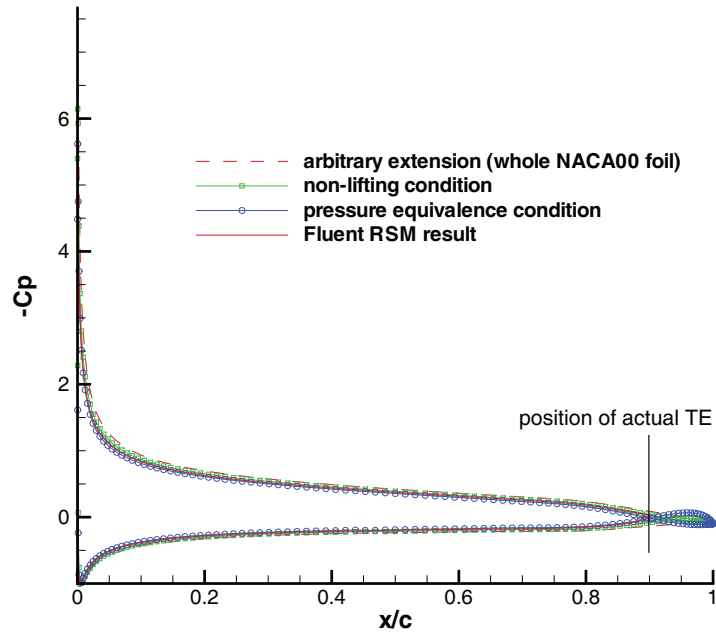


Figure 3.6: Comparison of results from the one degree of freedom iteration method and Fluent: (a) global result, (b) near the trailing edge

3.2.2 VII BEM Solver coupling with two degrees of freedom iteration method

Instead of controlling the extension geometry by using only the last camber point, two camber points on the extension are chosen as the control points (two degrees of freedom). In this case, the two points are set at $x=0.93$ and $x=1$, as shown in Figure 3.7. At the end of the iteration process, the two conditions used in one degree of freedom iteration method can be satisfied simultaneously. A Two-equation Newton-Raphson scheme is used to update the positions of the two control points after each iteration. In this scheme, we

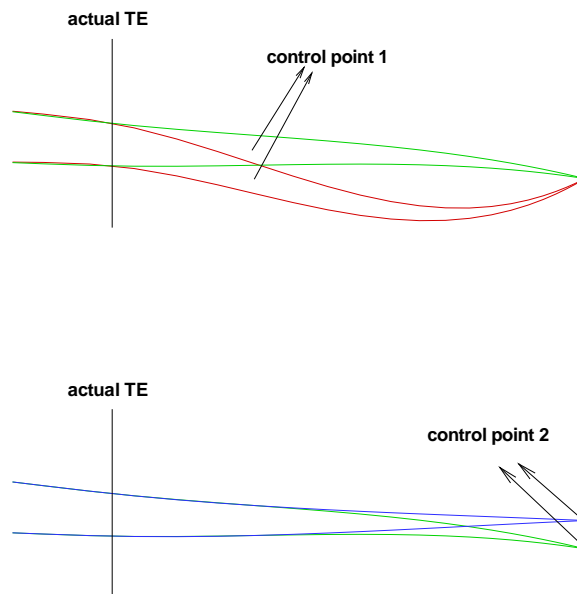


Figure 3.7: Two degrees of freedom closing extension behind the trailing edge

have two unknowns. So the two equations $C_L(y_1, y_2) = 0$ and $\Delta p(y_1, y_2) = 0$ can be satisfied simultaneously. For this case, the convergence criterion is set as $C_L < 10e-5$ and $\Delta C_p < 10e-3$, and it takes four iterations for the scheme to converge.

The pressure distribution on the hydrofoil is shown in Figure 3.8, with the comparison with Fluent result.

As shown in the figure, both conditions used in the one degree of freedom iteration method are satisfied. For an arbitrary extension, it affects not only the pressure distribution near the trailing edge, but also the global result. The improvement obtained by applying the two degrees of freedom iteration method is significant because it corrects the global result, with only a small discrepancy from the Fluent result near the trailing edge. The correction of the global result is important in evaluation of the lifting force of the whole hydrofoil.

The effect of extension length on pressure distribution is studied and Figure 3.9 shows that its influence to pressure distribution in the front of the trailing edge is negligible. This feature is useful because it allows us to use an extension of arbitrary length within a reasonable range when applying this scheme.

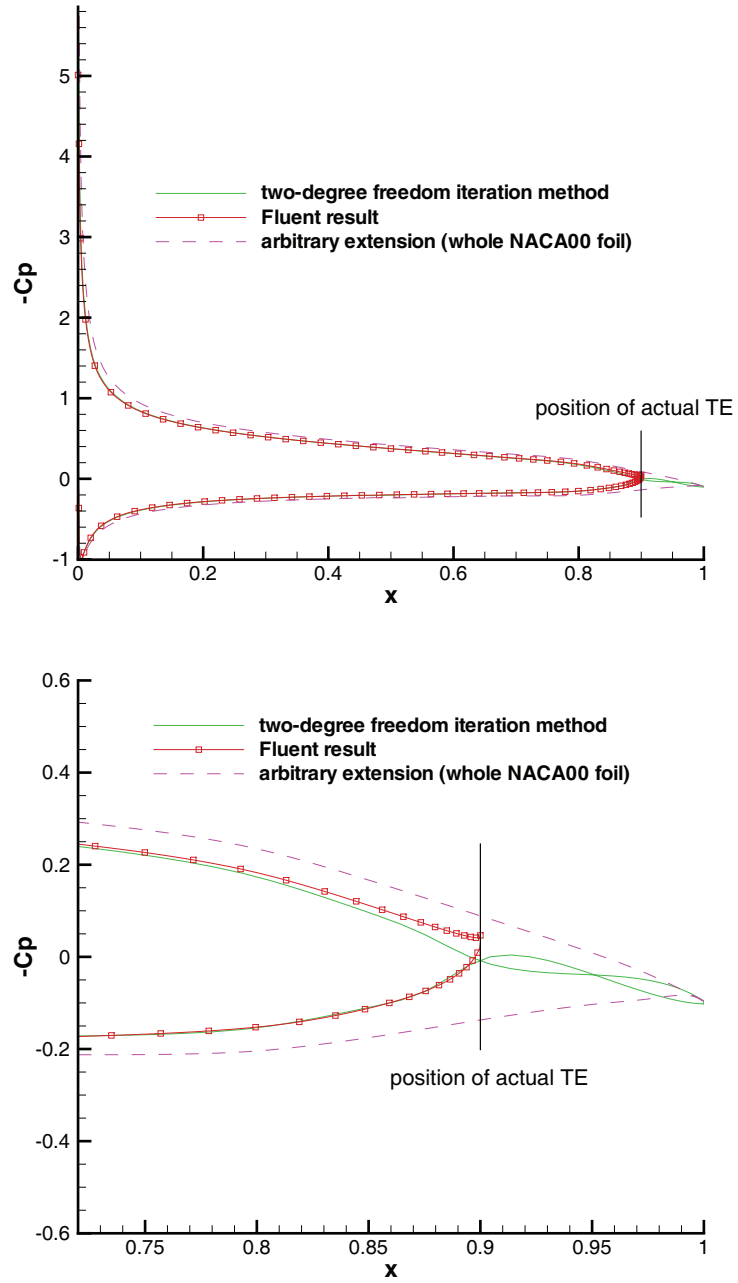


Figure 3.8: Comparison of results from the two degrees of freedom iteration method and Fluent: (a) global result, (b) near the trailing edge

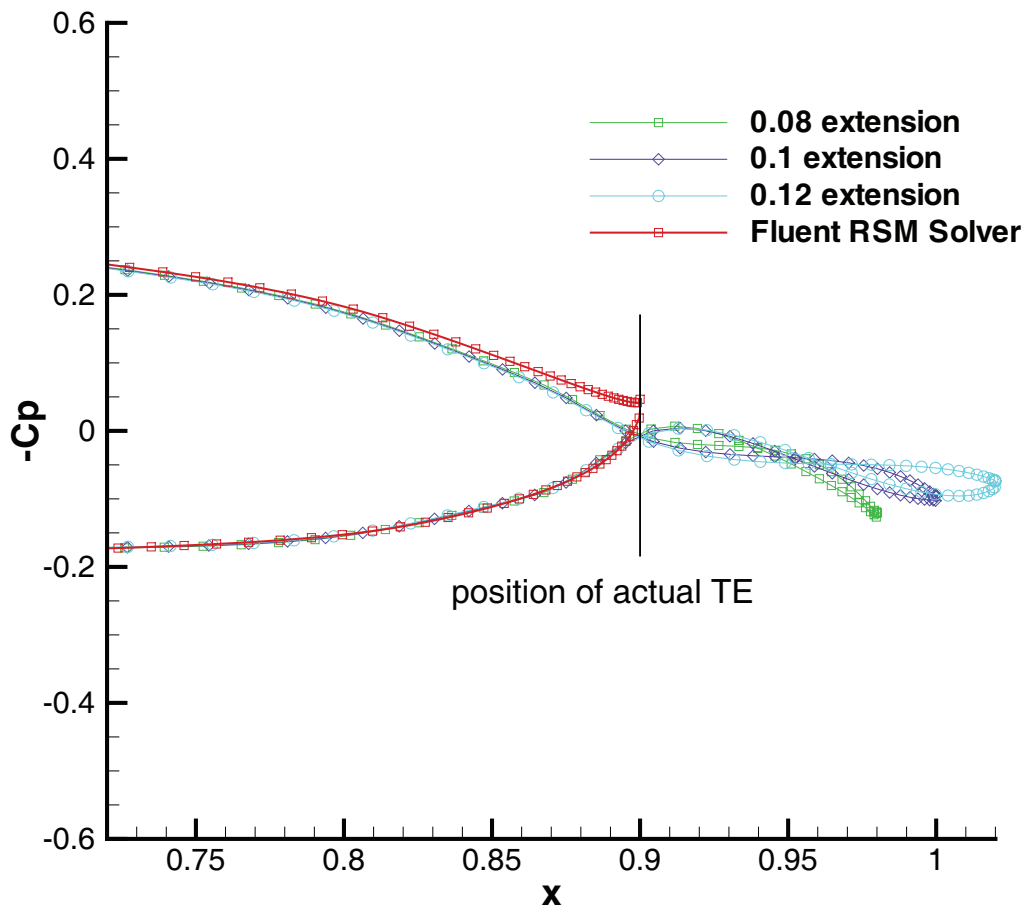


Figure 3.9: Influence of extension length on C_p distribution

However, a deficiency of this method exists that even if the lifting force on the extension vanishes, the pressure difference on the two sides at each location is not equal to zero. This is largely due to the insufficiency of the control of the extension geometry in this method. The camber line is controlled by two points but the thickness form stays unchanged in the iteration process. The following scheme is developed to overcome this difficulty.

3.2.3 Cavity-like scheme

This scheme is developed based on the iteration method for solving partial-cavitating problems. BEM solver has been found to be effective to model partial cavitation on suction side of a 2D hydrofoil. [Brewer and Kinnas 1997, Kinnas and Fine 1993]. In a cavitation problem, the pressure distribution on the cavity surface is constant. If the two sides of the extension are treated as two cavity surfaces, the scheme will give constant pressure distribution on each side of the extension. Furthermore, if the pressures at the two sides are equal to each other, an extension can be obtained using the condition that the pressure difference at each location is zero. Besides, the previous scheme for cavitation problem can be changed so that different profiles of pressure distributions can be obtained on the extension surfaces.

3.2.3.1 Mathematical Formulation

The perturbation potential, ϕ , must satisfy Green's formula, a Fredholm integral equation of the second kind, on the foil and extension.

$$\pi\phi_p = \int_S \left[-\phi \frac{\partial \ln R}{\partial n} + \frac{\partial \phi}{\partial n} \ln R \right] dS - \int_W \Delta\phi_w \frac{\partial \ln R}{\partial n} dS \quad \text{on } S \quad (3.1)$$

where S is the surface of the wetted foil and the cavity (extension) surface and W is the surface of the wake. R is the distance from the surface element dS to the point p . $\Delta\phi_w$ is the potential jump in the wake.

On the actual foil and extension, the kinematic boundary condition is satisfied so that the flow is tangent to the surface. (The cavitation model assumes that the cavity surface is a streamline on which pressure is equal to water vapor pressure.)

$$\frac{\partial \phi}{\partial n} = -\frac{\partial \Phi_{in}}{\partial n} = -U_\infty \cdot \vec{n} \quad (3.2)$$

On the extension (cavity-like surface), the dynamic boundary condition is satisfied so that the pressure distribution (or velocity distribution) has a certain profile on both sides of the extension.

$$\frac{\partial \phi}{\partial s_{c1}} + \frac{\partial \Phi_{in}}{\partial s_{c1}} = q_{c1} [1 + x \cdot Ratio] \quad \text{on the upper side} \quad (3.3)$$

$$\frac{\partial \phi}{\partial s_{c2}} + \frac{\partial \Phi_{in}}{\partial s_{c2}} = q_{c2} [1 + x \cdot Ratio] \quad \text{on the lower side} \quad (3.4)$$

where Φ_{in} is the inflow velocity potential. s_{c1} and s_{c2} are the arclengths of the suction side extension and pressure side extension, respectively. q_{c1} and

q_{c2} are velocities at the leading edges of suction side extension and pressure side extension, respectively. x is the horizontal distance to the finite trailing edge, as shown in Figure 3.10. *Ratio* is set as a user-defined parameter, to determine the profile of pressure distributions on the extension surfaces.

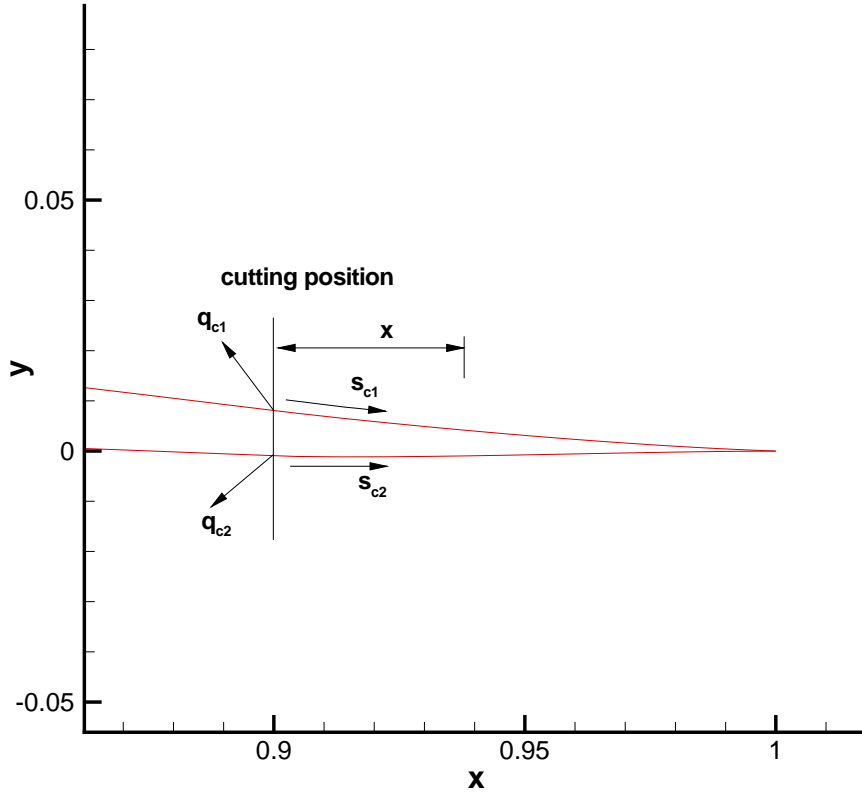


Figure 3.10: Definition of variables for cavity-like extension

By integrating (3.3) and (3.4), the expressions for ϕ on the extension are obtained.

$$\phi(s_{c1}) = -\Phi_{in}(s_{c1}) + \Phi_1(0) + q_{c1} \int_0^{s_{c1}} [1 + x \cdot Ratio] dS \quad (3.5)$$

$$\phi(s_{c2}) = -\Phi_{in}(s_{c2}) + \Phi_2(0) + q_{c2} \int_0^{s_{c2}} [1 + x \cdot Ratio] dS \quad (3.6)$$

where $\Phi_1(0)$ and $\Phi_2(0)$ are the total potentials at the leading edges of suction side extension and pressure side extension, respectively.

The extension surface, and thus s_c , is not known and will be determined iteratively in the present method. As a first iteration, the extension panels are placed on an arbitrary extension behind the finite trailing edge. At each successive iteration the extension panels are relocated on the updated extension surfaces, which are computed at the end of the previous iteration. The ‘‘cavity’’ height (taken normal to the present iteration ‘‘cavity’’ surface) is h_c and it represents the amount by which the updated extension surface has to be corrected. At the end of the extension, the cavity closure condition is satisfied so that the cavity height vanishes at the end.

$$h_{c1}(s_{c1L}) = 0 \quad \text{on the upper side} \quad (3.7)$$

$$h_{c2}(s_{c2L}) = 0 \quad \text{on the lower side} \quad (3.8)$$

where h_{c1} and h_{c2} are the cavity heights on the suction side extension and pressure side extension, respectively. s_{c1L} and s_{c2L} are the total arclengths of the suction side extension and pressure side extension, respectively.

It can be shown that the following relationship is valid up to the first order in h_{c1} and h_{c2} . [Kinnas and Fine 1991]

$$q_{c1}(1 + x \cdot Ratio) \frac{dh_{c1}}{ds_{c1}} = \frac{\partial \phi}{\partial n} + \frac{\partial \Phi_{in}}{\partial n} \quad \text{on the upper side} \quad (3.9)$$

$$q_{c2}(1 + x \cdot Ratio) \frac{dh_{c2}}{ds_{c2}} = \frac{\partial \phi}{\partial n} + \frac{\partial \Phi_{in}}{\partial n} \quad \text{on the lower side} \quad (3.10)$$

Combining Equation (3.7),(3.8),(3.9) and (3.10), we arrive at the cavity closure condition:

$$\int_0^{s_{c1L}} \frac{\partial \phi}{\partial n} \frac{ds_{c1}}{1 + x \cdot Ratio} = - \int_0^{s_{c1L}} \frac{\partial \Phi_{in}}{\partial n} \frac{ds_{c1}}{1 + x \cdot Ratio} \quad \text{on the upper side} \quad (3.11)$$

$$\int_0^{s_{c2L}} \frac{\partial \phi}{\partial n} \frac{ds_{c2}}{1 + x \cdot Ratio} = - \int_0^{s_{c2L}} \frac{\partial \Phi_{in}}{\partial n} \frac{ds_{c2}}{1 + x \cdot Ratio} \quad \text{on the lower side} \quad (3.12)$$

Equations (3.1),(3.2),(3.5),(3.6),(3.11) and (3.12) can be solved simultaneously for all the unknowns. Suppose we have N panels on the hydrofoil (including the extension), the unknowns to be determined are from $N + 2$ equations. (N equations from Green's formula and 2 cavity closure conditions). Therefore, q_{c1} and q_{c2} are determined in the solution, as well as ϕ and $\frac{\partial \phi}{\partial n}$ on the foil and extension surface. The updated extension surface is obtained using Equations (3.9) and (3.10), and the kinematic boundary condition on the extension is only satisfied when the solution of the extension surfaces is obtained. Finally, the pressure distribution is determined on the updated surface, as shown in Figure 3.11.

Due to the unsymmetrical geometry of a general foil, the initial arbitrary extension will give some difference between q_{c1} and q_{c2} . To make q_{c1} equal to q_{c2} (so that the two pressures are equal to each other), an outer iteration process is needed (with respect to the inner iteration process to determine the extension surfaces). The last camber point of the extension is again set as

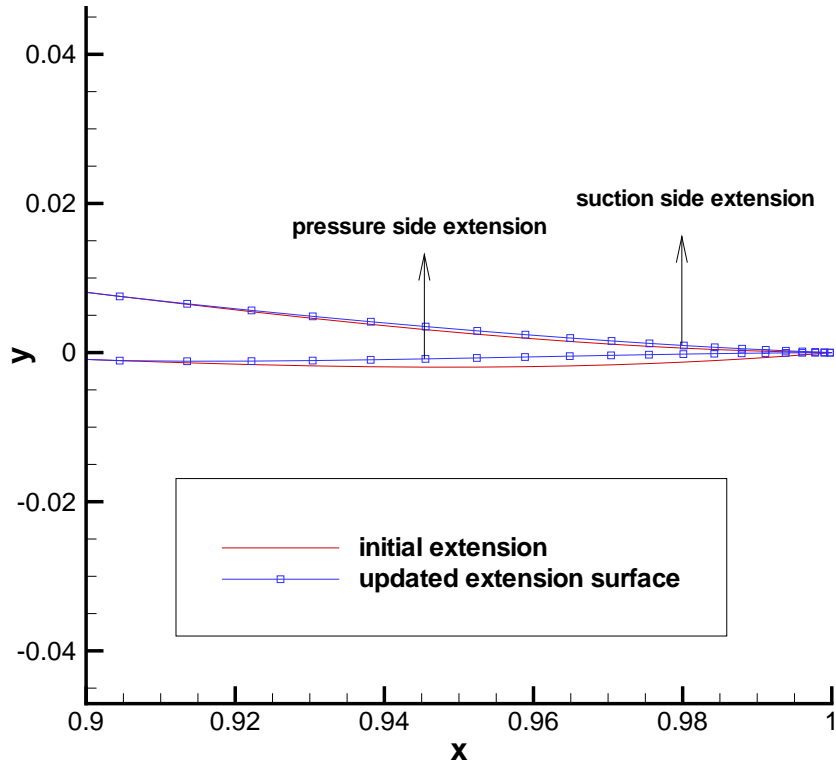


Figure 3.11: Updated extension surface

the control point, and Newton-Secant method is used to update the vertical position of this point. This outer loop ends until a solution is obtained for which $q_{c1} = q_{c2}$.

A flowchart of the whole process is shown in the Figure 3.12.

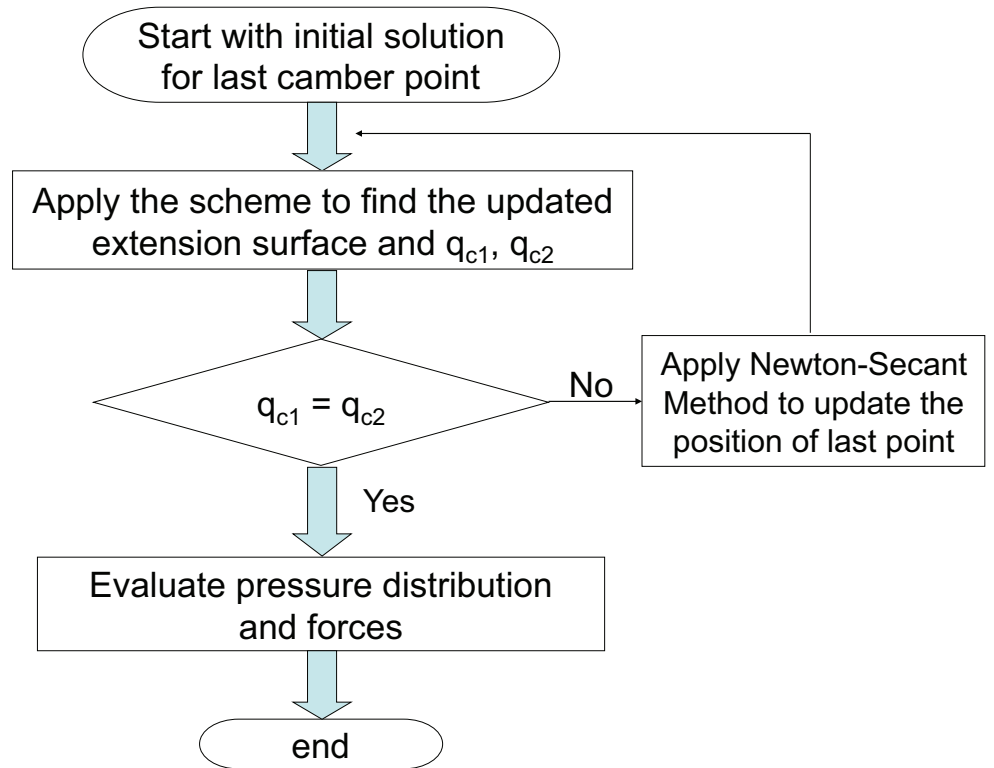


Figure 3.12: Flowchart for cavity-like scheme

3.2.3.2 Results from Cavity-like Scheme

The viscous pressure distribution on the hydrofoil for $Ratio = -0.3$ is shown in Figure 3.13, from which we can see that the pressure difference at each location on the two sides of the extension vanishes.

The influence of different values of $Ratio$ on inviscid and viscous pressure distributions is studied and shown in Figures 3.14 and 3.15. Note that $Ratio \leq 0$ because pressure increases (velocity drops) along the separation zone. Figure 3.14 shows that for different values of $Ratio$, different pressure distributions are developed on the extension surfaces, but the pressure differences on the two sides of the extension are equal to zero. The sudden change of pressure at the end of the extension is due to the inviscid cavity closure. Figure 3.15 shows that the viscous effect influences the pressure distribution so that the pressures of the two sides do not equal to each other for all locations of the extension. For $Ratio = -0.3$, however, the influence happens to be very small. [Kinnas et al. 1994] provides a scheme to correct the viscous pressure (make it constant on the cavity surface), but it is found that the correction scheme does not have a significant impact on the pressure distribution. Therefore it is not applied here. (This scheme is discussed in Chapter 5.) Furthermore, both figures show that the value of $Ratio$ affects the pressure distribution near the trailing edge, but the influence is not significant.

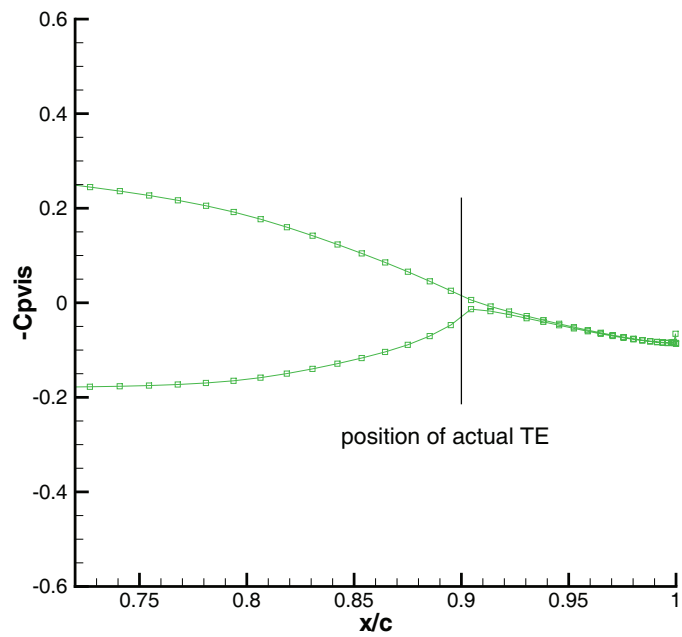
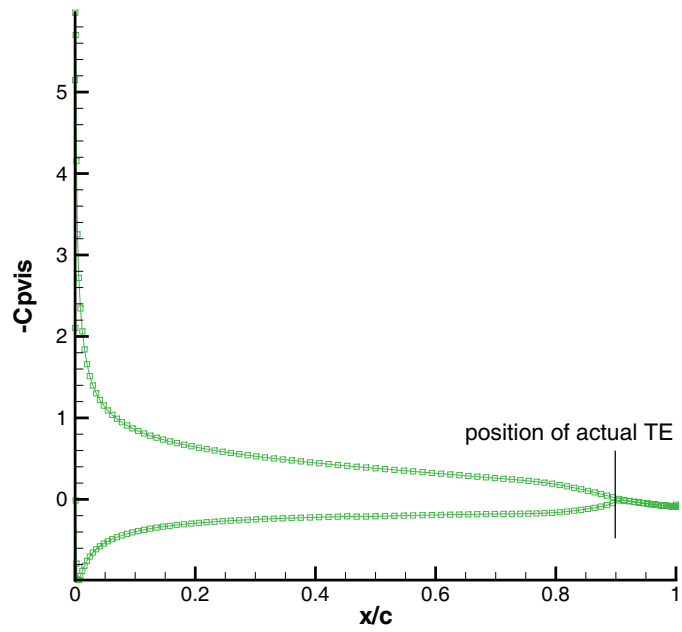


Figure 3.13: Viscous C_p distribution on the hydrofoil ($Ratio = -0.3$): (a) global result, (b) near the trailing edge

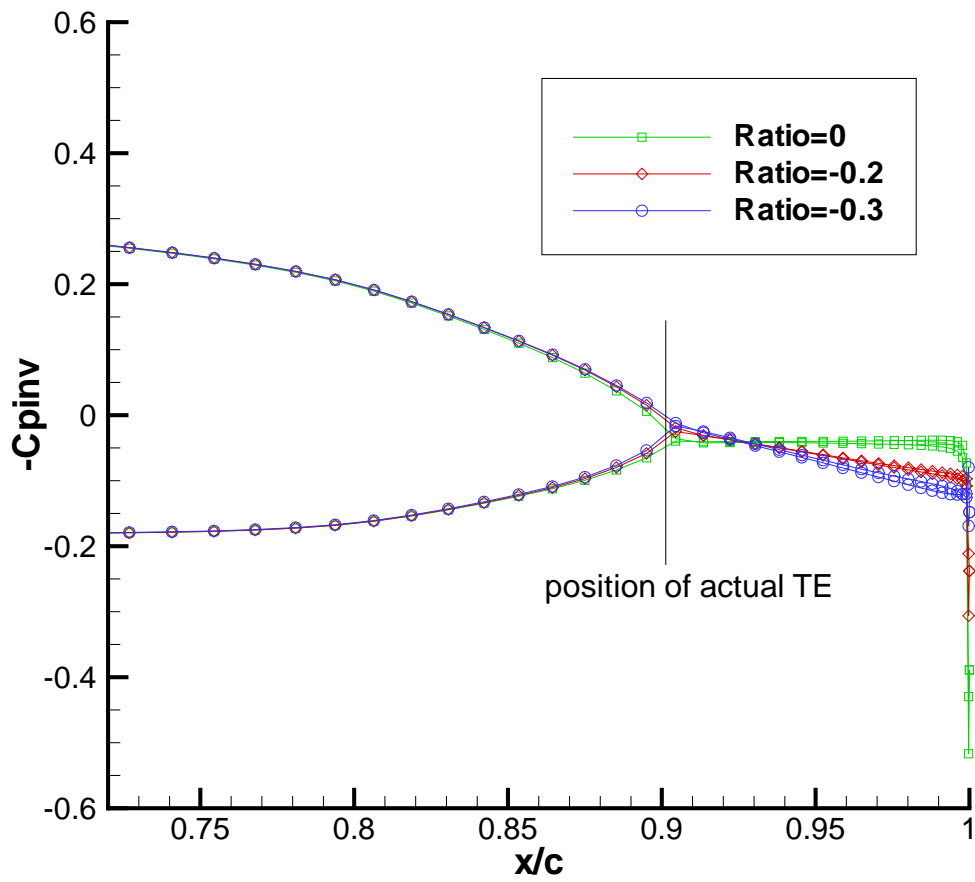


Figure 3.14: Influence of different values of *Ratio* on inviscid pressure distribution, using the cavity-like scheme

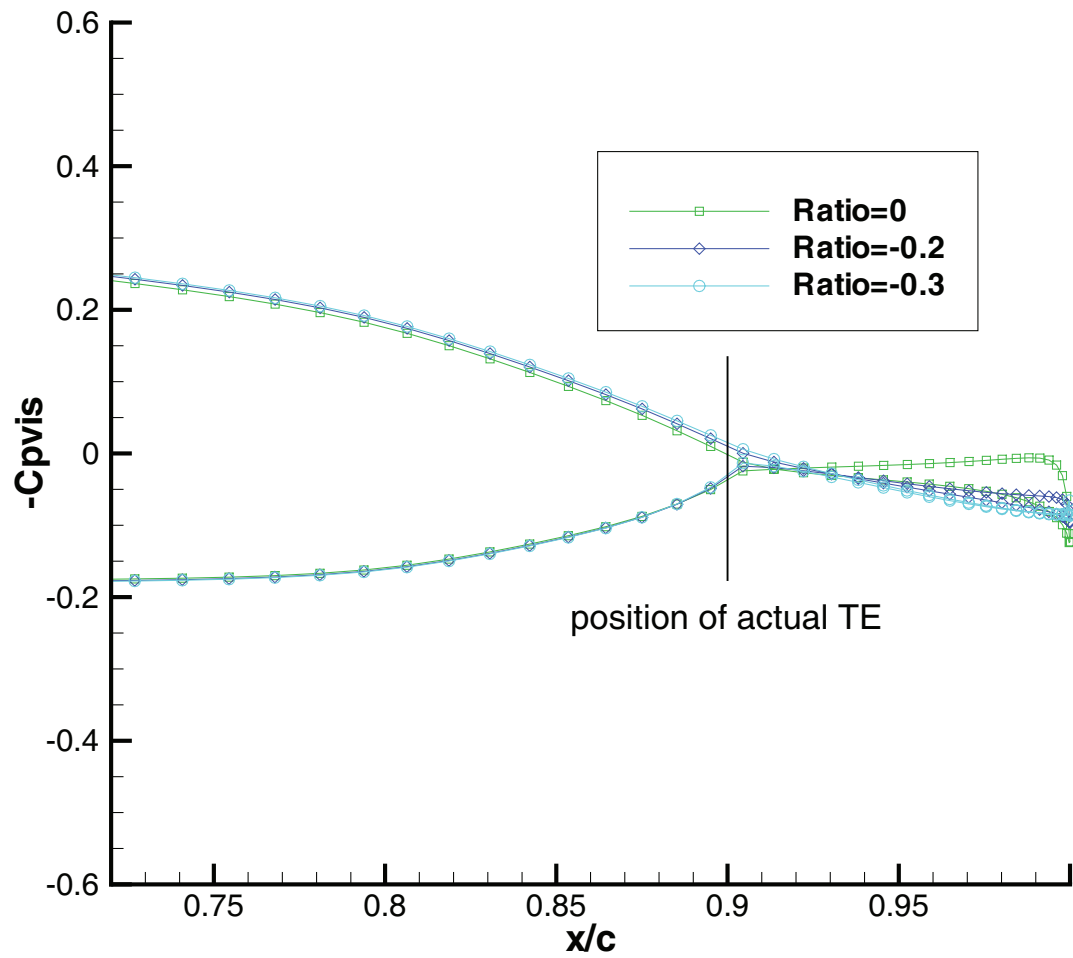


Figure 3.15: Influence of different values of *Ratio* on viscous pressure distribution, using the cavity-like scheme

3.2.4 Correlation of all current methods with Fluent analysis

The comparison of pressure distribution predicted by the current methods and Fluent is shown in Figure 3.16, from which one can see that all presented schemes predict the pressure distribution with acceptable accuracy. Also, the two degrees of freedom iteration method and cavity-like scheme both give more accurate results, compared with the one degree of freedom iteration method, assuming that the Fluent result is the “correct” one. The comparison

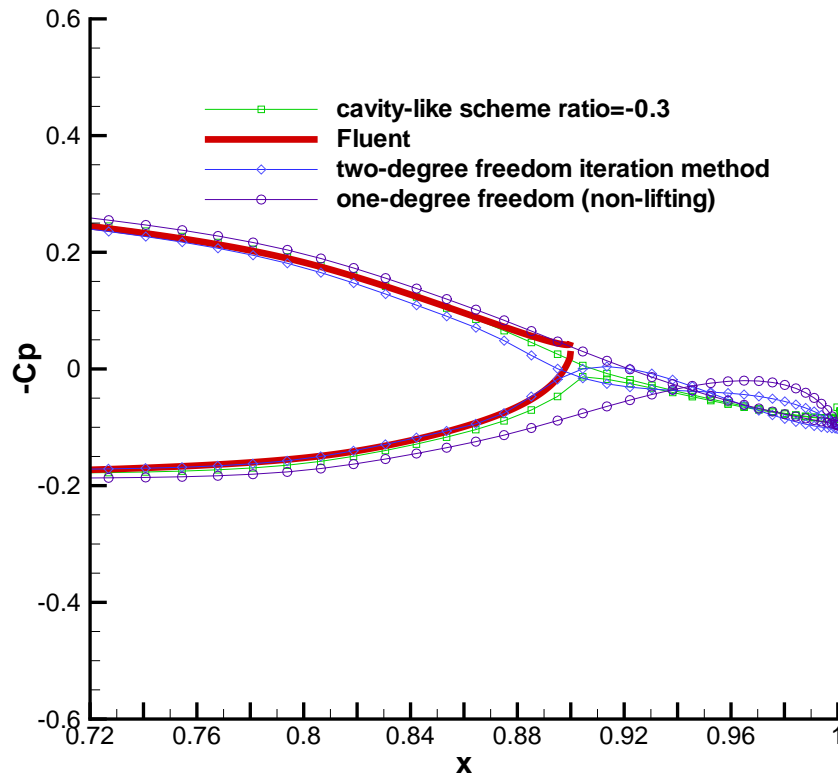


Figure 3.16: Comparison of pressure distributions predicted by proposed methods and Fluent

of lifting forces evaluated by current schemes and Fluent is shown in Table 3.2. Note that for the BEM solution, lift is evaluated only over the foil, not including the separation zone. For this case, Both two degrees of freedom iteration method and cavity-like scheme give the good correlations with Fluent.

Table 3.2: Comparison of lifting force predicted by proposed methods and Fluent

Method	C_L
Fluent	0.6717
arbitrary extension	0.7758
one degree of freedom	0.7124
two degrees of freedom	0.6744
cavity-like scheme	0.6915

The comparison of computational cost is shown in Table 3.3, from which we can see that the computational cost is reduced tremendously by applying the presented schemes.

Table 3.3: Comparison of computational cost

Analysis Method	Fluent	All presented schemes
Computer Characteristics	10 cores of dual-core CPUs (1.6GHZ AMD Opteron,	1 core of a dual-core CPU
Running Time	about 4 hours for steady run	Less than 1 minute

3.2.5 Some other results for different angles of attacks

Some other results are shown for the same hydrofoil at other angles of attack, for the test of the scheme. Figure 3.17 and Figure 3.18 shows the correlations of pressure distributions between current methods and Fluent at seven and four degrees angle of attack, respectively. The comparison shows that the two degrees of freedom iteration method and cavity-like scheme both give reasonable results.

The presented scheme provides a way to predict the performance of hydrofoil with non-zero trailing edge thickness, for which the detachment position of the separation zone is known as a priori. However, for a hydrofoil with rounded trailing edge, some iterative procedure is needed to find the flow detachment position. The shape factor H ($H = \delta^*/\theta$, where δ^* is the displacement thickness and θ is the momentum thickness) might serve as a useful parameter to find the separation position. This work is discussed in Chapter 6 as future work.

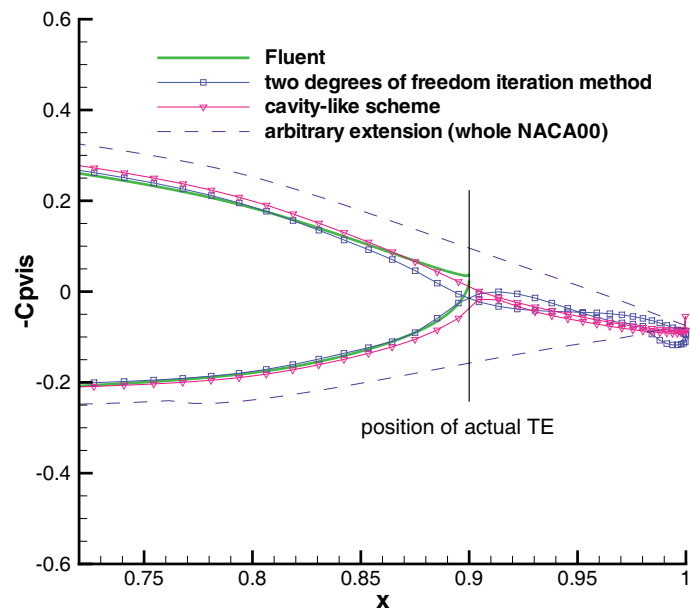
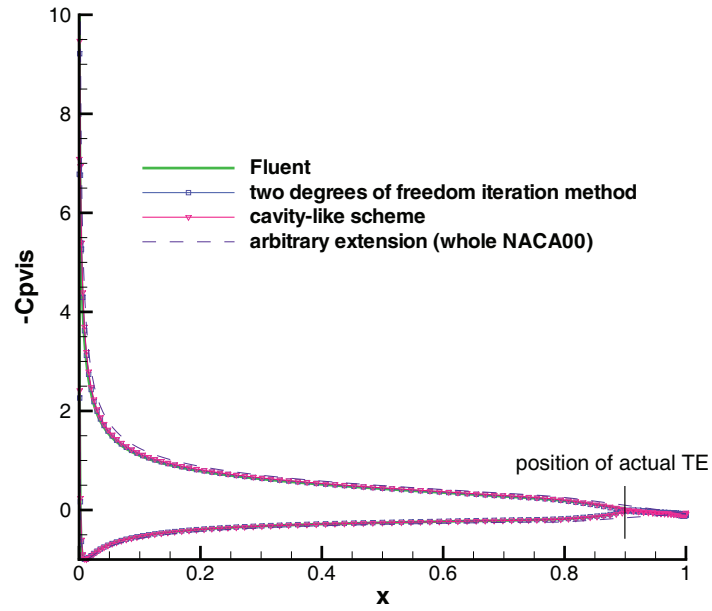


Figure 3.17: Comparison of pressure distributions predicted by proposed methods and Fluent at 7 degrees angle of attack

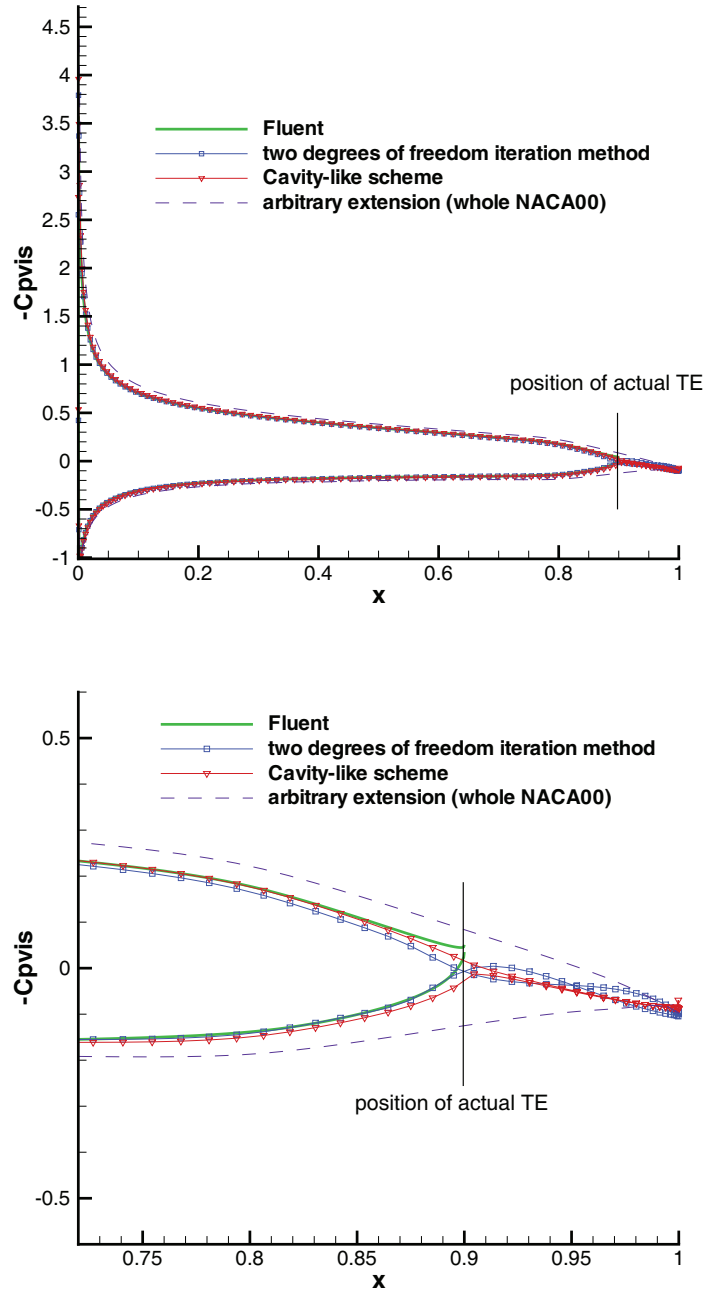


Figure 3.18: Comparison of pressure distributions predicted by proposed methods and Fluent at 4 degrees angle of attack

Chapter 4

Methodology and Results in 3D

4.1 Propeller Geometry

The propeller used in this study is a five-blade propeller with $P_{0.7}/D = 0.9288$, where $P_{0.7}$ is the propeller pitch at 70% of the propeller radius, and D is the propeller diameter. A global view of the propeller is shown in Figure 4.1, and some section geometries of the propeller are plotted in Figure 4.2 (Only trailing edge parts are shown.). More details of the propeller geometry are restricted from including in the thesis, by the provider of the experimental data. The feature of this propeller, significant non-zero trailing edge thickness, is evident in both figures. The t_0/c of this propeller varies from 0.6% to 5% , where t_0 and c are the trailing edge thickness and chord length of each strip of the propeller, respectively. For convenience, we will call this propeller "propeller A" hereafter.

In the past, this kind of propeller is treated using two different types of approximations. As shown in Figure 4.3, approximation 1 closes the trailing edge of each strip at its mid-point. In current application, the foil geometries are modified near the trailing edges over 20% of the chord lengths. Approximation 2 uses an extension with zero camber at the last point behind each

finite trailing edge. In current application, extensions of 10% of the chord lengths (including extensions) are used.

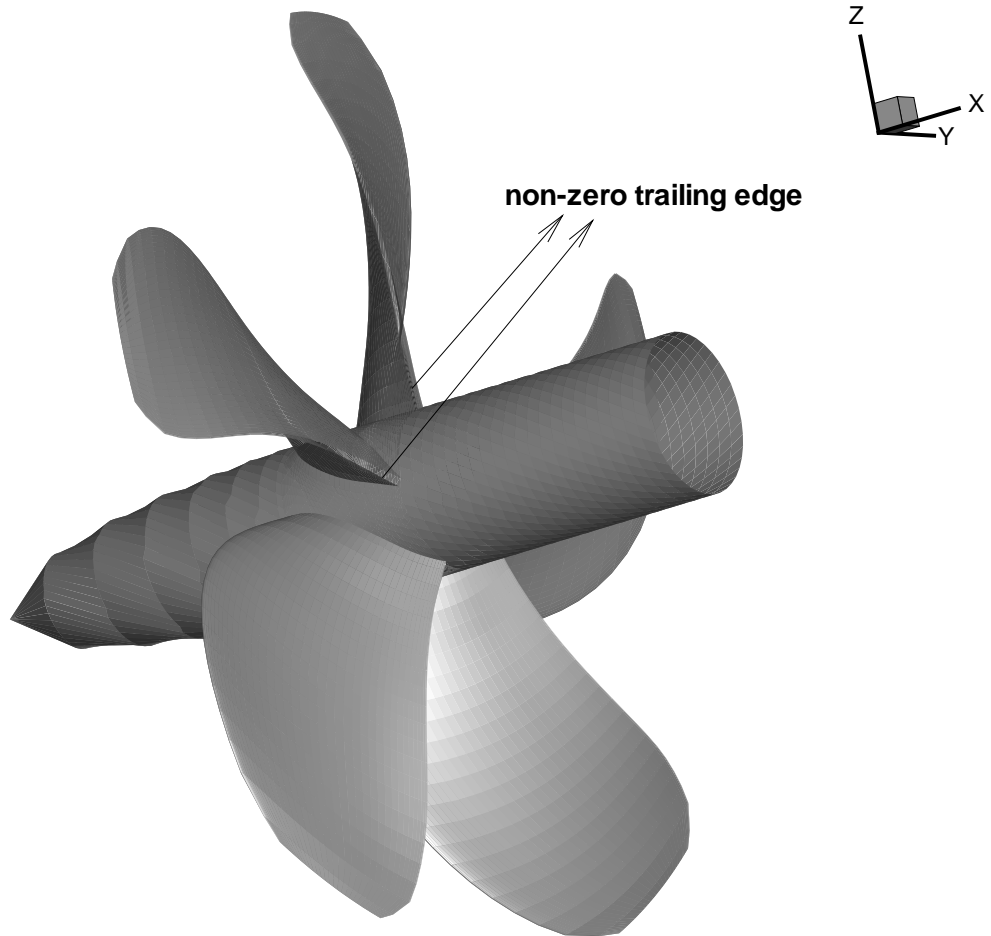


Figure 4.1: The propeller A, with significant non-zero trailing edge thickness

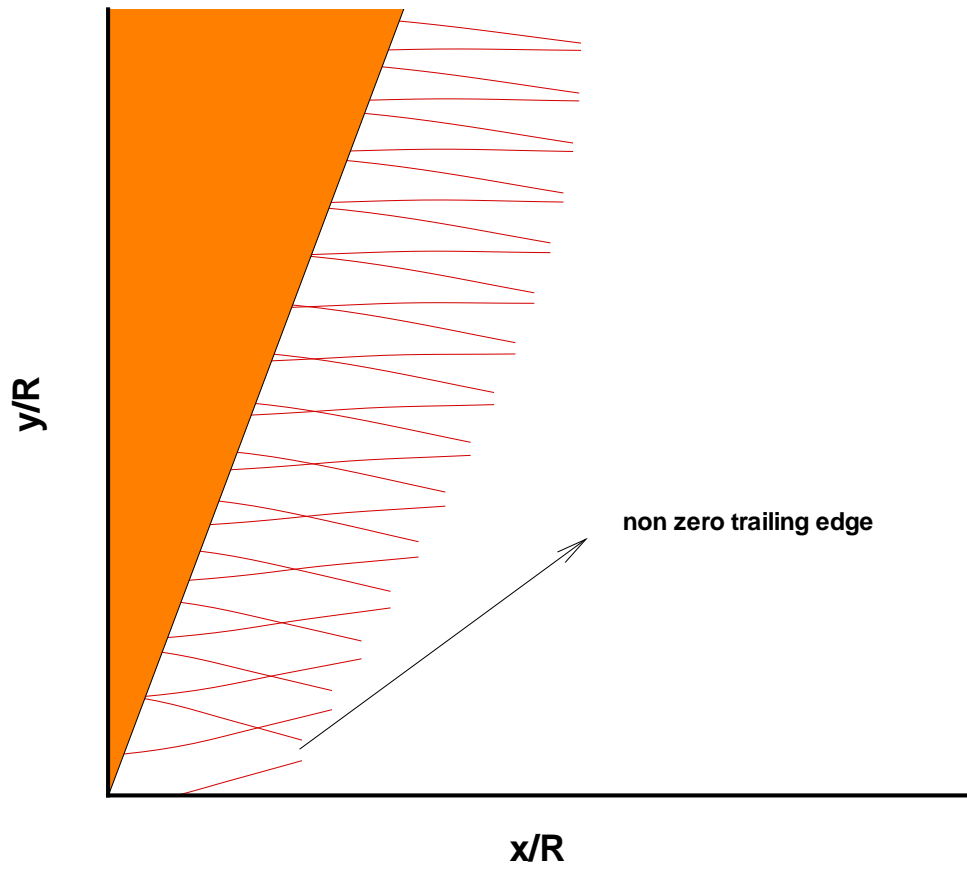


Figure 4.2: Expanded view of some sections of propeller A

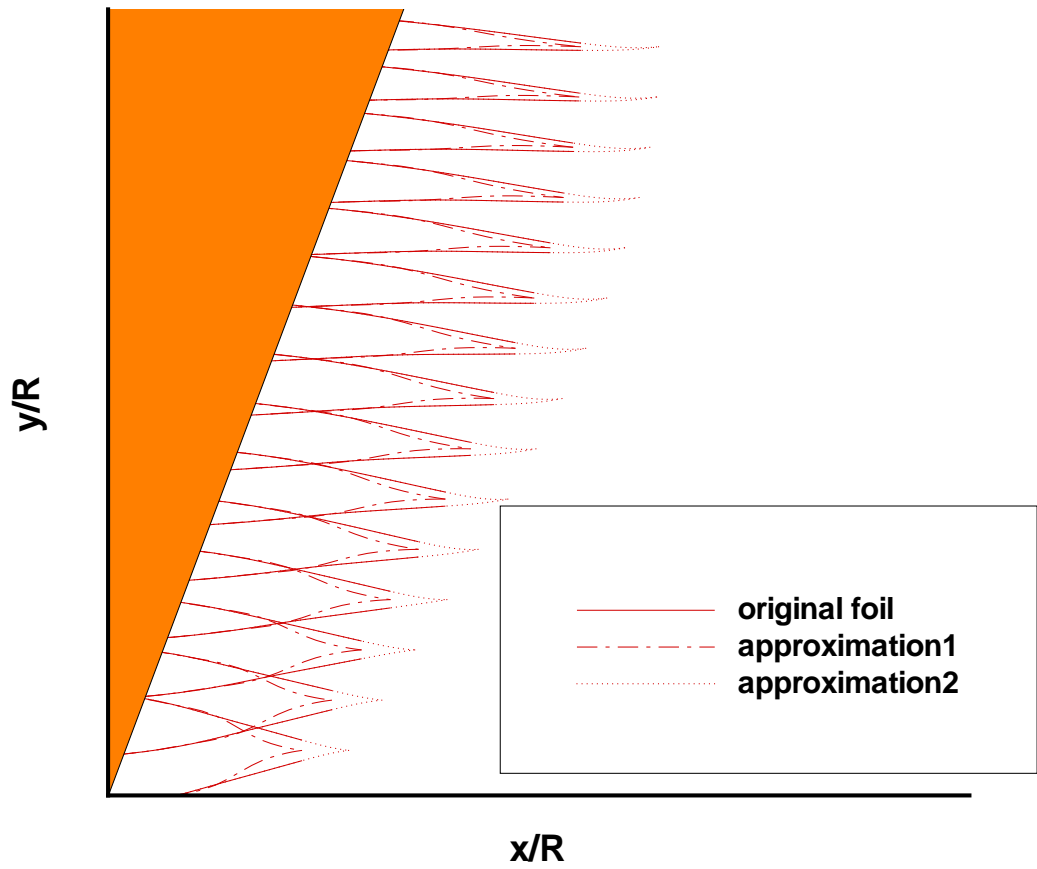


Figure 4.3: Two approximations used in the past

One way of generating approximation 1 is by using a parabolic distribution of DS between the original geometry and modified geometry, as shown in Figure 4.4. Specifically,

$$DS = (YS_{ori} - YP_{ori}) \times (12.5\bar{x}^2 - 20\bar{x} + 8) \quad (4.1)$$

$$YP_{mod} = YP_{ori} + DS \quad (4.2)$$

$$YS_{mod} = YS_{ori} - DS \quad (4.3)$$

$$\text{So that when } \bar{x} = 0.8, YP_{mod} = YP_{ori}; YS_{mod} = YS_{ori}; \quad (4.4)$$

$$\frac{\partial DS}{\partial \bar{x}} = 0 \quad (4.5)$$

$$\text{when } \bar{x} = 1.0, YP_{mod} = YS_{mod} = 0.5 \times (YP_{ori} + YS_{ori}) \quad (4.6)$$

Where $\bar{x} = x/c$.

Equation (4.5) must be satisfied so that the modified geometry does not have a discontinuous point. Geometry discontinuity always causes pressure discontinuity on the strip. On the other hand, different lengths of the geometry can be modified by using different distributions of DS . In our research, 20% ~ 40% are tried and it was found that they do not have a significant impact on the forces and moments of the propeller.

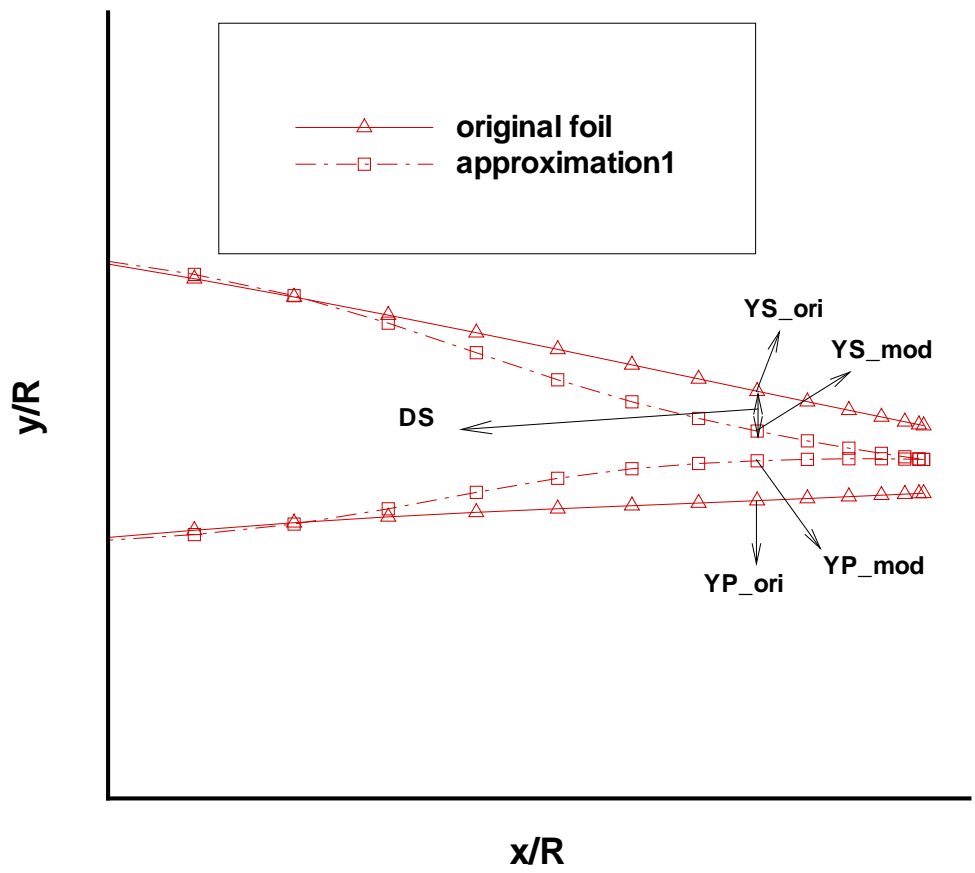


Figure 4.4: The way to close the non-zero trailing edge by using approximation 1

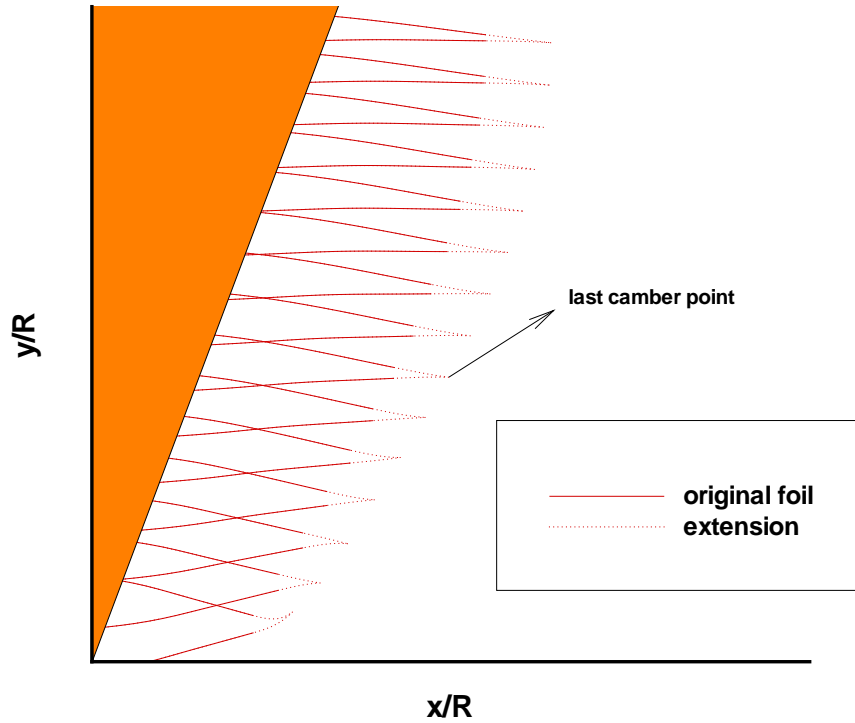


Figure 4.5: Current approach: original propeller with extensions determined by the last camber points

In the current approach, we extend each section by a flap, whose geometry is controlled by the location of the last camber point (or two camber points in two degrees of freedom model), as shown in Figure 4.5. As in the 2D model, we determine the positions of the last camber points so that the conditions used in 2D are satisfied at each strip of the propeller.

4.2 BEM-inviscid model

In this section, the BEM inviscid model is coupled with one or two degrees of freedom iteration method used in 2D. It turns out that this approach is not able to give a good correlation with experimental data. However, it is necessary to include these results in two senses: (1) Since the convergence of XFOIL is very difficult for some certain geometries in 3D, applying inviscid scheme could avoid this difficulty as a preliminary investigation. (2) Convergence study is easier to perform using inviscid model, in which the error from XFOIL is excluded.

4.2.1 One degree of freedom model in 3D

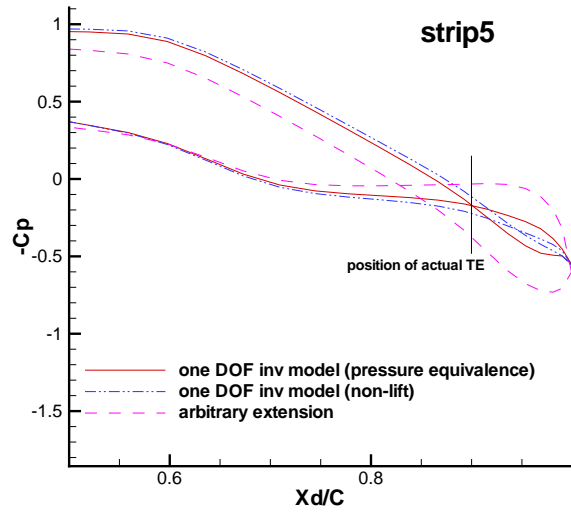
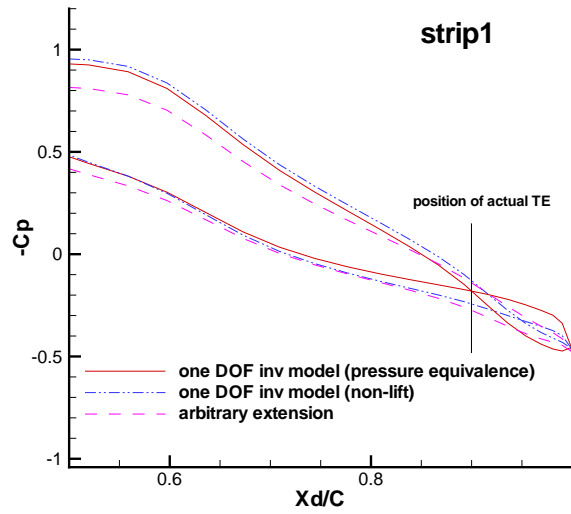
A sample case is provided here, for the explanation of this scheme. Consider propeller A as discussed before, extension of 10% of the chord length (including extension) is added behind each strip. The geometries of the extensions are determined in the same manner as in 2D - by the interpolation of the original strips and the last camber points. For this case, the advance ratio $J = \frac{V_s}{nD} = 0.85$, where V_s is the ship speed, n is the propeller rotational speed and D is the propeller diameter. 80 (chord-wise)*20 (span-wise) panels are used, including the extension. Cosine spacing is used in chord-wise and constant spacing is used in span-wise. Strips 1-20 are used for strips from the hub to the tip.

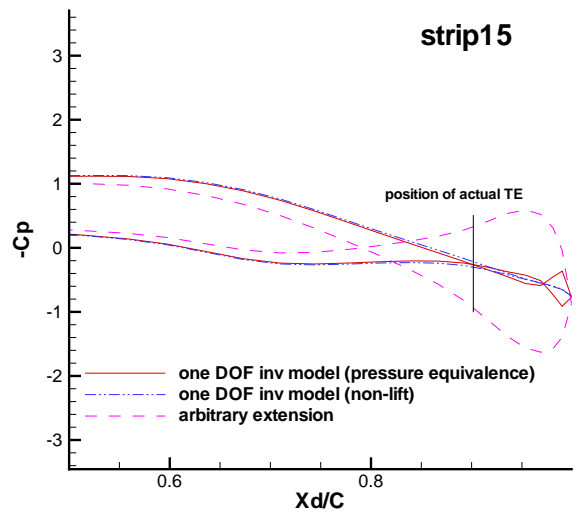
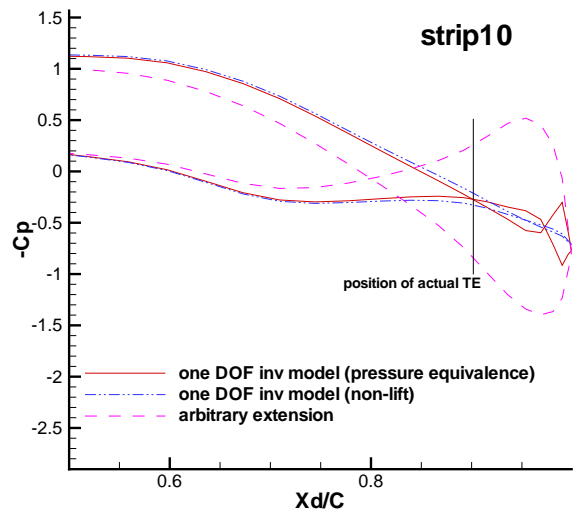
The pressure equivalence condition in 3D is similar as that in 2D. It requires that the 3D pressure distribution closes at the actual trailing edge of

each strip. The non-lift condition needs to be performed with more care, in term of the definition of lift. In 3D, each strip sees a different inflow velocities due to the different rotational linear speeds, even if the inflow wake is constant. Therefore, each strip has its own local angle of attack, which is related to the local pitch angle, rotational linear speed and inflow wake. The non-lift condition in 3D can be expressed as: For each strip, lift force with respect to the local angle of attack vanishes on the extension. Also, it is worthwhile to mention that the velocity has three components in 3D. The total velocity, including all three components, is considered in evaluation of pressure using Bernoulli's equation.

The convergence criterion is set as $\Delta C_p < 10^{-2}$ ($C_p = (p-p_0)/(\frac{\rho}{2}n^2D^2)$, where p_0 is the pressure at infinity.) for pressure equivalence condition and $C_L < 10^{-3}$ ($C_L = Lift/(\frac{\rho}{2}n^2D^2 \cdot Aex)$, where Aex is the planform area of the extension and $Lift$ is evaluated by integrating the pressure over the extension of each strip) for non-lift condition.

The scheme used to obtain the solution of one degree of freedom model is summarized in section 4.2.3. Here the pressure distributions on different strips are shown in advance in Figure 4.6, for the explanation of the scheme.





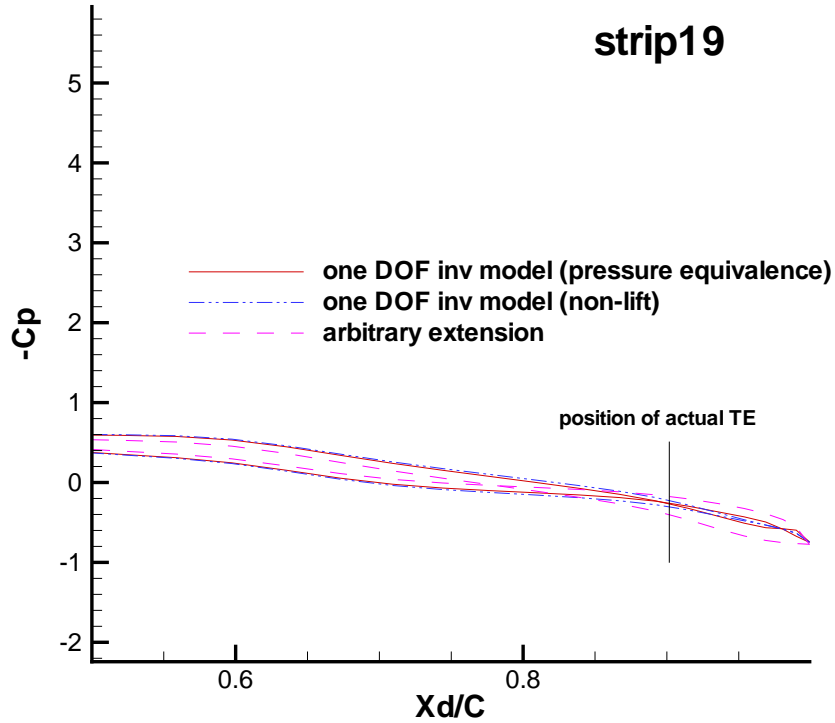


Figure 4.6: Inviscid pressure distributions on some sections for one DOF model in 3D at $J = 0.85$, span-wise positions of the strips: strip1: $r/R=0.1888$; strip5: $r/R=0.3552$; strip10: $r/R=0.5632$; strip15: $r/R=0.7712$; strip19: $r/R=0.9376$

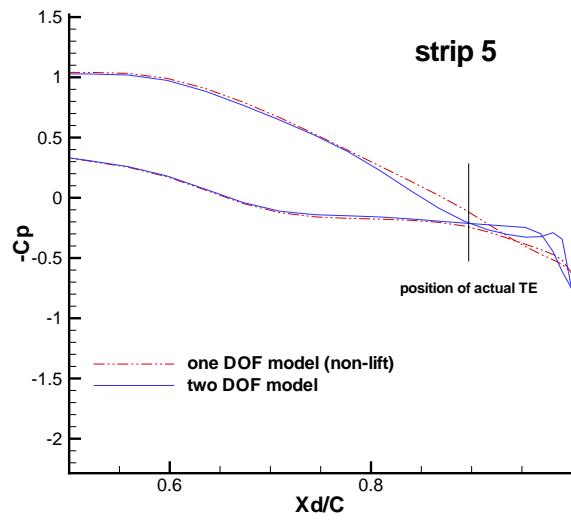
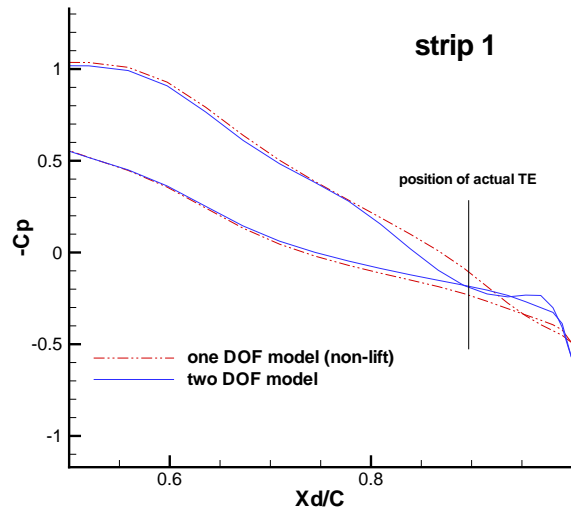
As shown in the Figure 4.6, the non-lift condition or pressure equivalence condition is satisfied on all strips for the two schemes, respectively. For strips near the hub, the correction obtained by applying current schemes is significant, compared with the results from arbitrary extensions. This is reasonable because the trailing edge thickness of the strips near the hub are much larger than those near the tip, as shown in Figure 4.2.

4.2.2 Two degrees of freedom model in 3D

Another sample case is provided here again, for the sake of explanation. As one DOF model, extension of 10% of the chord length is added behind each strip of propeller A. Instead of controlling the geometry of extension by the last camber point, the mid-point and last point are both chosen as the control points for each strip. For this case, $J = \frac{V_s}{nD} = 0.9$ and 80×14 panels are used to discretize the propeller surface. Fewer panels are used in the span-wise direction to have the convergence faster.

The convergence criterion is set the same as the one DOF inviscid model. At the end of the iteration, both conditions should be satisfied for each strip of the propeller, as shown in Figure 4.7.

The pressure distributions from the two degrees of freedom model do not have too many differences with those obtained by one degree of freedom model, except a small part near the trailing edge. It is found that the forces and moments predicted by these two models are not very different in 3D application.



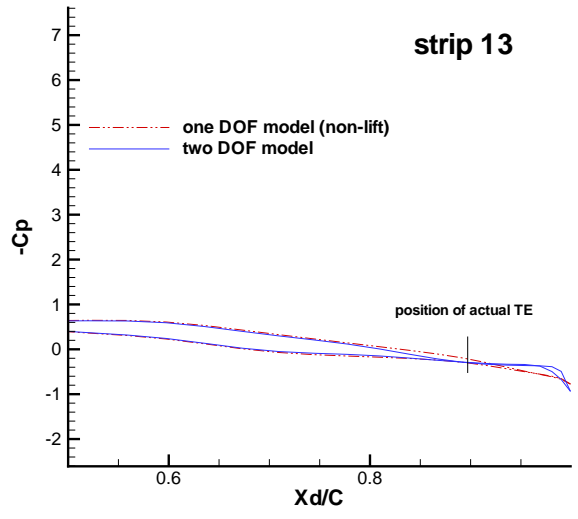
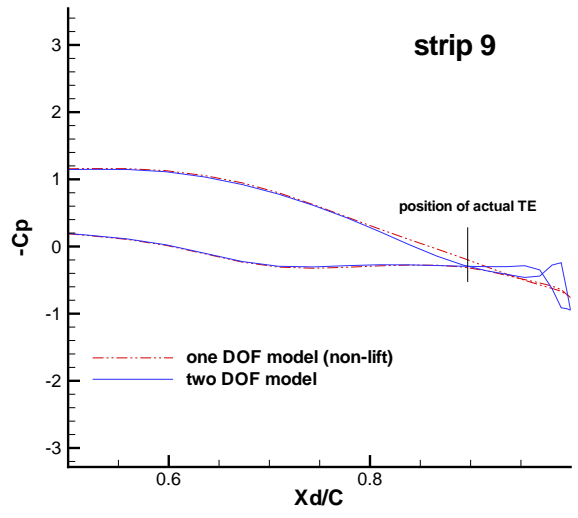


Figure 4.7: Inviscid pressure distributions on some sections for two DOF model in 3D at $J = 0.9$, span-wise positions of the strips: strip1: $r/R=0.1977$; strip5: $r/R=0.4354$; strip9: $r/R=0.6731$; strip13: $r/R=0.9109$

4.2.3 Solution scheme

In this section, one DOF model with pressure equivalence condition is taken as an example for explaining the scheme to obtain a converged solution. In this case, $J=0.9$ and $80*20$ panels are used.

The pressure difference at the actual trailing edge of each strip is a function of 20 last camber points. The problem can be described as determining twenty unknowns (positions of twenty camber points y_1, y_2, \dots, y_{20}) by satisfying twenty conditions (pressure differences at the original trailing edges vanish; $\Delta p_1, \Delta p_2, \dots, \Delta p_{20} = 0$). Mathematically, we need to solve 20 equations:

$$\Delta p_n(y_1, y_2, \dots, y_{20}) = 0, n = 1, 2, \dots, 20$$

A natural idea to solve this problem is to use a 20-equation Newton-Raphson method. However, a fatal drawback, as shown below, makes this scheme difficult.

Accurate numerical derivatives, which are needed in Newton-Raphson method, are hard to obtain. On the other hand, the N-equation Newton-Raphson method needs accurate numerical derivatives and good initial solutions to get converged. The figure 4.8 shows the numerical derivatives $\frac{\partial \Delta p_n}{\partial y_{10}}$ by using different sizes of Δy_{10} .

As shown in Figure 4.8, when Δy_{10} is very small ($\Delta y_{10} = 0.000001$), the error of PROPCAV (mostly due to its single precision) ruins the result.

When Δy_{10} becomes slightly larger ($\Delta y_{10} = 0.00001$ and $\Delta y_{10} = 0.0001$),

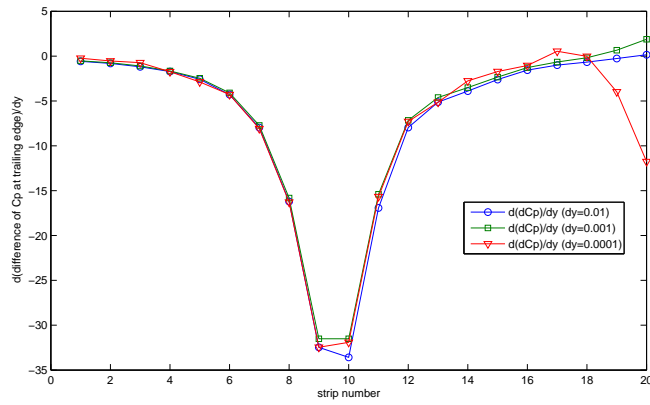
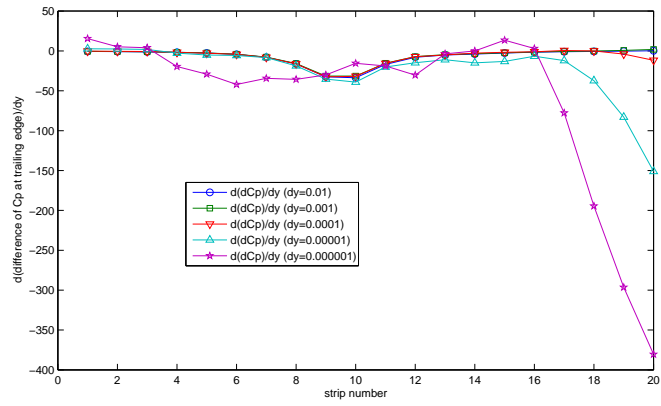


Figure 4.8: The numerical derivatives $\frac{\partial \Delta p_n}{\partial y_{10}}$ by using different sizes of Δy_{10}

the global results are improved, but near the tips (and also hub) the results still behaves oddly due to error of PROPCAV.

$\Delta y_{10} = 0.01$ and $\Delta y_{10} = 0.001$ give globally reasonable results. However, for $\Delta y_{10} = 0.001$ the tip is still a problem. Because theoretically, the derivatives should tend to zero as the position goes far from strip 10. Therefore, the size of Δy_{10} to give reasonable derivatives are in the order of $O(0.001)$ - $O(0.01)$. However, derivatives in this order are not accurate because Δy_{10} is in the same order of *final solution – initial solution*. For example, if we start with an initial solution of $(0,0,0,0,\dots,0,0,0,0)$ for this case, the final solution, obtained by another scheme which works, turns out to be $(0.0061676,0.0055281,0.0029191,-0.0019412,\dots,-0.0035514,-0.0014955,-0.0007270,0.0000458)$.

Two facts make the situation even worse. First, for different strips, the sizes of Δy_n to obtain reasonable numerical derivatives are different. It is hard to find a uniform Δy_n to apply on all strips. Second, for viscous calculations, when the error of XFOIL steps in, things become even harder.

A scheme without using numerical derivatives is applied for current case. The basic idea is from the figures of numerical derivatives shown above: Moving the last camber point of strip n only influences Δp near strip n. The iteration process of this scheme is outlined as follows:

1. Solve the equation $\Delta p_1(y_1) = 0$ using Newton-Secant method, with y_2, y_3, \dots, y_{20} as constants.
2. Solve the equation $\Delta p_2(y_2) = 0$ using Newton-Secant method, with y_1, y_3, \dots, y_{20}

as constants.

.....

20. Solve the equation $\Delta p_{20}(y_{20}) = 0$ using Newton-Secant method, with y_1, y_2, \dots, y_{19} as constants.

21. Check if all strips converge. If not, steps 1-20 are applied again. (Any of steps 1-20 might be skipped if the equation is satisfied before the iteration of Newton-Secant method)

Similar schemes can be applied on one DOF non-lift condition and two DOF model. In two DOF model, steps 1-20 should be modified as: Solve the equations $\Delta p_n(\text{camber point1 at strip } n, \text{ camber point2 at strip } n) = 0$ and $C_{Ln}(\text{camber point1 at strip } n, \text{ camber point2 at strip } n) = 0$ using a 2-equation Newton-Raphson method. Here, 2-equation Newton-Raphson method works because accurate local numerical derivatives (like $\frac{\partial \Delta p_{10}}{\partial y_{10}}$) are easier to evaluate.

In the author's experience, this scheme works as long as the initial solution is not too bad. However, in some certain cases, trial-and-error is needed for finding a good initial solution.

After a converged result is obtained, the forces and moments on the blade with non-zero trailing edge thickness need to be evaluated. In the current approach, they are evaluated as the sum of two parts, as shown in Figure 4.9:
part 1: forces and moments due to pressure and suction sides of the blade.
part 2: forces and moments due to non-zero trailing edge. For this part, the pressure is taken as the average of the base pressures at the pressure side and suction side.

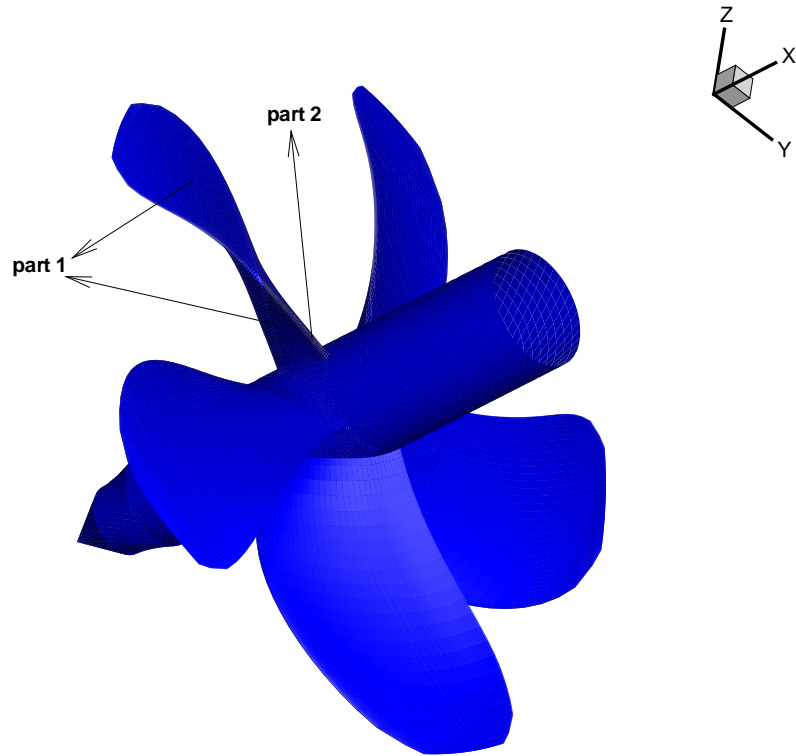


Figure 4.9: Two parts of forces and moments

A flow chart for the whole solution process is shown in Figure 4.10.

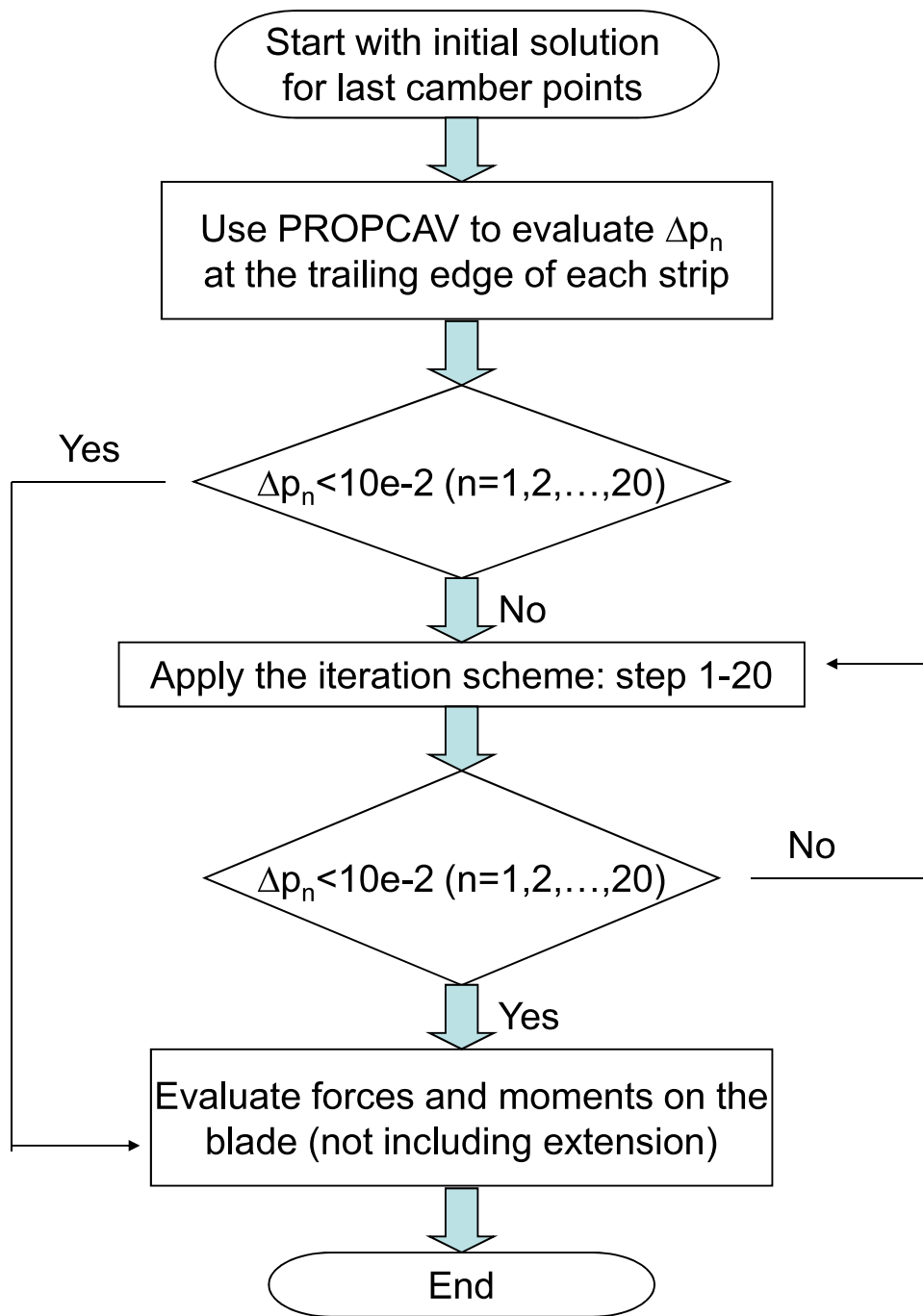


Figure 4.10: A flowchart for the whole solution process

4.2.4 Results and comparison

K_T and K_Q predicted by one degree of freedom model with both conditions are shown in the Figure 4.11, with the experimental data and results from the two approximations.

As shown in the Figure 4.11, the one degree of freedom inviscid model is an improvement from using arbitrary extensions (approximation 2). However, it gives no better results than approximation 1. Discrepancies with experimental data still exist, especially for K_T . Also, the two degrees of freedom model does not give better results than the one degree of freedom model. There might be two reasons for this: (1) The number of panels used in two DOF model is less than that in one DOF model in this application. Less number of panels is used here only for a fast convergence. However, convergence study shows that a difference of 14 and 20 panels in span-wise direction does not have a significant impact on the results, as discussed in Section 4.4. (2) Viscous effect is important in this kind of flow separation. Using inviscid model is not supposed to predict the forces and moments well. All the models are developed as viscous models in 2D. The non-lift condition, which we get evidence from Fluent result, only applies to viscous flow. As shown later in Section 4.3, Applying XFOIL on one DOF model helps improve the results significantly.

One might argue that the one degree of freedom inviscid model is no better than using a simple approximation 1. This is true in terms of inviscid forces and moments. However, using approximation 1 has two disadvantages. (1) Applying XFOIL on the generated geometry does not help to improve the

results, as shown in Section 4.3. (2) The modification of the geometry results in the change of pressure distributions significantly. Figure 4.12 shows the pressure distributions on two arbitrary sections by applying approximation 1 and one DOF inviscid model. Even if the slope of the geometry and pressure distribution are both kept continuous, the results are very different from those obtained by one DOF inviscid model.

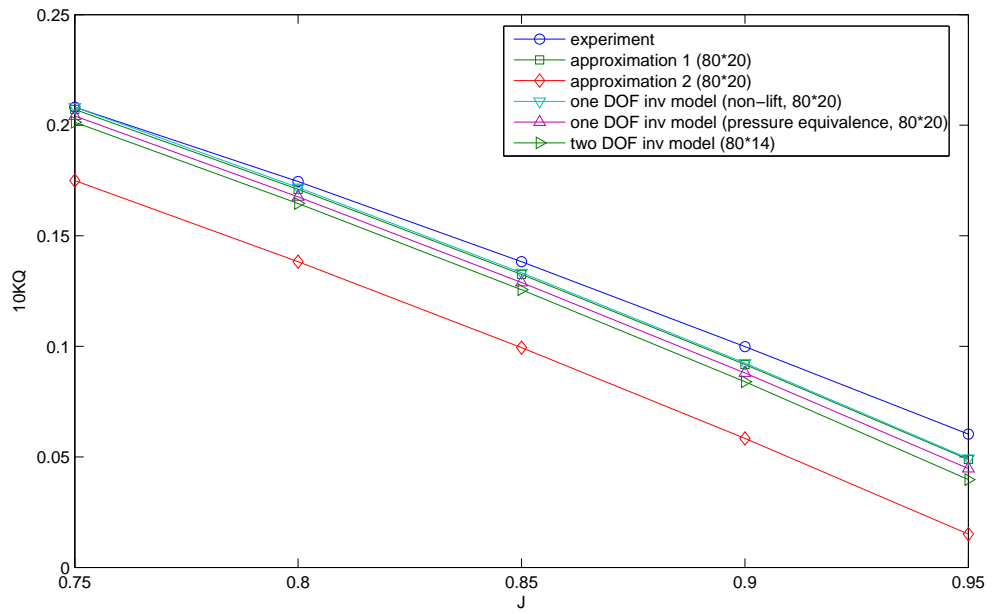
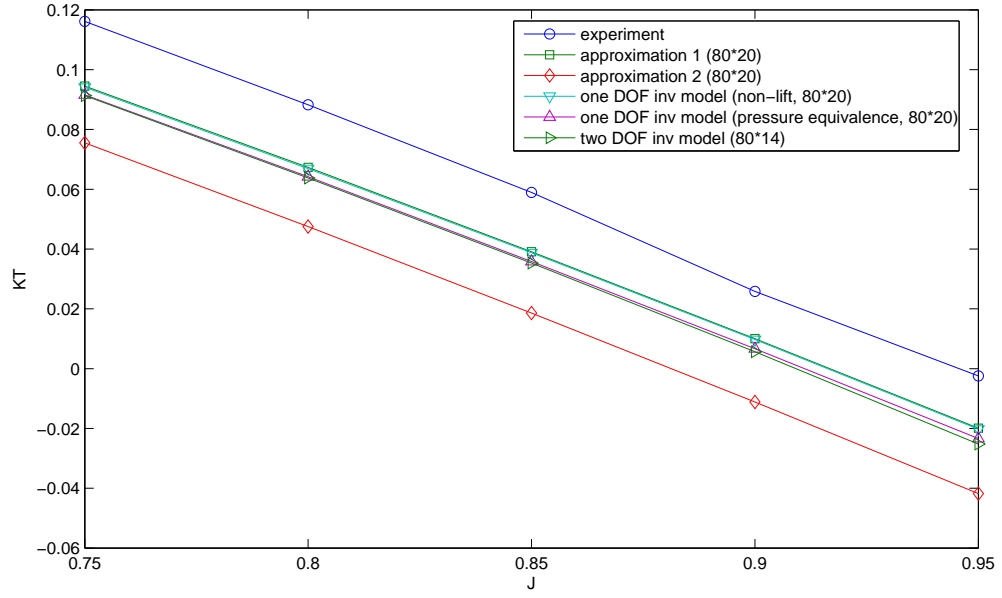


Figure 4.11: Results from one DOF inviscid model: (a) K_T , (b) K_Q

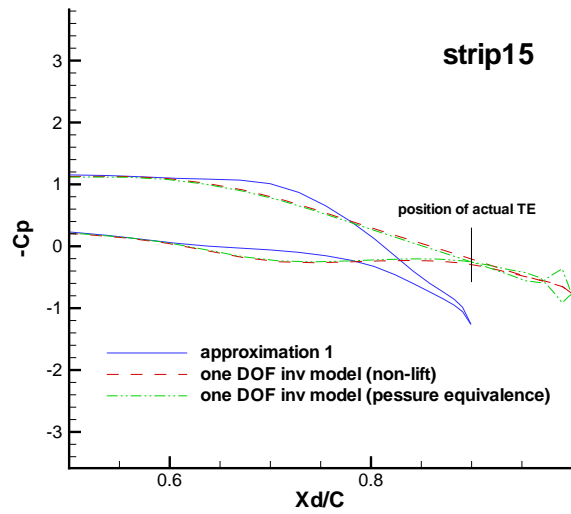
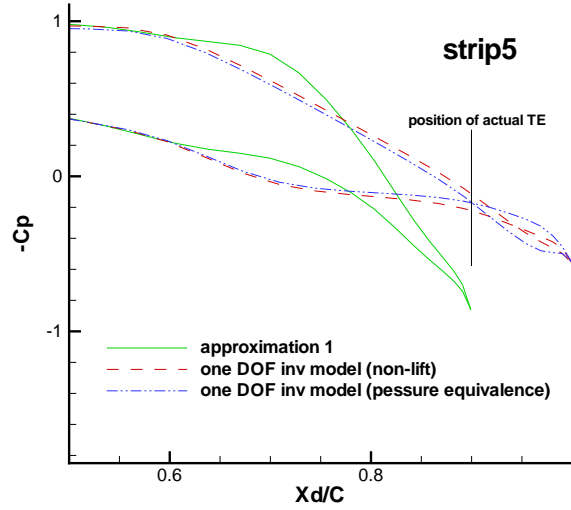


Figure 4.12: Pressure distributions on two arbitrary strips from approximation 1 at $J = 0.85$, span-wise positions of the strips: strip5: $r/R=0.3552$; strip15: 0.7712

4.3 BEM-viscous model

In this section, XFOIL is coupled with the inviscid solution to obtain the viscous results. Two models are used. First, a simple model is used, in which XFOIL is applied on top of the geometry from inviscid solution. Second, the one degree of freedom model, like the method used in 2D, is applied on the viscous results in each iteration.

4.3.1 A simple model

XFOIL is applied on top of the inviscid solution obtained by the one degree of freedom model (non-lift condition). The Reynolds number, based on the propeller diameter and inflow velocity, is set at 637000, which is the same as the experimental setting. The resulted K_T and K_Q are shown in Figure 4.13.

As shown in the figure, applying XFOIL on top of the one DOF inviscid solution helps to improve the K_T curve. K_Q curve is changed as well but does not show better behavior than inviscid results. Also, as discussed before, XFOIL does not help to improve the results from approximation 1. However, a disadvantage of this simple model exists that XFOIL influences the pressure distributions on the strips (original+extension). Therefore, the viscous pressure does not satisfy the non-lift condition, as shown in Figure 4.14.

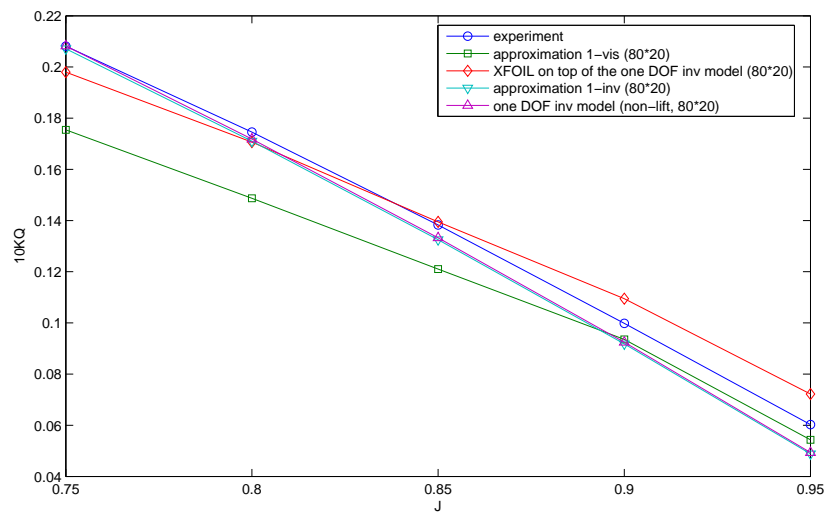
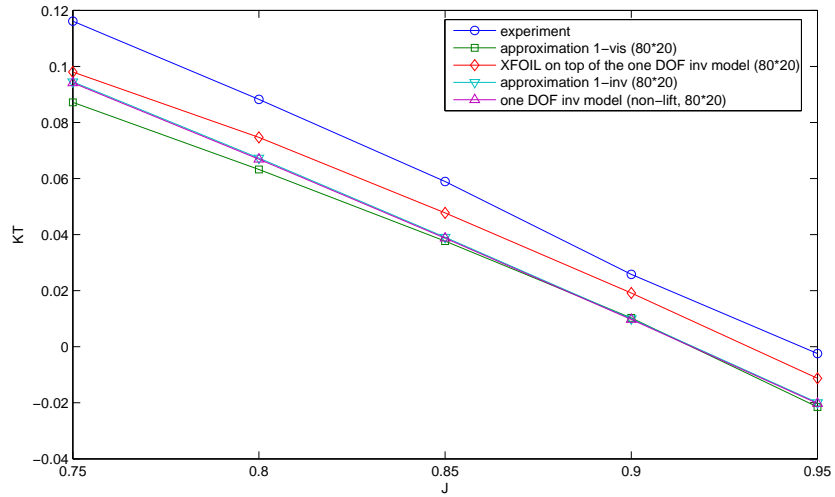


Figure 4.13: Results predicted by the simple viscous model: (a) K_T , (b) K_Q

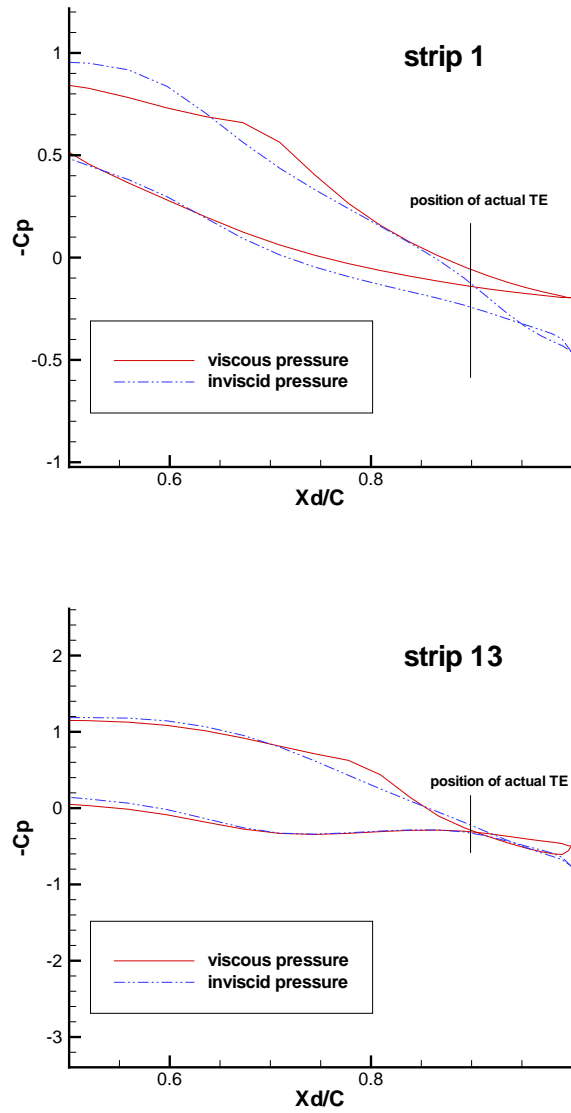


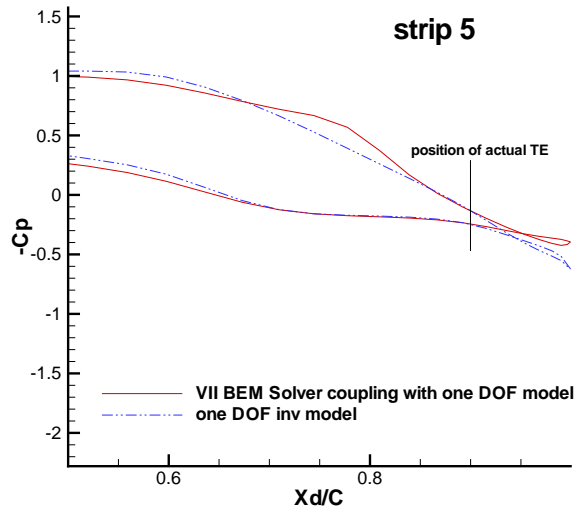
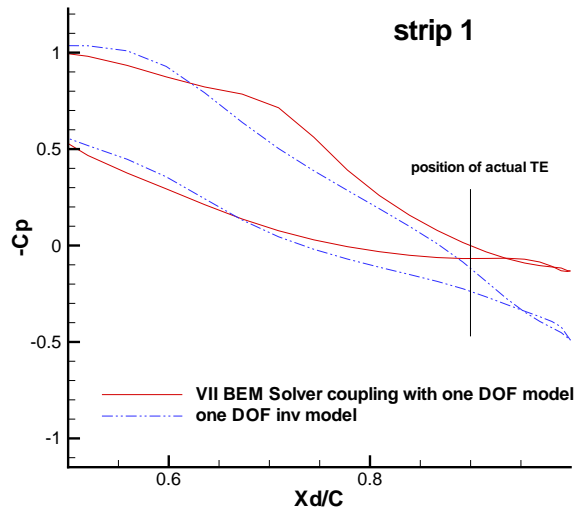
Figure 4.14: Pressure distributions on two arbitrary strips by applying XFOIL on top of one DOF inv model (non-lift), $J = 0.85$, 80×20 panels are used, span-wise positions of the strips: strip1: $r/R=0.1977$; strip13: $r/R=0.9109$

4.3.2 VII BEM Solver coupling with one degree of freedom model in 3D

In this model, XFOIL is applied on each iteration. In other words, one DOF model is applied on the viscous pressure so that in the end the viscous pressure distribution satisfies the non-lift condition. For example, the propeller A is modeled using 80×14 panels. At $J=0.85$, the pressure distributions on different strips are shown in the Figure 4.15.

The predicted K_T and K_Q from this model are shown in Figure 4.16. At five different values of J , the current model is applied using 110×14 panels. It can be seen that both K_T and K_Q are improved significantly at higher values of J .

It seems that not much benefit is gained by applying this model at lower values of J . However, there are many unknown factors that can have impact on the viscous results, such as the turbulent intensity level, transition point from laminar to turbulent flow, number of elements and so on. These unknown factors provides some uncertainties and their influences on the results are discussed below.



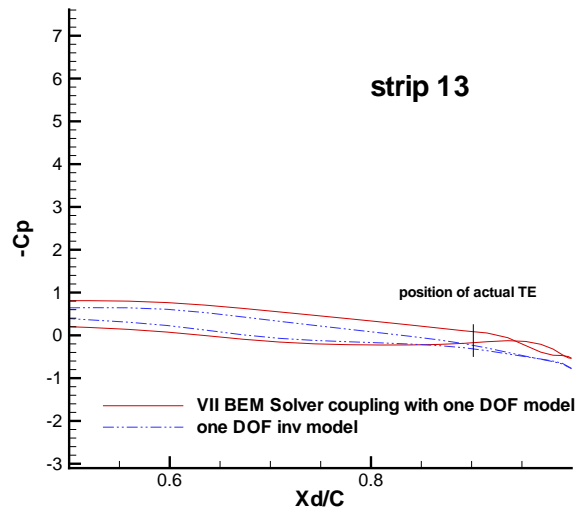
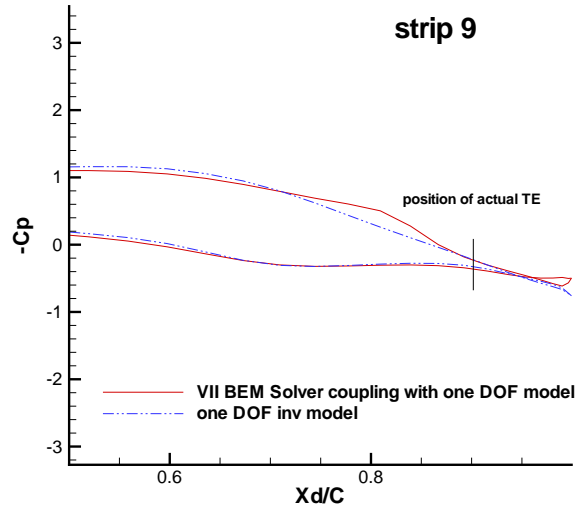


Figure 4.15: Pressure distributions by using VII BEM Solver coupling with non-lift condition at $J = 0.85$, 80×14 panels are used, span-wise positions of the strips: strip1: $r/R=0.1977$; strip5: $r/R=4354$; strip9: $r/R=6731$; strip13: $r/R=0.9109$

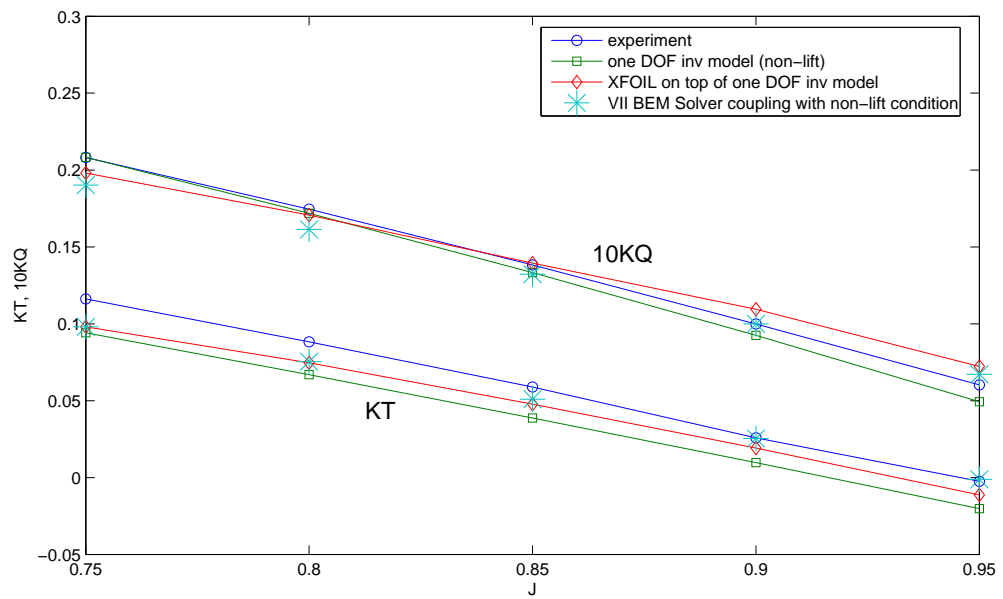


Figure 4.16: K_T and K_Q predicted by VII BEM Solver coupling with non-lift condition

Influence of turbulence level:

In XFOIL, the transition points from laminar to turbulent flow can be set as either forced or free transitions. Since no turbulent stimulator is used in this experiment, we used free transitions in all simulations. In the case of free transition, the position is controlled by the critical maximum amplification rate of the Tollmien Schlichting waves ($N_{critical}$). For example, $N_{critical}$ of MIT's water tunnel is 2.623 which corresponds to a one percent turbulence level. [Rice 1991]

It is found that different turbulence levels influence the pressure distributions near the transition point, resulting in different forces and moments. Figure 4.17 shows the pressure distribution on an arbitrary strip of propeller A (110*14 panels, $J = 0.75$) by using different $N_{critical}$ values. It can be seen that different transition positions are obtained from different values of $N_{critical}$. The predicted K_T and K_Q from these cases are listed in Table 4.1, which shows that K_T changes with different values of turbulence levels. Note that for this case, the experimental data for K_T and $10K_Q$ are 0.1161 and 0.2081, respectively.

Table 4.1: K_T and K_Q by using different turbulent levels at $J = 0.75$

$N_{critical}$	2.1	2.3	2.5	2.7	2.9	3.1	3.3
turbulent level	1.24%	1.14 %	1.05 %	0.97%	0.89%	0.82%	0.75%
K_T	0.0952	0.0962	0.0974	0.0981	0.0990	0.0998	0.1004
$10K_Q$	0.1899	0.1899	0.1901	0.1900	0.1900	0.1902	0.1901

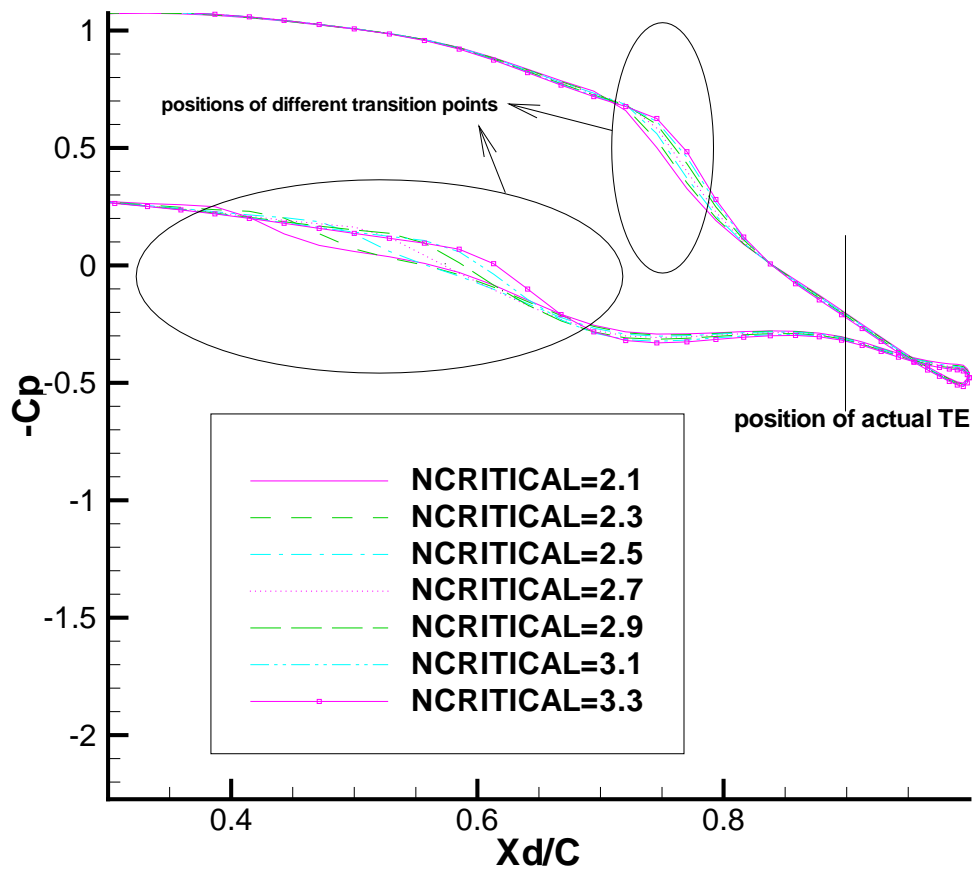


Figure 4.17: Pressure distributions on one arbitrary strip of propeller A by using different turbulent levels at $J = 0.75$

Influence of number of elements:

Although the inviscid results converge well with number of elements (discussed in Section 4.4), the viscous results are found to vary with number of elements, which is an internal deficiency of the viscous part of PROPCAV. Figure 4.18 shows the viscous pressure distribution on one arbitrary strip of propeller A ($J = 0.75$) by using different numbers of chord-wise elements. Different numbers of elements result in different transition points, which appears not to converge with increasing number of elements.

Table 4.2 shows the predicted K_T and K_Q by using different numbers of chord-wise elements. It can be seen that the number of elements has a larger impact on K_Q . Also, the results do not appear to converge with increasing number of elements.

With these uncertainties in XFOIL, it is hard to set the transition point from laminar to turbulent flow the same as that in the experiment. With different settings, the VII BEM Solver coupling with non-lift condition could give different results. For example, at $J = 0.75$, using less chord-wise elements and higher value of $N_{critical}$ helps to give results closer to the experiment data.

Table 4.2: K_T and K_Q by using different numbers of chord-wise elements at $J = 0.75$

number of panels	50*14	80*14	110*14	140*14	170*14	200*14
K_T	0.0995	0.0988	0.0980	0.0974	0.0962	0.0956
$10K_Q$	0.2037	0.1938	0.1902	0.1879	0.1857	0.1834

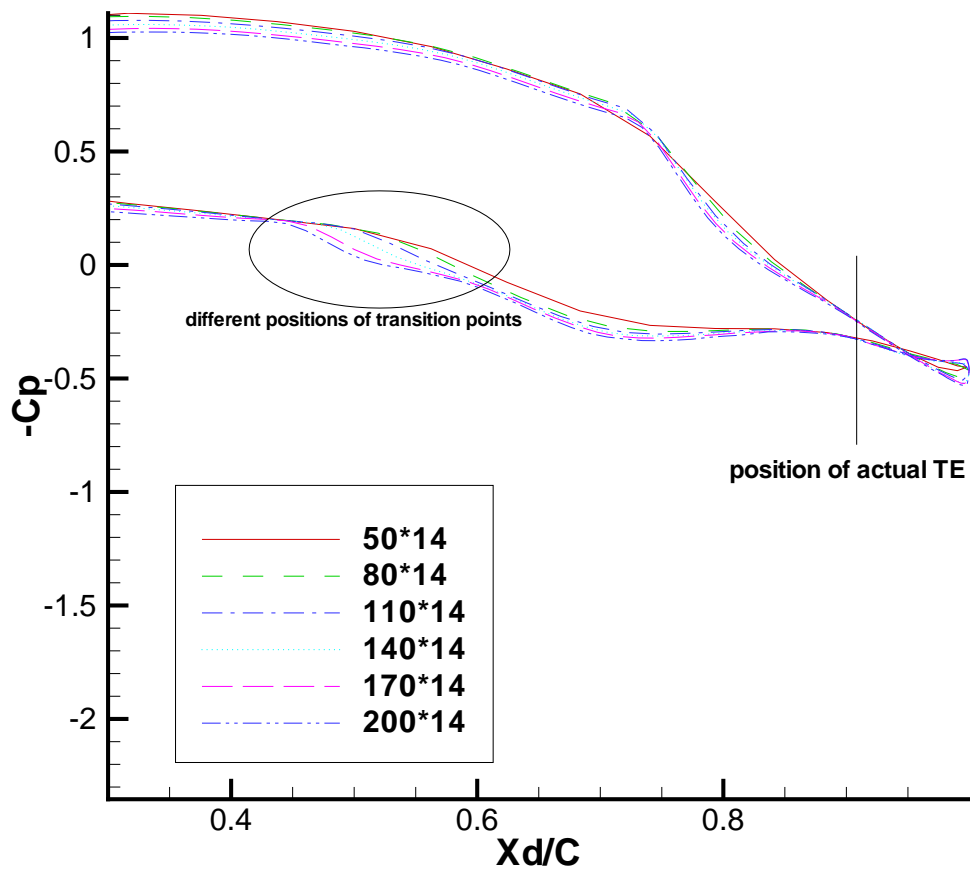


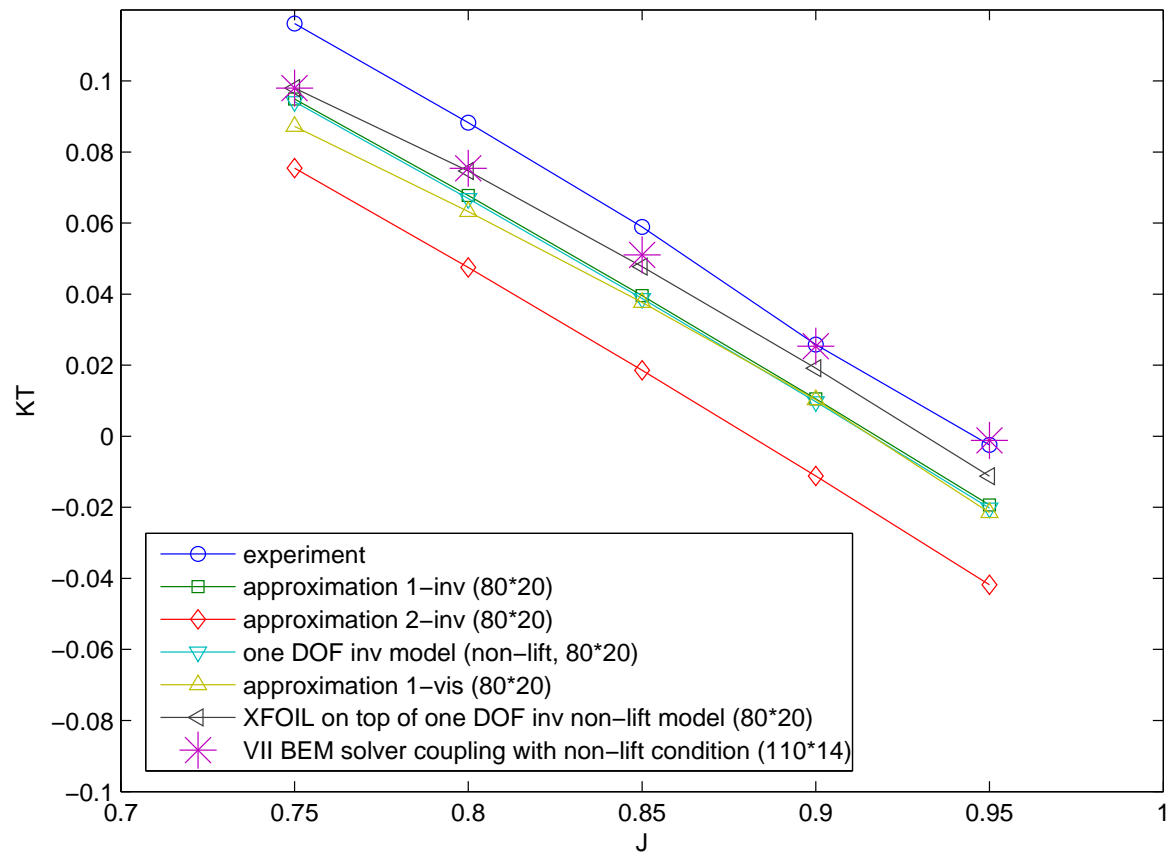
Figure 4.18: Pressure distributions on one arbitrary strip of propeller A by using different numbers of chord-wise elements at $J = 0.75$

In current applications, 110×14 panels are used for all five different values of J . The value of $N_{critical}$ is set at 2.623, which corresponds to the turbulence level in MIT's water tunnel, given that the turbulence level of this experiment was not known.

As a summary, the predicted K_T and K_Q from all discussed approaches are shown in Figure 4.19. And Table 4.3 gives the computational cost for all these methods. Note that all the cases listed in Table 4.3 are run on a single core of a quad-core CPU (2.5GHZ Intel Xeon) with 16GB RAM and 80×14 panels are used.

Table 4.3: Computational cost for approaches in 3D

Cases	closed section (inviscid)	closed section (viscous)	open section (one DOF inviscid)	open section (one DOF viscous)
CPU time	0.56 min	0.61 min	about 1 hour, depending on the initial solution	about 2.5 hours, depending on the initial solution



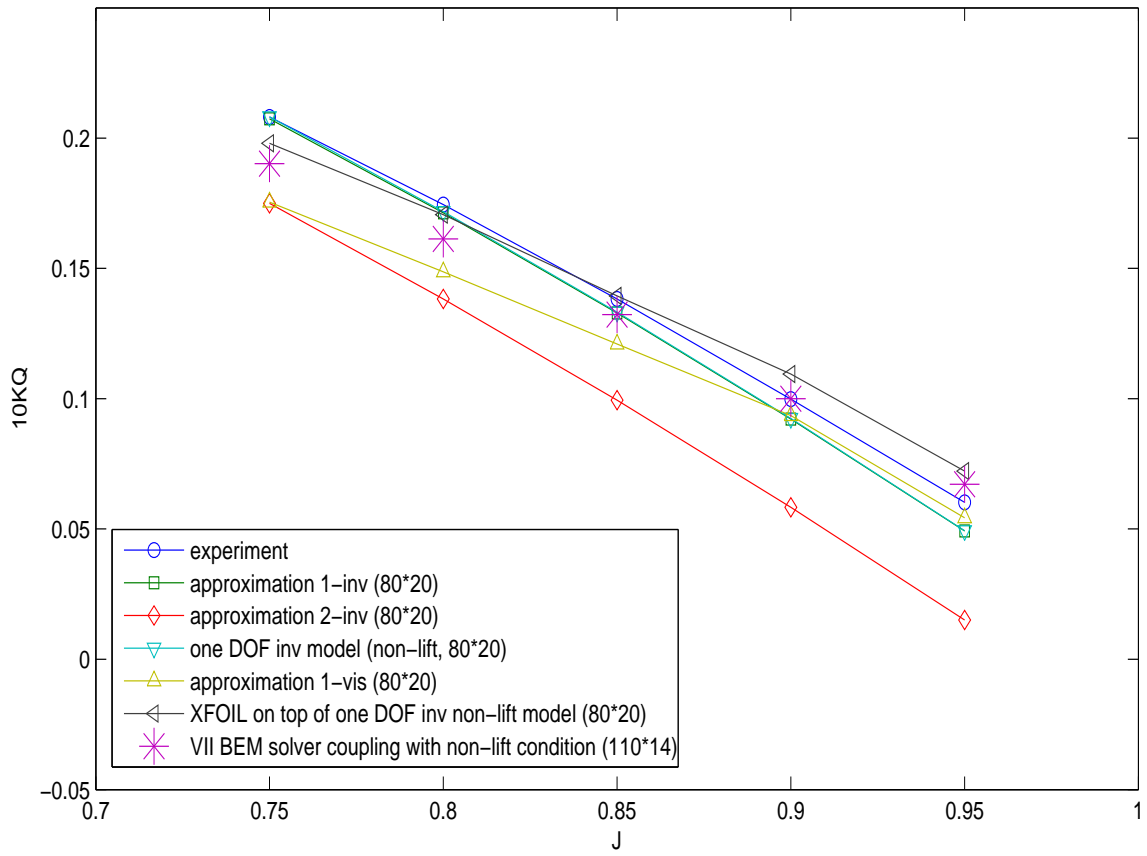


Figure 4.19: K_T and K_Q predicted by all discussed approaches

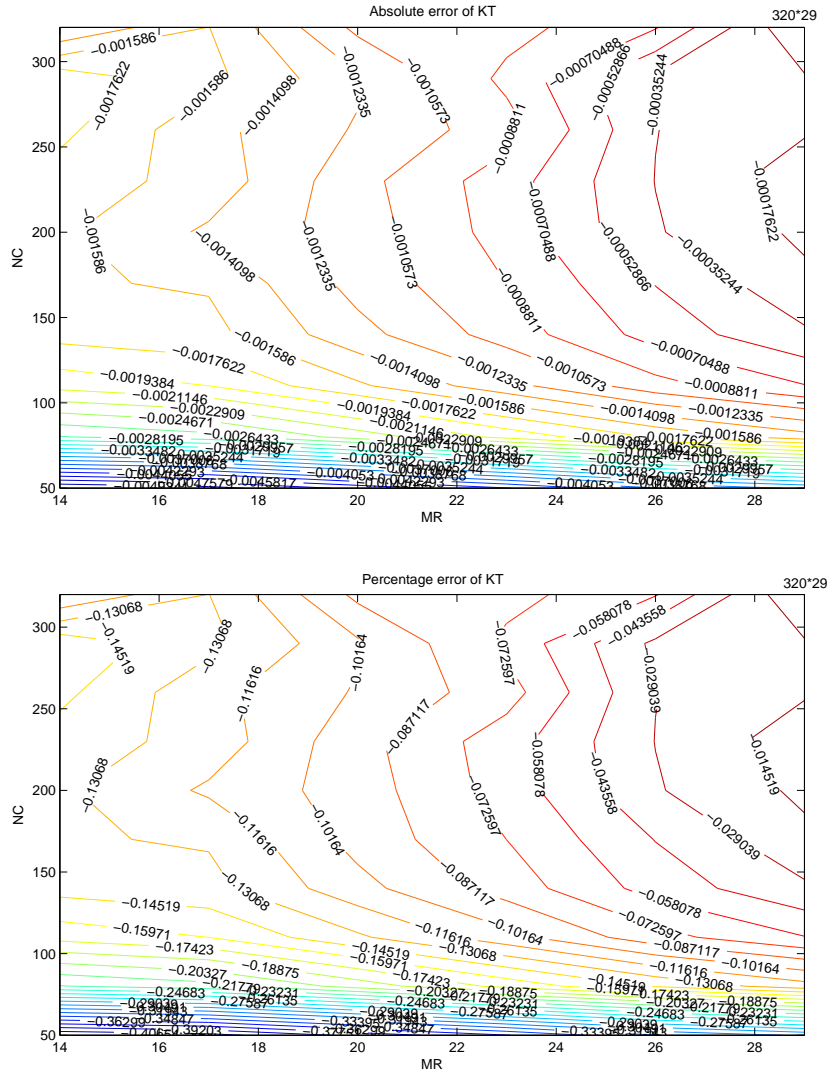
4.4 Convergence study

In this section, extensive convergence studies are performed in terms of pressure distributions, forces and moments. The inviscid solution is used to avoid the influence of XFOIL on the results.

4.4.1 Convergence contour for propeller A with modified blade sections

A convergence study of K_T and K_Q for the same propeller but with closed sections of NACA a=0.8 camber and NACA00 thickness distribution is performed. This study shows an approximation of the convergence rate for propeller A. The reason for using a closed section, instead of the real section, is to reduce the computational cost. On the other hand, this study excludes the influence of current (one DOF inv model) method. Therefore, it serves as a comparison of the convergence of K_T and K_Q by using current method, which will be discussed later.

For this case, $J = 0.9$, the results obtained by using 320*29 panels are regarded as the accurate results. The contour lines for absolute error and percentage error of K_T and K_Q with number of span-wise (MR) and chord-wise (NC) elements are shown in Figure 4.20 and Figure 4.21. The absolute error, as shown in the figure, does not change much with number of elements. However, the percentage error of K_T seems large in this case, which is due to the fact that the “accurate” value of K_T is near zero. This fact will be discussed later.



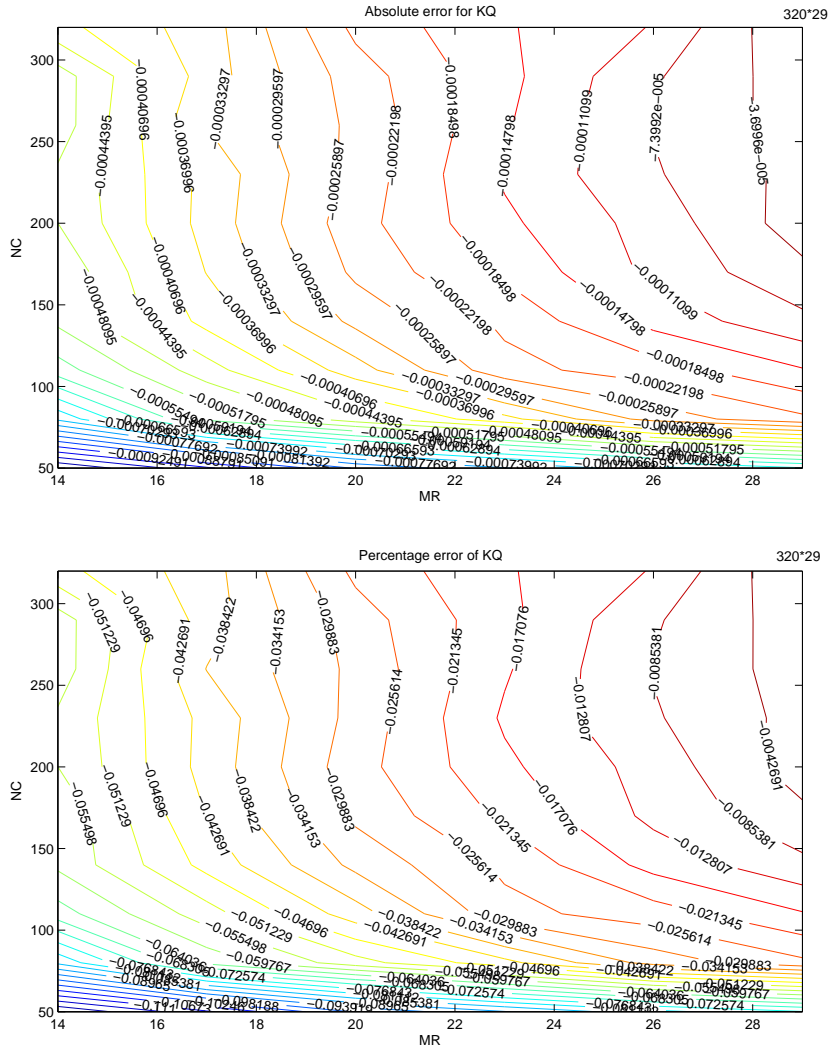


Figure 4.21: Error of K_Q by using NACA00 sections at $J = 0.9$, modified Propeller A: (a) absolute error, (b) percentage error

4.4.2 Convergence study of propeller A

In this section, the convergence study is performed directly using propeller A. For this case, $J = 0.9$ and 80×20 panels are used. The one DOF inv model with pressure equivalence condition is applied. Other models can be applied using the similar approach.

4.4.2.1 Convergence study of propeller A with number of chord-wise elements

Four convergence studies of propeller A with number of chord-wise elements are performed, as discussed below.

First of all, evaluating base pressures is a most important issue in current approach. It is worthwhile to study the convergence of base pressures with number of panels.

Figure 4.22 shows the convergence of base pressures with number of chord-wise elements. The base pressure curve, as shown in the figure, gets converged with increase of number of chord-wise elements. For this case, increasing the number of chord-wise elements reduces the base pressure, but the effect is not significant.

Second, the convergence of pressure distributions with number of chord-wise elements is studied. The pressure distributions on three arbitrary strips with different numbers of chord-wise elements are shown in Figure 4.23. Since the torque and thrust of the propeller are obtained by integrating the pressure and viscous forces, of which the first part is more important, the convergence

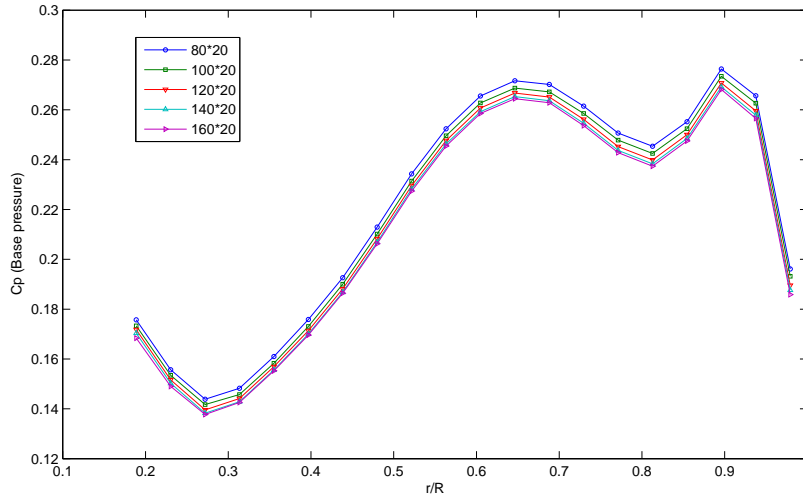


Figure 4.22: Convergence of base pressures with number of chord-wise elements at $J = 0.9$, Propeller A

of pressure distributions is a good sign on whether the forces and moments converge well.

As shown in the Figure 4.23, the pressure distributions converge well with increase of number of chord-wise elements. Even though the pressure distributions on the extensions vary with different numbers of elements, the pressures on the actual foil remains the same. (Note that only the pressure distributions from $x=0$ to $x=0.9$ are important, not including the extensions.)

Third, Table 4.4 shows the convergence of K_T and K_Q with number of chord-wise elements. We can observe that K_T and K_Q get converged with increase of number of chord-wise elements. However, the differences of K_T among these cases seem large. These “large” differences, which are related to

the fact that the actual value of K_T is near zero at $J = 0.9$, can be justified as something we expect. The reasons are listed as below.

(1) These differences in K_T are consistent with the convergence contour for standard NACA00 sections. For instance, Figure 4.20 shows that $\Delta K_T \approx 0.118$ between 80×20 and 160×20 panels, which is a little smaller but comparable to the ΔK_T shown in Table 4.4.

(2) These difference in K_T are consistent with those by applying approximation 1 to the same propeller. Specifically, for using approximation 1, a grid of 80×20 gives K_T as 0.0100, while a grid of 160×20 gives K_T as 0.0116. The difference is similar as that for propeller A.

(3) In the above two cases (NACA00 and approximation 1), the one DOF inviscid model is not included. The only source of the error is from the difference in pressure distribution. In fact, although the differences of pressure distributions are not visible in a global figure, it exists locally.

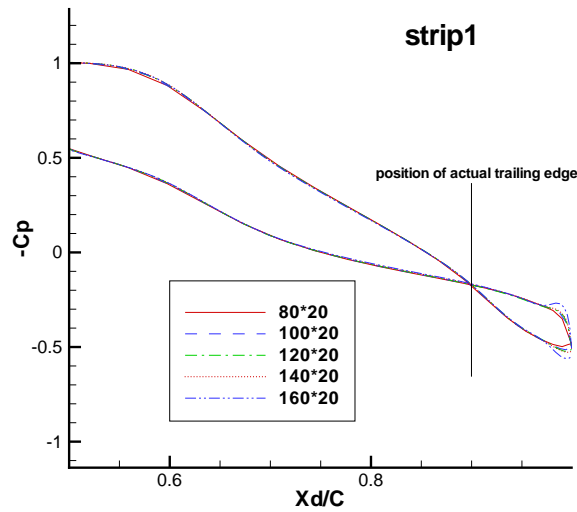
(4) Since the thrust is obtained from a summing operation (integration of pressure and viscous forces), considering the absolute error makes more sense. In other words, the percentage error varies greatly with J but the absolute error does not. For example, Table 4.5 summarizes K_T if we run the case using approximation 1 at $J = 0.75$ and $J = 0.9$. The absolute error keeps similar, with the percentage error much smaller at $J = 0.75$.

Table 4.4: Convergence of K_T and K_Q with number of chord-wise elements at $J = 0.9$

Number of panels	80*20	100*20	120*20	140*20	160*20
K_T	0.00658	0.00743	0.00784	0.00811	0.00824
$10K_Q$	0.08793	0.08947	0.09019	0.09118	0.09144

Table 4.5: Summary of K_T using different panels at $J = 0.75$ and $J = 0.9$

Number of panels	80*20	100*20	120*20	140*20	160*20
K_T at $J = 0.75$	0.09450	0.09507	0.09527	0.09542	0.09552
K_T at $J = 0.9$	0.01000	0.01081	0.01118	0.01144	0.01157



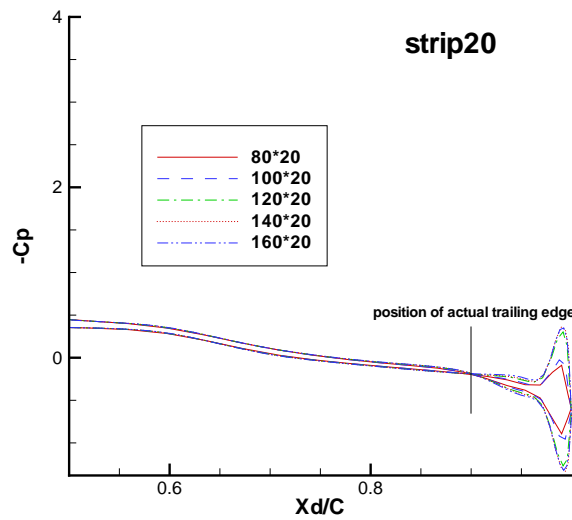
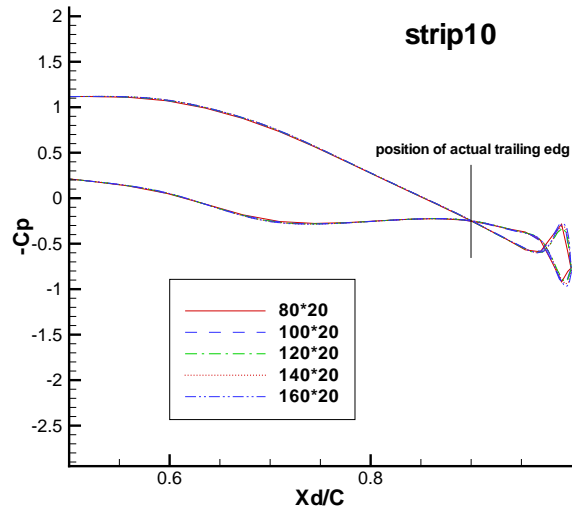


Figure 4.23: Convergence of pressure distributions on three arbitrary strips with number of chord-wise elements at $J = 0.9$, propeller A

Fourth, the convergence of two parts of K_T with number of chord-wise elements is studied, respectively. Figure 4.24 shows the convergence study of K_T due to pressure distributions on pressure and suction sides. Each point on the curve shows the contribution to total K_T due to the force of a strip at a certain span-wise position. Figure 4.25 shows the convergence study of K_T due to base pressure, and the curve is generated using the same manner.

It is found that the first part of K_T (due to pressure distributions on pressure and suction sides) is the main source of total K_T difference, which is consistent with the discussion before. Also, the first part of K_T is much larger than the second part for most of the strips. However, the second part of K_T (due to base pressure) is important for strips where the first part is small. For examples, Figure 4.26 shows the two parts of K_T at the first few strips near the hub, where the two parts of K_T are comparable.

Note that in Figures (4.24), (4.25) and (4.26), only the pressure forces on a single blade are included. Also, a different form of nondimensionalization is used. The total K_T can be obtained by

$$K_T(total) = -(\text{sum of points in Figure 4.24 and 4.25}) \times J^2/8 \quad (4.7)$$

$$\times 5 \text{ (number of blades) } + \textit{viscous forces} + \textit{tip forces}$$

Where the tip forces are obtained by extrapolation.

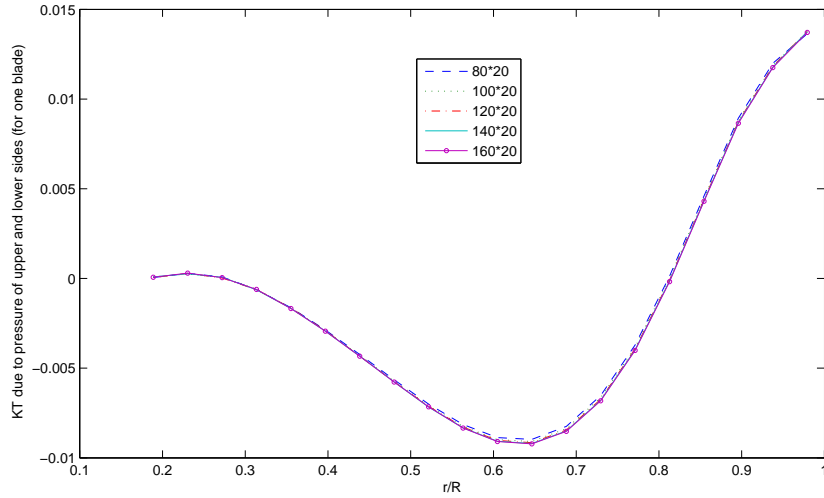


Figure 4.24: Convergence study of K_T due to pressure distributions on pressure and suction sides at $J = 0.9$, Propeller A

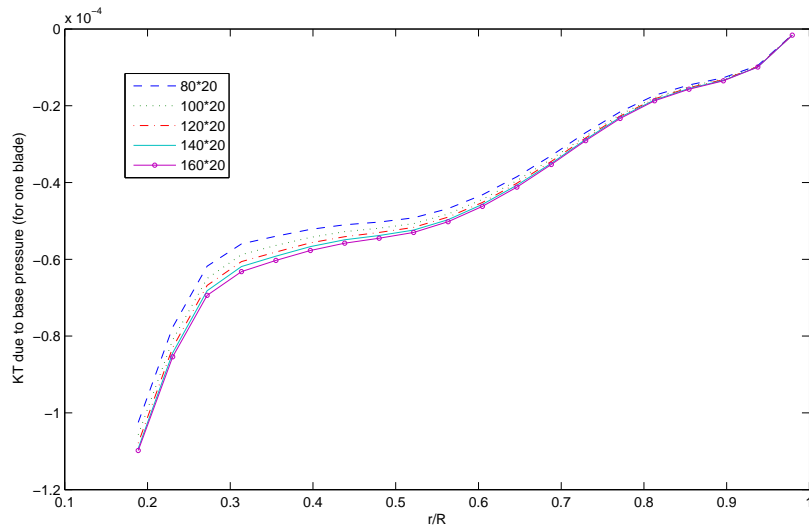


Figure 4.25: Convergence study of K_T due to base pressure at $J = 0.9$, Propeller A

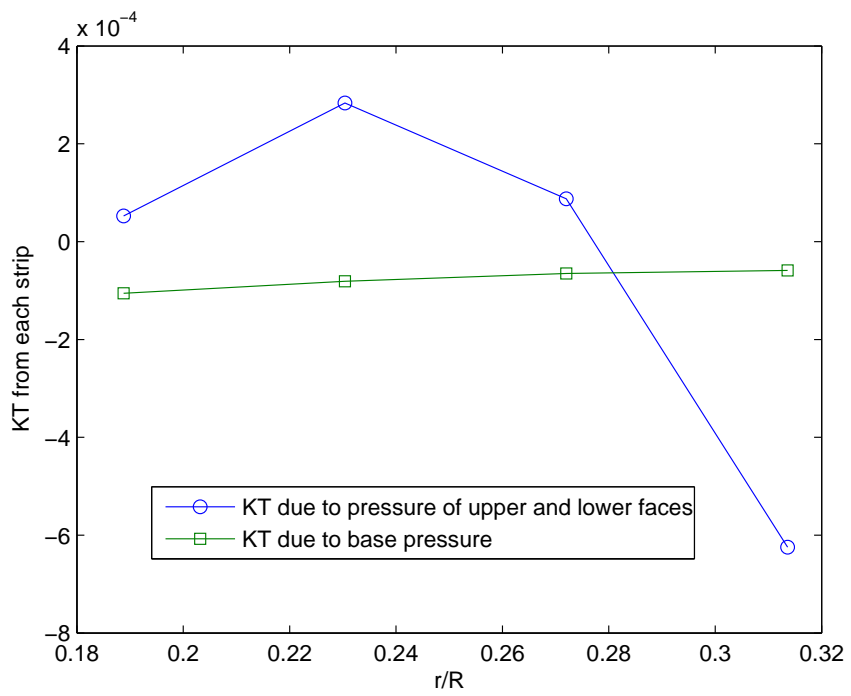


Figure 4.26: Comparison of two parts of K_T at the first few strips near the hub at $J = 0.9$, Propeller A

4.4.2.2 Convergence study of propeller A with number of span-wise elements

Figure 4.27 shows the base pressures by using different numbers of span-wise elements for $J = 0.9$. The convergence is good globally except the few strips near the tip. However, this is unavoidable because boundary element method always has a hard time in predicting the tip effects of propellers.

Table 4.6 shows the convergence of K_T and K_Q with number of span-wise elements. We can observe that the changes of K_T and K_Q with number of span-wise elements are much smaller than those with chord-wise elements. Also, instead of increasing or decreasing monotonically, K_T and K_Q fluctuates with increase of number of span-wise elements. It is reasonable to believe that these fluctuations of forces and moments come from the fluctuations of pressure distributions on the few strips near the tip.

Table 4.6: Convergence of K_T and K_Q with number of span-wise elements at $J = 0.9$

Number of panels	80*20	80*24	80*28
K_T	0.00658	0.00675	0.00646
$10K_Q$	0.08793	0.08902	0.08860

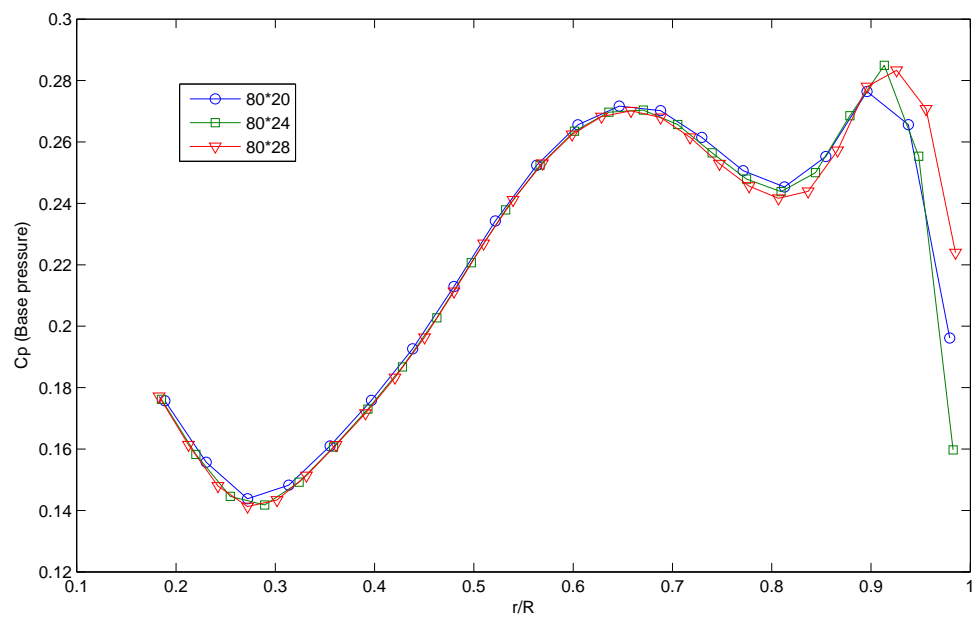


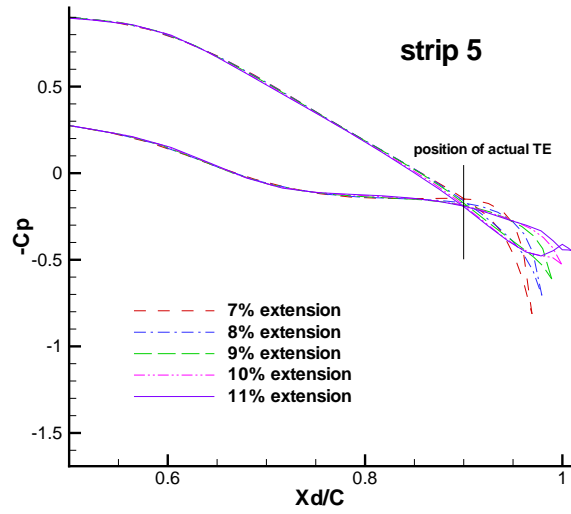
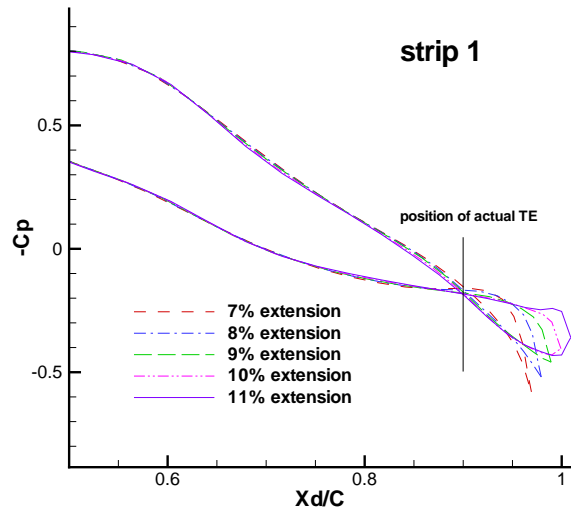
Figure 4.27: Convergence of base pressures with number of span-wise elements at $J = 0.9$

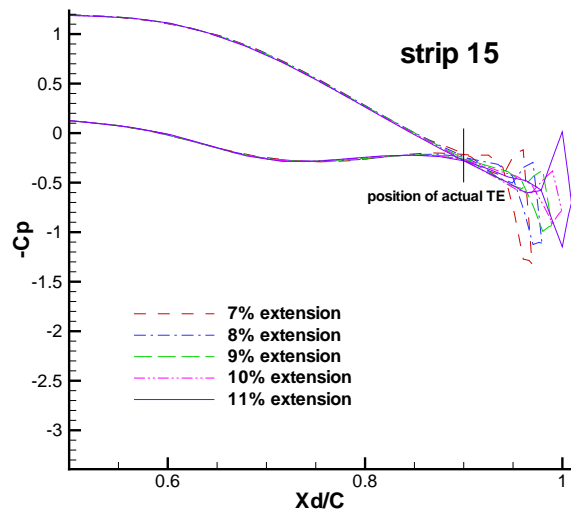
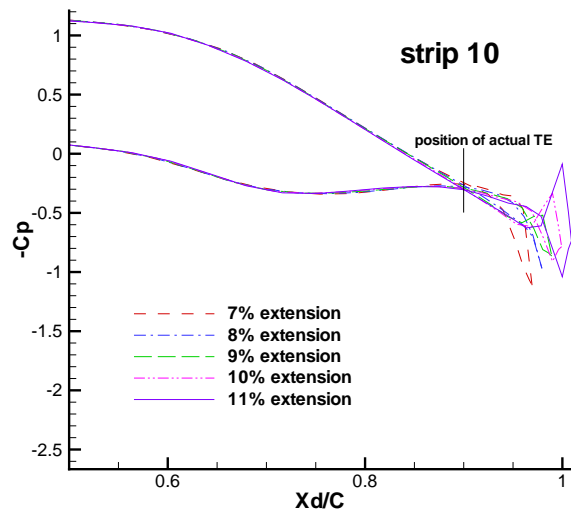
4.4.2.3 Convergence study of different lengths of extensions

In all the above cases, extensions of 10% of the chord lengths are used. It is worthwhile to see whether a different length of the extension results in different pressures, forces and moments. In this study, 80*20 panels are used and $J = 0.75$.

Figure 4.28 shows the pressure distributions on five arbitrary strips of propeller A by using different lengths of extensions. It can be seen that the pressure distributions do not change much on the actual propeller surface, though they vary a lot from one another on the extensions. The resulted K_T and K_Q by using different lengths of extensions are shown in Figure 4.29. As we expect, the differences among these K_T and K_Q are small, given the small differences in pressure distributions.

From the analysis above, the effect of extension lengths on the pressures, forces and moments is found to be very small. This study is useful because it allows us to use arbitrary lengths of extensions in a reasonable region, without much change of the results.





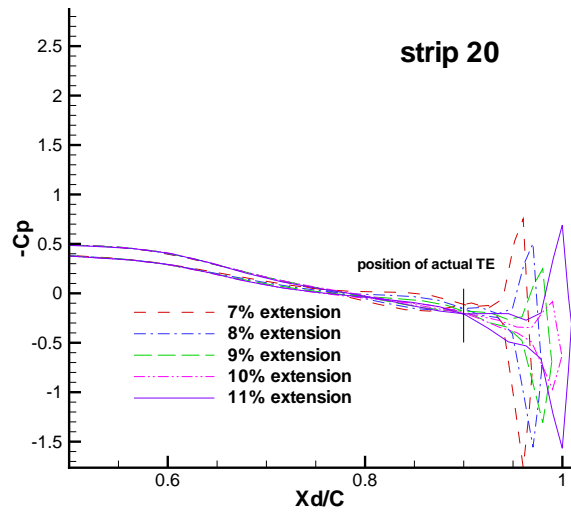


Figure 4.28: Pressure distributions on five arbitrary strips of propeller A by using different lengths of extensions at $J = 0.75$, Propeller A, span-wise positions of Propeller A: strip1: $r/R=0.1888$; strip5: $r/R=0.3552$; strip10: $r/R=0.5632$; strip15: $r/R=0.7712$; strip20: $r/R=0.9792$

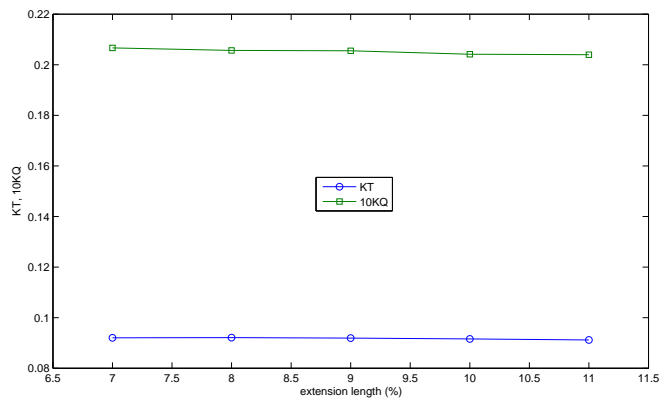


Figure 4.29: K_T and K_Q by using different lengths of extensions at $J = 0.75$, Propeller A

Chapter 5

VII BEM Solver with application to partial-cavitating hydrofoils

This chapter is an independent part from the previous ones on non-zero trailing edge thickness. It includes the application of the VII BEM Solver to partial-cavitating hydrofoils. Also, a RANS solver coupled with a mixture model (Fluent) is used to solve the same problem. The results from the two approaches are compared.

5.1 Fluent simulation of partial cavitation

In this section, an introduction to the Fluent cavitation model is given, and the results from this model is presented.

5.1.1 Description of Fluent cavitation model

This section gives a brief explanation of the Fluent cavitation model. For more details, refer to [Singhal et al. 2002, Rhee et al. 2005, Fluent 2007].

The basic approach of the cavitation model consists of using the Navier-Stokes equations for the mixture phase, a transport equation governing water vapor mass fraction, as well as the extra turbulent model equations.

Mixture equations

In most engineering application, the operating fluid is assumed to be a mixture of liquid, vapor and a finite amount of non-condensable gases (e.g. dissolved gases). The continuity equation governing the mixture is given by

$$\frac{\partial}{\partial t}(\rho_m) + \nabla \cdot (\rho_m \vec{v}_m) = 0 \quad (5.1)$$

Where \vec{v}_m is the mass-averaged velocity:

$$\vec{v}_m = \frac{\sum_{k=1}^3 \alpha_k \rho_k \vec{v}_k}{\rho_m} \quad (k = 1, 2, 3 \text{ corresponding to water, vapor and gas})$$

ρ_m is the mixture density:

$$\rho_m = \sum_{k=1}^3 \alpha_k \rho_k$$

And α_k is the volume fraction of phase k .

Also, the momentum equations for the mixture can be obtained by summing the individual momentum equations for all the phases:

$$\frac{\partial}{\partial t}(\rho_m \vec{v}_m) + \nabla \cdot (\rho_m \vec{v}_m \vec{v}_m) = -\nabla p + \nabla \cdot [\mu_m (\nabla \vec{v}_m + \nabla \vec{v}_m^T)] + \rho_m \vec{g} + \vec{F} \quad (5.2)$$

Where μ_m is the viscosity of the mixture:

$$\mu_m = \sum_{k=1}^3 \alpha_k \mu_k$$

For current application,

$$\nabla \cdot \nabla \vec{v}_m^T = 0 \text{ due to incompressibility}$$

$$\rho_m g = F = 0, \text{ no external force}$$

Effect of non-condensable gases (NCG)

Even a small amount of NCG can have significant effects on cavitation. [Watanabe and Prosperetti 1994] The primary effect is due to the expansion of gas at low pressures which can lead to significant values of local gas volume fraction, and thus have considerable impact on density, velocity and pressure distributions. In the cavitation model, this effect is accounted by treating NCG using ideal gas law. The secondary effect can be via increases in the phase-change threshold pressure. This has been neglected due to lack of a general correlation.

Effect of turbulence (taken from [Singhal et al. 2002])

Several experimental investigations have shown significant effect of turbulence on cavitating flows [Keller and Rott 1997]. [Singhal et al. 1997] reported a numerical model, using a probability density function (PDF) for accounting the effects of turbulent pressure fluctuations. This approach required: (a) estimation of the local values of the turbulent pressure fluctuation as:

$$P'_{turb} = 0.39\rho k$$

(b) Computations of time-averaged phase-change rates by integration of instantaneous rates in conjunction with assumed PDF for pressure variation with time. In the Fluent model, this treatment has been simplified by simply

raising the phase-change threshold pressure value as:

$$P_v = P_{sat} + P'_{turb}/2$$

Where P_{sat} is the saturation pressure (the pressure for a corresponding saturation temperature at which a liquid boils into its vapor phase) without turbulent effect.

Transport Equation for Vapor Mass Fraction

The vapor mass fraction, f , is governed by a transport equation:

$$\frac{\partial}{\partial t}(\rho_m f) + \nabla \cdot (\rho_m \vec{v}_v f) = \nabla \cdot (\gamma \nabla f) + R_e - R_c \quad (5.3)$$

Where \vec{v}_v is the velocity vector of the vapor phase, γ is the effective exchange coefficient, corresponding to diffusion of vapor phase. R_e and R_c are the vapor generation and condensation rates. The expressions for both are derived from the Rayleigh-Plesset equations. [Simonin and Viollet 1990] Using \sqrt{k} (square root of turbulent kinetic energy) as a characteristic velocity and with consideration of turbulent effects, they are given as:

$$\text{when } p < p_v \quad R_e = C_e \frac{\sqrt{k}}{\sigma} \rho_l \rho_v \sqrt{\frac{2(p_v - p)}{3\rho_l}} (1 - f_v - f_g)$$

$$\text{when } p > p_v \quad R_c = C_c \frac{\sqrt{k}}{\sigma} \rho_l \rho_v \sqrt{\frac{2(p - p_v)}{3\rho_l}} f_v$$

Where σ is the surface tension coefficient of the liquid, and C_e and C_c are empirical constants with $C_e = 0.02$ and $C_c = 0.01$.

Finally, the relation between the mass fraction and the volume fraction is given by

$$\alpha_i = f_i \frac{\rho}{\rho_i} \quad (5.4)$$

Turbulence modeling

It is worthwhile to point out that the equations shown above are the mean equations without considering the fluctuations of the variables. (The reason for not doing this is to give a clear picture of the cavitation model) However, for turbulence modeling, Reynolds Averaging needs to be applied. For this application, Reynolds Stress Model (RSM) is used, which solves five extra equations for a 2D problem. Specifically, it models the evolutions of four Reynolds Stress components and the turbulent dissipation rate. Due to the symmetry condition in 2D (statistics is invariant with reflection of the axis normal to the 2D plane), we can obtain that $\langle uv \rangle = \langle vw \rangle = 0$. Therefore, the remaining Reynolds Stress components modeled are $\langle uu \rangle$, $\langle vv \rangle$, $\langle ww \rangle$ and $\langle uv \rangle$.

5.1.2 Fluent setting

Geometry and Grid

In present work, the hydrofoil used is a NACA00 section, with maximum thickness chord ratio $t/c = 0.04$ and maximum camber chord ratio $cam/c = 0.02$. The computational domain is $[-5,10]$ horizontally and $[-5,5]$ vertically, as shown in Figure 5.1 with the boundary conditions. GAMBIT is used for building the grid. As shown in Figure 5.2, a structured-grid zone

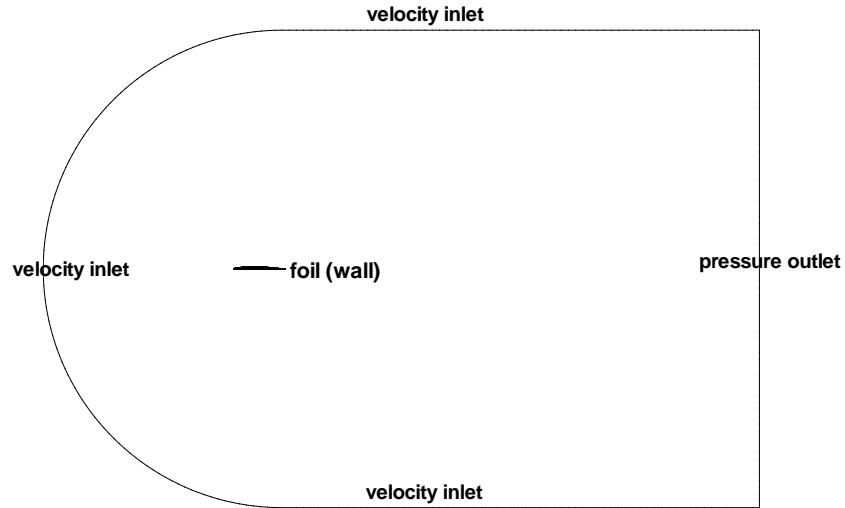


Figure 5.1: Computational domain and boundary conditions

is built near the hydrofoil and the thickness of the first layer is $O(1 \times 10^{-4})$, which gives the value of wall y^+ at $O(20)$. An unstructured-grid zone is built in the rest of the domain. The total number of cells is 101840.

Fluent running conditions

For spatial discretization, the schemes used are shown in the table 5.1. It should be pointed out that the second order upwind scheme is not available for vapor fraction. The PRESTO! (PREssure STaggerring Option) scheme used for pressure discretization is a scheme similar in spirit to the staggered-grid scheme. Also, SIMPLE is used for pressure-velocity coupling.

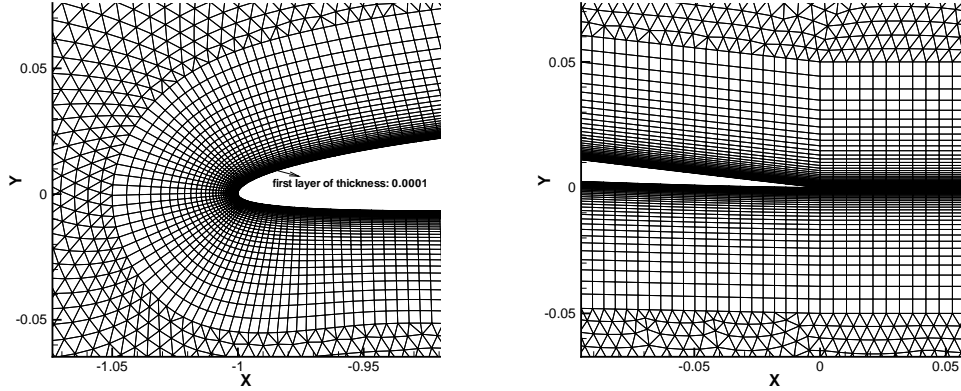


Figure 5.2: Grid near the trailing edge and leading edge: (a) leading edge, (b) trailing edge

Table 5.1: Spatial discretization in Fluent

Density, momentum, Reynolds stress, turbulent dissipation rate	Second order upwind
Vapor fraction	First order upwind
Pressure	PRESTO!

Table 5.2 gives some physical parameters used in this Fluent simulation. These values corresponds to the temperature $T = 300K$. The operating (ambient) pressure is set as 50000 Pa, which corresponds to a cavitation number $\sigma = \frac{p_\infty - p_v}{(1/2)\rho v^2} = 0.955$. (inflow velocity=10m/s, angle of attack=3 degrees)

Since the nature of cavitation restrains the steady state solution, (e.g. the closure of the cavity fluctuates as predicted by the reentrant model.) Unsteady solver is used to seek a quasi-steady solution. First order implicit scheme is used for time discretization, which is supposed to be sufficient for

Table 5.2: Physical parameter used in the Fluent simulation

Water vaporization pressure	2367.8 Pa
Surface tension coefficient	0.0717N/m
Non-condensable gas mass fraction	1.5×10^{-5}

most problems [Fluent 2007]. At each time step, the residuals for all the unknowns (pressure, velocities, Reynolds Stresses, turbulent dissipation rate) are set to be 10^{-6} .

Finally, fourteen cores of quad-core CPUs (2.5GHZ Intel Xeon) are used for this run. It takes about 20 hours for 30000 time steps. ($dt=0.0005$, to ensure good convergence at each time step)

5.1.3 Results

In the unsteady calculation, the lift coefficient $C_l = \frac{lift}{(1/2)\rho v^2 \cdot 1}$ is set as a monitor, whose time variance behavior shows whether the calculation reaches the quasi-steady state. Figure 5.3 shows the variance of C_l in 30s. We can observe that after 10s, C_l becomes nearly a constant, with only a small amount of fluctuation which is shown in Figure 5.3(b). We call this state quasi-steady state because it is not steady in nature due to the fluctuation of cavity closure. The small fluctuation of C_l is a good indicator of this behavior. However, the amount of the fluctuation predicted by the mixture model is much smaller than that from the experiments [Tulin and Hsu 1980]. Hereafter, all the results are corresponding to this quasi-steady state.

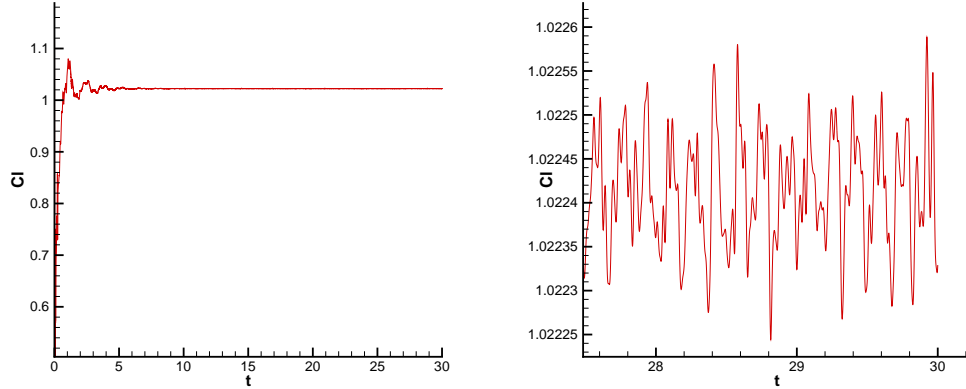


Figure 5.3: Time variance of lifting coefficient for $\sigma = 0.955$: (a) global view, (b) “quasi-steady” state

The y^+ of the first grid point near the foil is shown in Figure 5.4. They are in the order of $O(20)$ and a standard wall function is used for the near wall treatment.

The pressure distribution near the foil is shown in Figure 5.5. In (a) the blue region (low pressure area) indicates the location where cavitation occurs. The cavity length is about 0.27. Note that the water vaporization pressure 2367.8 Pa is only reached very locally at the foil leading edge. An explanation is that the vaporization pressure happens locally when the cavitation is triggered. Then the cavity bubble grows to form the whole cavity region. After the cavity region is fully developed, the pressure inside the cavity region changes slowly in space, (it does not remain a constant in this mixture model because turbulent effects raise the phase-change threshold pressure value) which is shown more clearly in (b). However, at the right end of the cavity bubble, the pressure

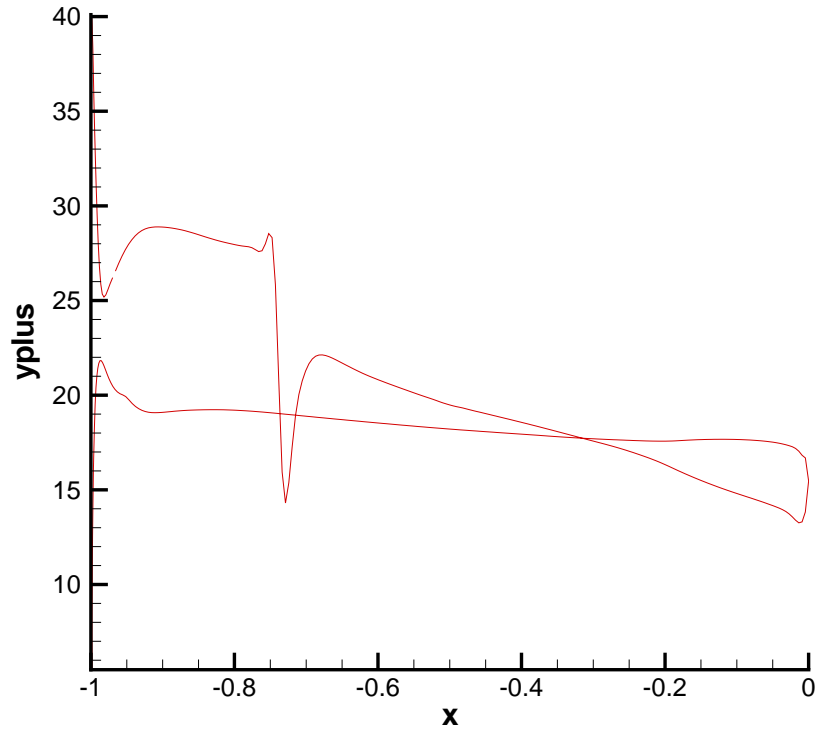


Figure 5.4: y^+ of the first grid point near the foil

gradient increases abruptly. These local high pressure gradients are consistent with the fluctuation of the cavity closure.

More results about the pressure distribution on the foil, the volume fraction distribution are discussed in Section 5.2, with the comparison with results from BEM solver.

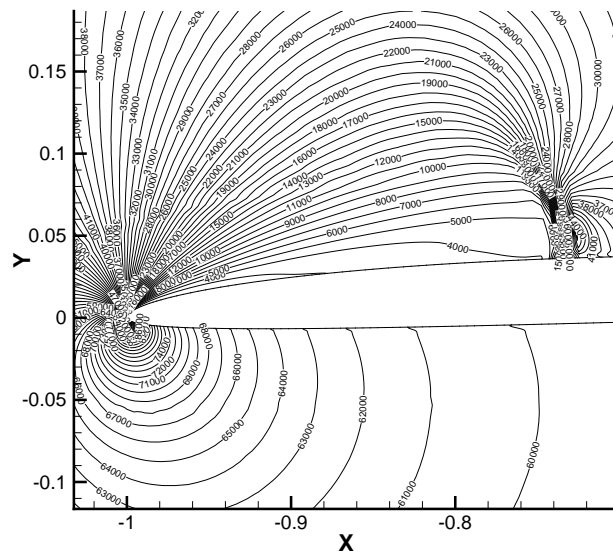
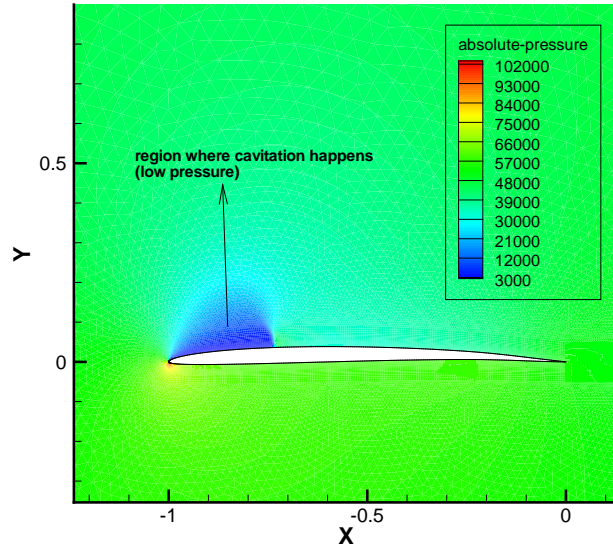


Figure 5.5: Pressure distribution near the cavity bubble predicted by Fluent mixture model for $\sigma = 0.955$: (a) global view of pressure distribution with contour flood, (b) local view of pressure distribution inside and outside the cavity bubble with contour lines, The units of both are Pascal.

5.2 VII BEM simulation

In this section, the application of VII BEM solver to partial-cavitating hydrofoil is discussed. The inviscid solution from BEM solver has long been developed and tested. [Kinnas and Fine 1993] Therefore, the emphasis of this section is put on the viscous correction of the pressure distribution.

5.2.1 Inviscid solution

The formulation of BEM inviscid solution of a partial-cavitation problem can be found in [Kinnas and Fine 1993] and is not repeated here. The basic idea is to treat the cavity surface to be a streamline on which the pressure is equal to the vaporization pressure. The code PCPAN is developed for this application, in which the cavity position is known a priori, the cavitation number, potentials and cavity surface are solved. Once the cavity surface is determined, it is used as part of the compound foil and the inviscid solution is determined on this compound foil.

For a proper comparison with Fluent result, the same cavity position as Fluent needs to be applied in the BEM solver. In this case, a cavity length of 0.27 which starts at the leading edge of the foil is given in PCPAN. Figure 5.6 shows the cavity surface predicted by the BEM solver. Also shown in Figure 5.6 is the water volume fraction near the cavity bubble obtained from Fluent. The comparison shows that the cavity surface predicted by BEM solver agrees roughly with the volume fraction contour lines on which $\alpha_{water} = 0.5 \sim 0.55$.

Figure 5.7 shows the pressure distributions predicted from BEM (in-

viscid) and Fluent. As shown in the figure, the cavitating pressure predicted by the BEM solver is very close to that given in Fluent ($\sigma = 0.955$). The only large discrepancy happens near the cavity closure, which is as expected. The BEM theory applies a cavity termination model that the velocity (i.e. pressure) in the transition zone (a small distance near the cavity closure) departs from its constant value according to a prescribed law. [Lemonnier and Rowe 1988] While Fluent does not need a cavity termination model since RANS mixture model is applied. It is impossible for these two methods to be consistent at the cavity closure.

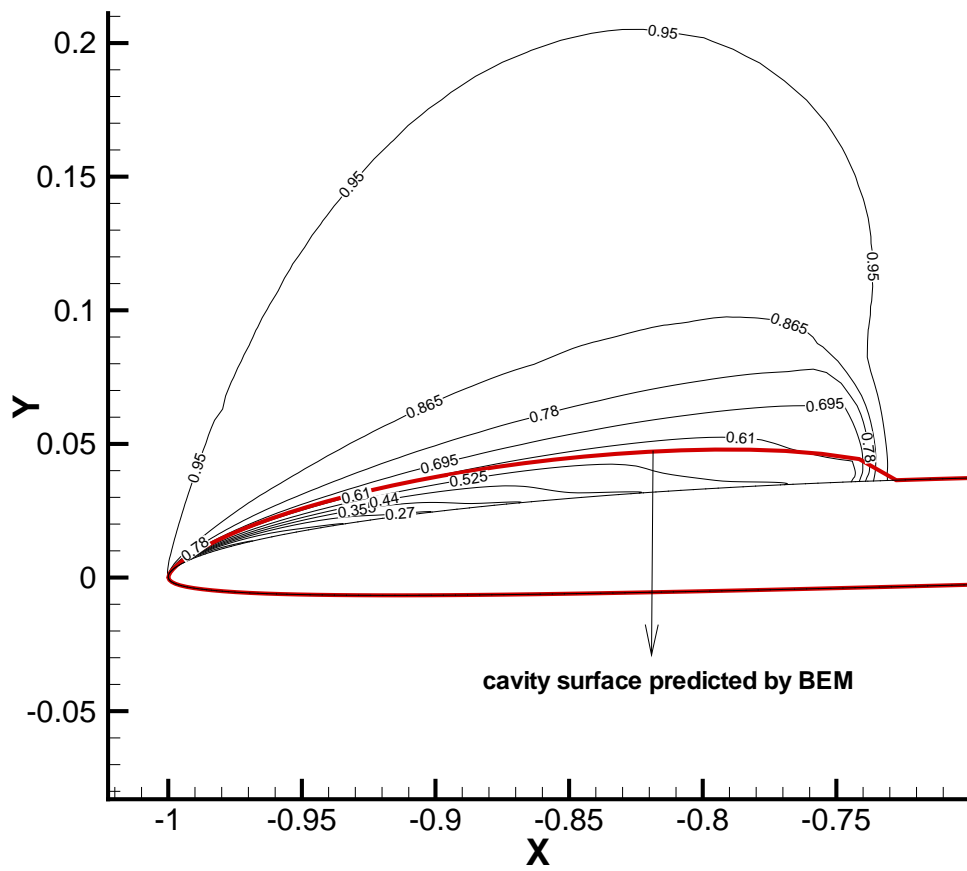


Figure 5.6: Cavity surface predicted by BEM solver and volume fraction predicted by Fluent for $\sigma = 0.955$

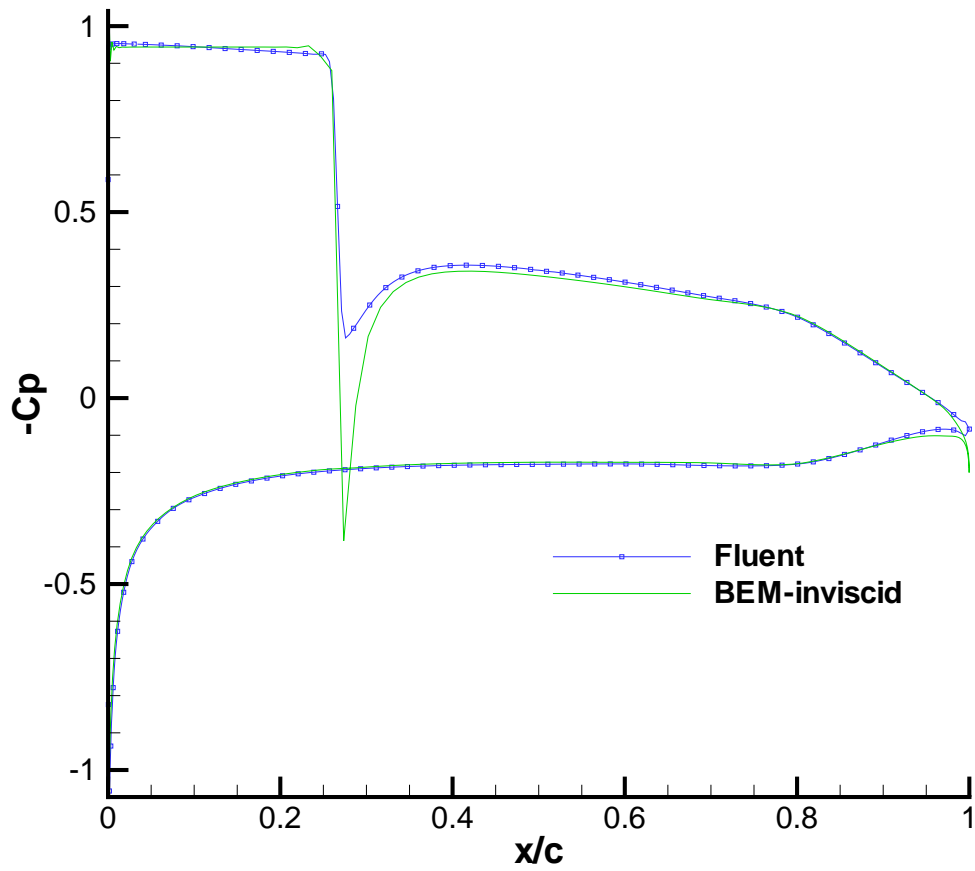


Figure 5.7: Pressure distributions predicted by BEM (inviscid) and Fluent, the result of “BEM-inviscid” is obtained by running CAV2DBL (inviscid) on the compound foil obtained from PCPAN

5.2.2 Viscous solution

In this section, the viscous solution through coupling XFOIL with BEM is discussed. XFOIL is applied on the compound foil (original foil plus cavity surface) directly, which creates a problem that the viscous cavitating pressure fails to be a constant. Three correction schemes are developed to eliminate the negative effects of XFOIL.

5.2.2.1 Original viscous solution

XFOIL is applied on the compound foil directly and the pressure distribution is shown in Figure 5.8. We can observe that viscosity has two effects on the cavitating pressure. First, the cavitation pressure increases by a finite value; second, it somehow perturbs the constant cavitation pressure. These two effects are due to the reason that the cavity surface is treated as a non-slip wall, which is non-physical and different with Fluent mixture model. Three schemes are developed for “correcting” the viscous pressure distribution, which are discussed below.

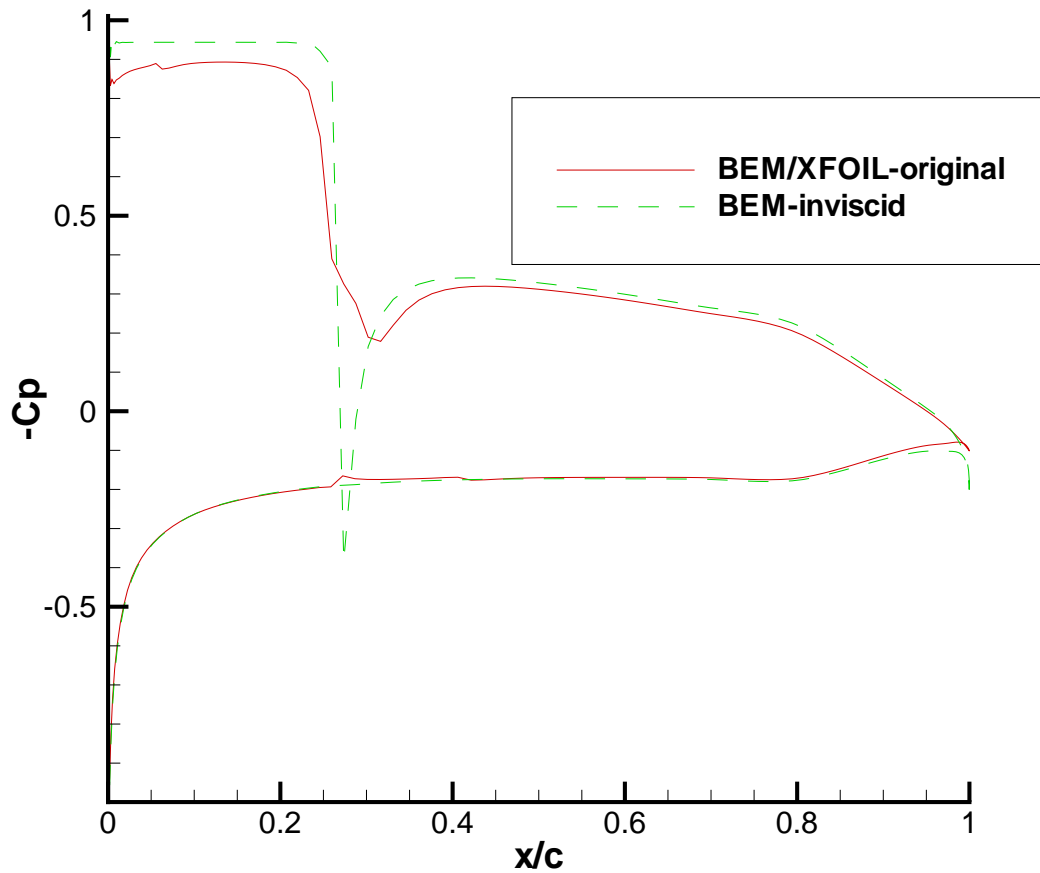


Figure 5.8: Viscous solution by applying XFOIL on top of the compound foil directly, the result of BEM/XFOIL-original is obtained by running CAV2DBL (viscous) on the compound foil obtained from PCPAN

5.2.2.2 Correction scheme I

The correction scheme I is developed for eliminating the effect of pressure perturbation” introduced by XFOIL. This scheme was first developed in [Kinnas et al. 1994]. Its formulation is included here for the sake of completeness.

The effect of viscosity on the inviscid flow can be accounted via the blowing sources, $\hat{\sigma}$, which are defined as:

$$\hat{\sigma} = \frac{d(U_e \delta^*)}{ds} \quad (5.5)$$

Where U_e is the edge velocity and δ^* is the displacement thickness. The presence of the blowing sources will modify Green’s formula equation, when applied on the foil surface, as follows:

$$\frac{\phi^v}{2} = \int_S \left[G(-\vec{U}_\infty \cdot \vec{n}) ds - \phi^v \frac{\partial G}{\partial n} \right] ds - \int_W \Delta \phi_W^v \frac{\partial G}{\partial n} ds + \int_{SUW} \hat{\sigma} G ds \quad (5.6)$$

When applying XFOIL on the compound foil, the introduction of blowing source is the reason for changing the cavitation pressure. To eliminate the perturbation effects on pressure, we need to find a “new” cavity shape on which a “new” dynamic boundary condition is satisfied. Suppose ϕ^{cor} and σ^{cor} are the “correct” perturbation potential and cavitation number, “NL” stands for the compound foil predicted by BEM inviscid theory, the “new” dynamic boundary condition on the cavity is given as

$$\frac{\partial \phi^{cor}}{\partial s} + \vec{U}_\infty \cdot \vec{s}^{NL} = U_\infty \sqrt{1 + \sigma^{cor}} \quad (5.7)$$

On the wetted foil, considering the blowing source strength, a “new” kinematic boundary condition is satisfied:

$$\frac{\partial \phi^{cor}}{\partial n} = -\vec{U}_\infty \cdot \vec{n} + \hat{\sigma}^{NL} \quad (5.8)$$

Equations (5.7) and (5.8) take the same form as a partial cavitation problem for which the cavity length is known a priori, by adding the blowing source $\hat{\sigma}^{NL}$ to $-\vec{U}_\infty \cdot \vec{n}$. We thus treat the correction problem as a cavity problem (applied on the compound foil) and determine ϕ^{cor} and σ^{cor} . The new values of $\frac{\partial \phi^{cor}}{\partial n}$ on the cavity are also determined at each iteration. The cavity shape then needs to be corrected by h^{cor} , defined normal to the original cavity shape. If \vec{n}^{cor} is the unit vector normal to the correct cavity shape, the following kinematic boundary condition must be satisfied when the iteration converges:

$$[\nabla \phi^{cor} + \vec{U}_\infty] \cdot \vec{n}^{cor} = \hat{\sigma}^{NL} \quad (5.9)$$

The normal vector, to the first order in h^{cor} , can be given as:

$$\vec{n}^{cor} = \vec{n}^{NL} - \frac{dh^{cor}}{ds} \vec{s}^{NL} \quad (5.10)$$

Combining equations (5.9) and (5.10) gives the following equation for updating cavity surface after each iteration:

$$U_\infty \sqrt{1 + \sigma^{cor}} [1 - f(x)] \frac{dh^{cor}}{ds} = \frac{\partial \phi^{cor}}{\partial n} + \vec{U}_\infty \cdot \vec{n}^{NL} - \hat{\sigma}^{NL} \quad (5.11)$$

Where $f(x)$ is a function used for the cavity termination model, which is nonzero only on the transition zone to give a prescribed pressure distribution.

After the “correct” cavity shape is found, Equation (5.6) is applied on the “new” compound foil, and the “correct” viscous pressure is obtained. However, a problem still exists that after the new compound foil is obtained, the blowing sources will change correspondingly. Therefore, iterations are needed until pressure distribution remains unchanged compared to the last iteration. Figure 5.9 shows the pressure distributions from the first and second iterations. The difference is so small that the procedure of iteration is neglected.

Also shown in Figure 5.9 is that the “perturbation” of viscous cavitating pressure is eliminated. However, correction I still treats the cavity surface as a non-slip wall, which makes the viscous cavitating pressure lower than that in Fluent mixture model.

The procedure for applying this scheme is outlined as follows:

- (1) PCPAN: Find the inviscid cavity surface on the foil.
- (2) CAV2DBL: Apply viscous solver on the compound foil and calculate the strengths of blowing sources.
- (3) PCPAN: Find the “new” cavity surface, as described above.
- (4) CAV2DBL: Solve equation (5.6) to get the viscous pressure on the foil, by adding the blowing source term.

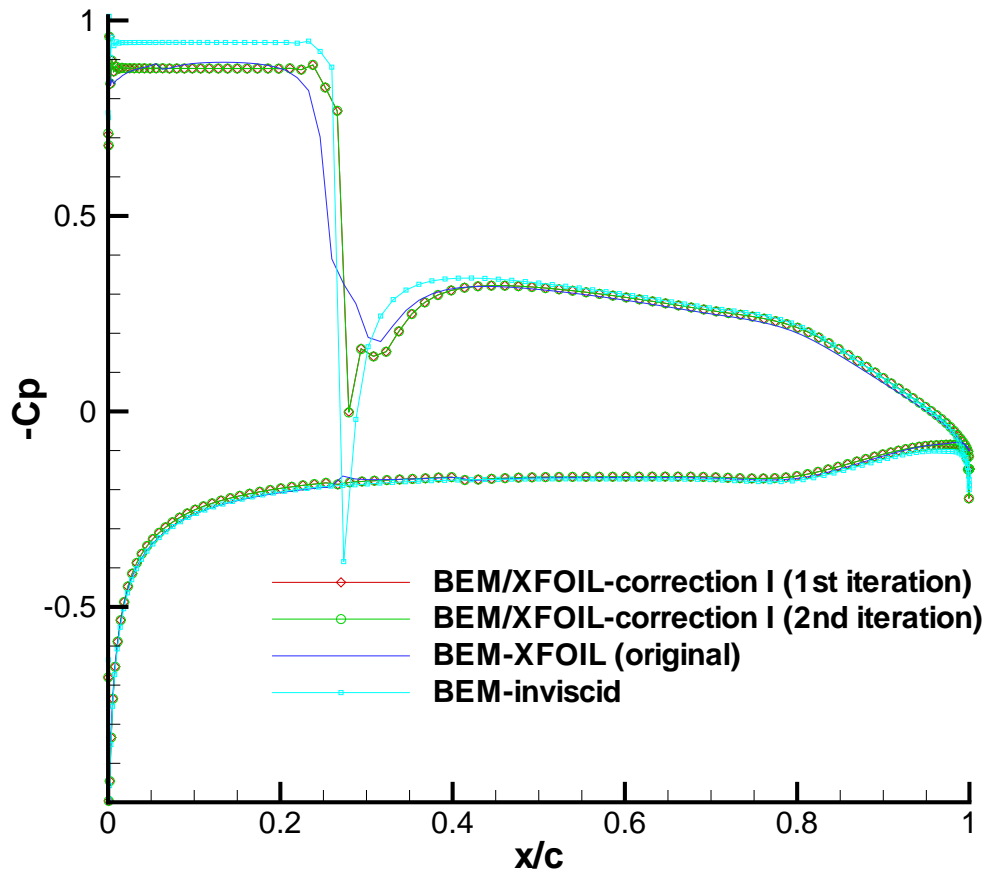


Figure 5.9: Viscous pressure distribution by applying correction I (Results from first and second iterations are shown)

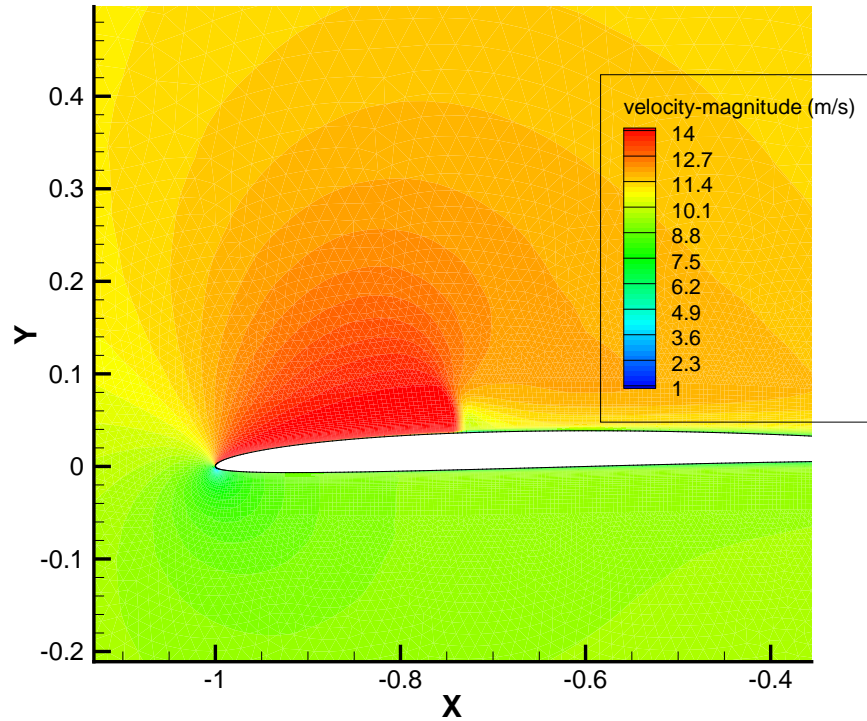


Figure 5.10: Mixture velocity near the cavity predicted by Fluent mixture model

5.2.2.3 Correction scheme II

The only difference between scheme I and scheme II is that in scheme II, the strengths of blowing sources on the cavity surface are set to be zero, after XFOIL is applied on the compound foil. The reason for doing this is that the cavity surface is assumed to be inviscid. In Fluent mixture model, the velocity near the cavity surface is high due to the locally low pressure, as shown in Figure 5.10.

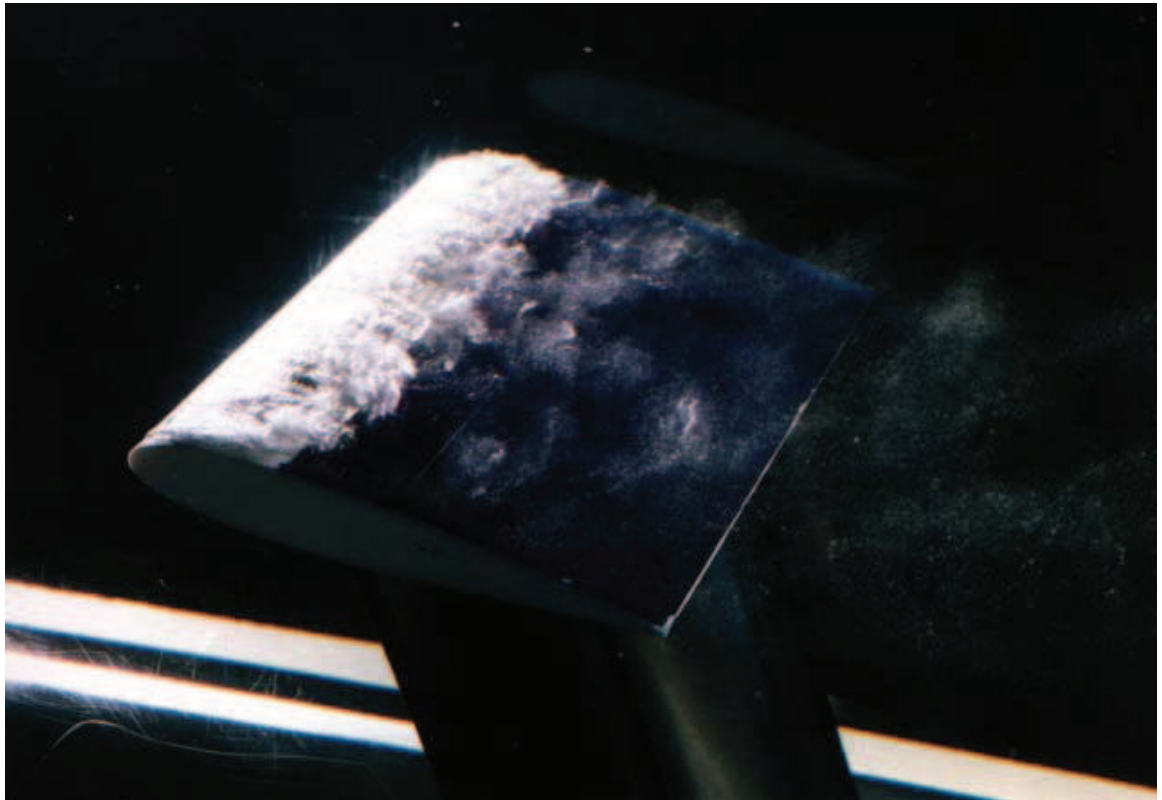


Figure 5.11: A hydrofoil with sheet cavitation (The picture is taken in University of Tokyo and can be found online at <http://www.fluidlab.naoe.t.u-tokyo.ac.jp/Research/CavPictures/index.html.en>)

Physically, there is an interfacial boundary layer existing at the cavity surface, which is out of the modeling scope of BEM. However, experimental result shows that the water vapor convected with the flow velocity. Figure 5.11 shows a picture of a hydrofoil with sheet cavitation in experiment. Instead of using a viscous wall, it is more reasonable to model the cavity surface as inviscid in BEM because the velocity near the cavity surface is physically nonzero.

Figure 5.12 shows the viscous pressure distribution obtained from Correction scheme II, where the cavitating pressure raises to the inviscid value. However, since the strengths of the blowing sources on the cavity are forced to be zero after XFOIL is applied on the whole compound foil, this scheme creates a problem that the boundary layer thickness jumps from zero to a finite value at the end of the cavity. (The strength of the blowing source starts from zero to a large value.) This negative effect is compensated by artificially putting an extra source on the last panel of cavity, whose strength is opposite to the one next to it.

This scheme is not a good scheme in the sense that too many things are forced artificially. Although the cavitating pressure is raised to the inviscid value for this case, it is not true for a case with different cavity length.

5.2.2.4 Correction scheme III

In this scheme, the viscous boundary layer is assumed to start at the trailing edge of the cavity on the suction side, as shown in Figure 5.13. Therefore, the cavity surface is treated as inviscid and the cavitating pressure is not updated by XFOIL. The procedures to find the “new” cavity surface, which are used in correction I and II, are not needed here.

Figure 5.14 shows the pressure distribution obtained from this scheme. We can see that only the pressures on the wetted foil (not including the cavity surface) are corrected.

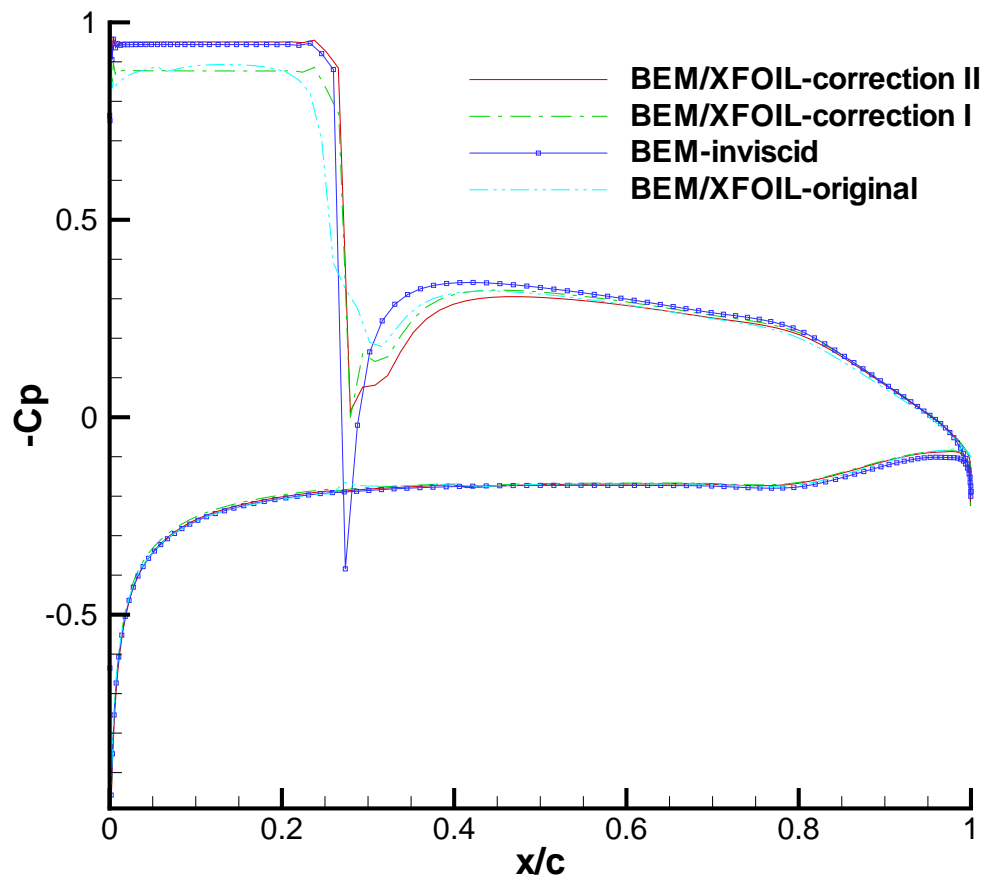


Figure 5.12: Viscous pressure distribution by applying correction II

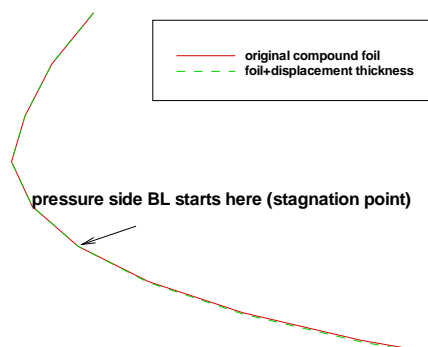
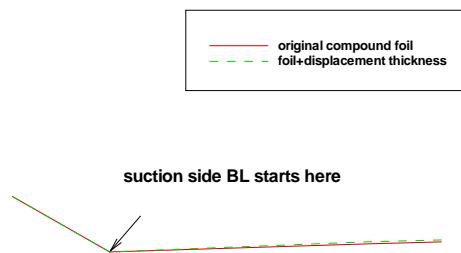
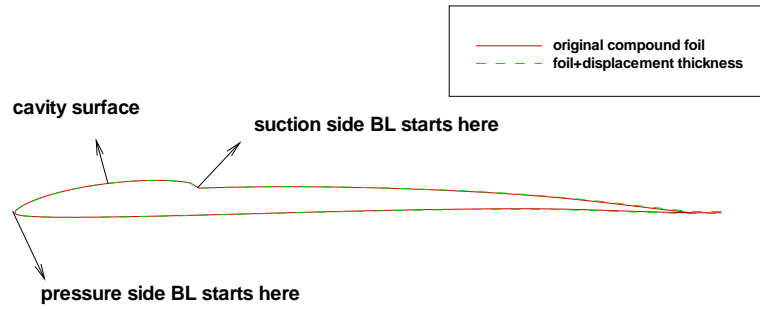


Figure 5.13: Treatment of boundary layer in Correction scheme III

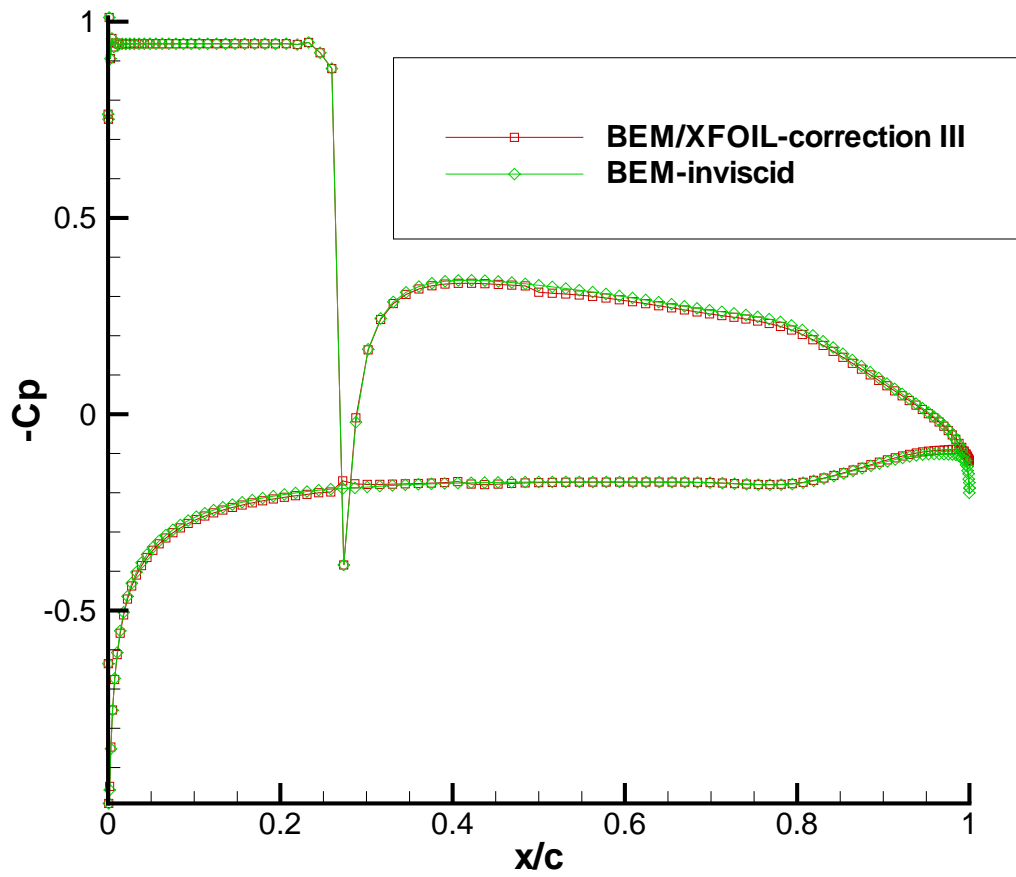


Figure 5.14: Viscous pressure distribution by applying correction III

5.2.3 Summary of all schemes

As a summary, Figure 5.15 shows the comparison of all BEM schemes and Fluent result. In term of cavitating pressure, the BEM inviscid scheme, viscous correction scheme II, III and Fluent mixture model give very similar results. The only large discrepancy exists at the cavity closure, which is due to the fact that different treatments of cavity closure are applied.

These schemes are then applied to the same hydrofoil with smaller cavitation number. Specifically, the operating (ambient) pressure in Fluent is set to be 40000 Pa, which gives a cavitation number $\sigma = \frac{p_\infty - p_v}{(1/2)\rho v^2} = 0.754$. Figure 5.16 shows the Fluent result of pressure distribution near the foil. The cavity length for this case is about 0.74, which is, as expected, much larger than the previous case. However, the similar behavior of pressure variance can be observed inside and outside the cavity bubble. It should be noted that the unsteady solver of Fluent is also used in this case, and it is found that the cavity fluctuations are not significant. This is contrary to experimental evidence where partial cavities exceeding 50% of the chord are very unstable [Tulin and Hsu 1980]. Figure 5.17 shows the water volume fraction inside and outside the cavity bubble and the cavity surface predicted by BEM solvers. Similar as the previous case, the cavity surface predicted by BEM solver agrees roughly with the volume fraction contour lines on which $\alpha_{water} = 0.55 \sim 0.6$.

The predicted pressure distributions on the foil by both Fluent and BEM solvers are shown in Figure 5.18. Again, the cavitating pressure predicted by BEM inviscid theory agrees well with Fluent result. However, relatively

larger discrepancy still exists near the cavity closure region. Also, for this case, correction scheme II fails to give a good correlation with Fluent in term of the cavitating pressure.

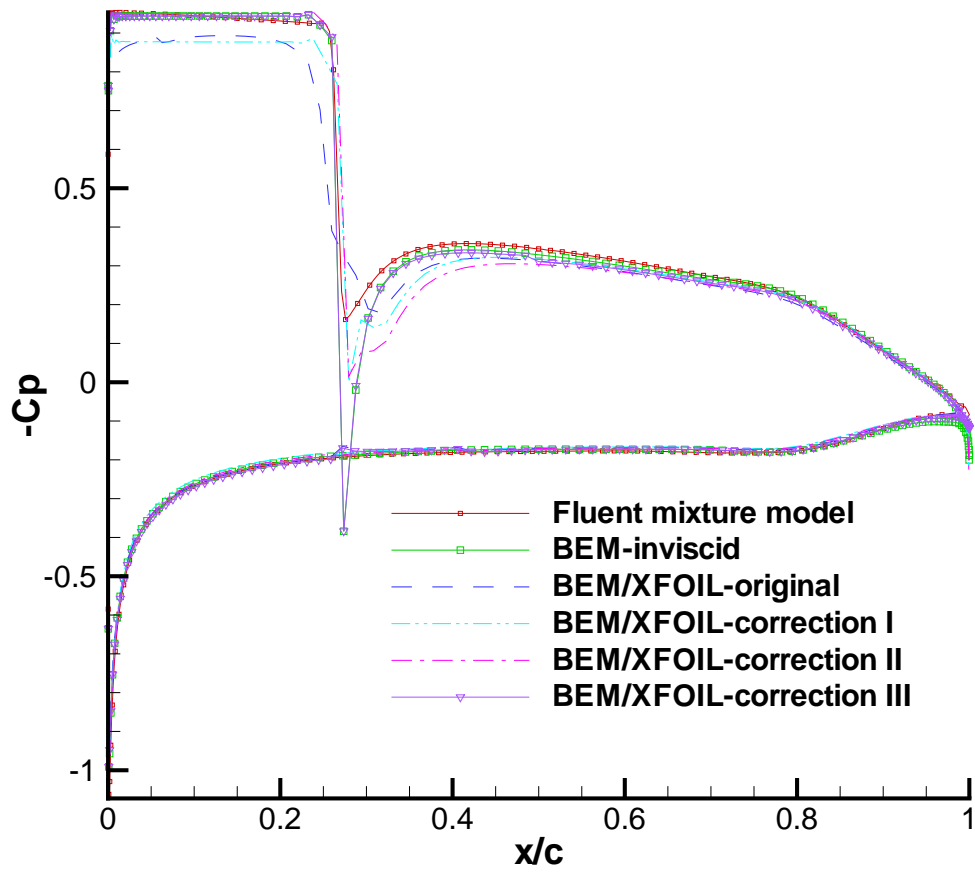


Figure 5.15: Summary of pressure distributions predicted by all schemes for $\sigma = 0.955$

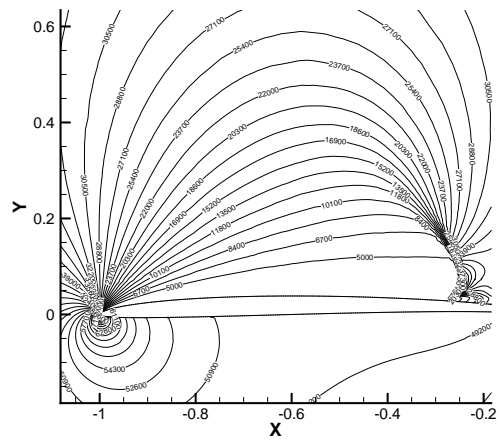
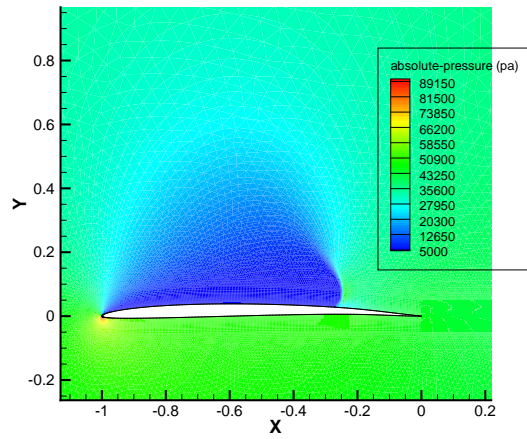


Figure 5.16: Pressure distribution near the cavity bubble predicted by Fluent mixture model for $\sigma = 0.754$: (a) global view of pressure distribution with contour flood, (b) local view of pressure distribution inside and outside the cavity bubble with contour lines, The units of both are Pascal.

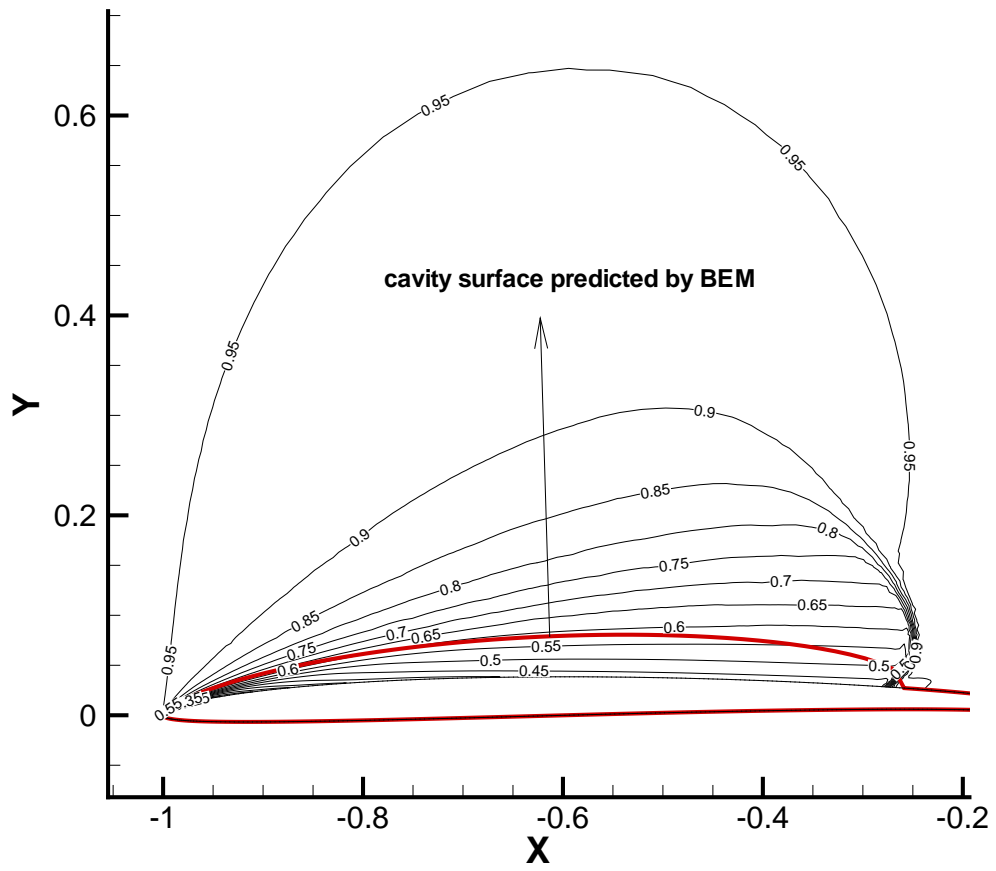


Figure 5.17: Cavity surface predicted by BEM solver and volume fraction predicted by Fluent for $\sigma = 0.754$

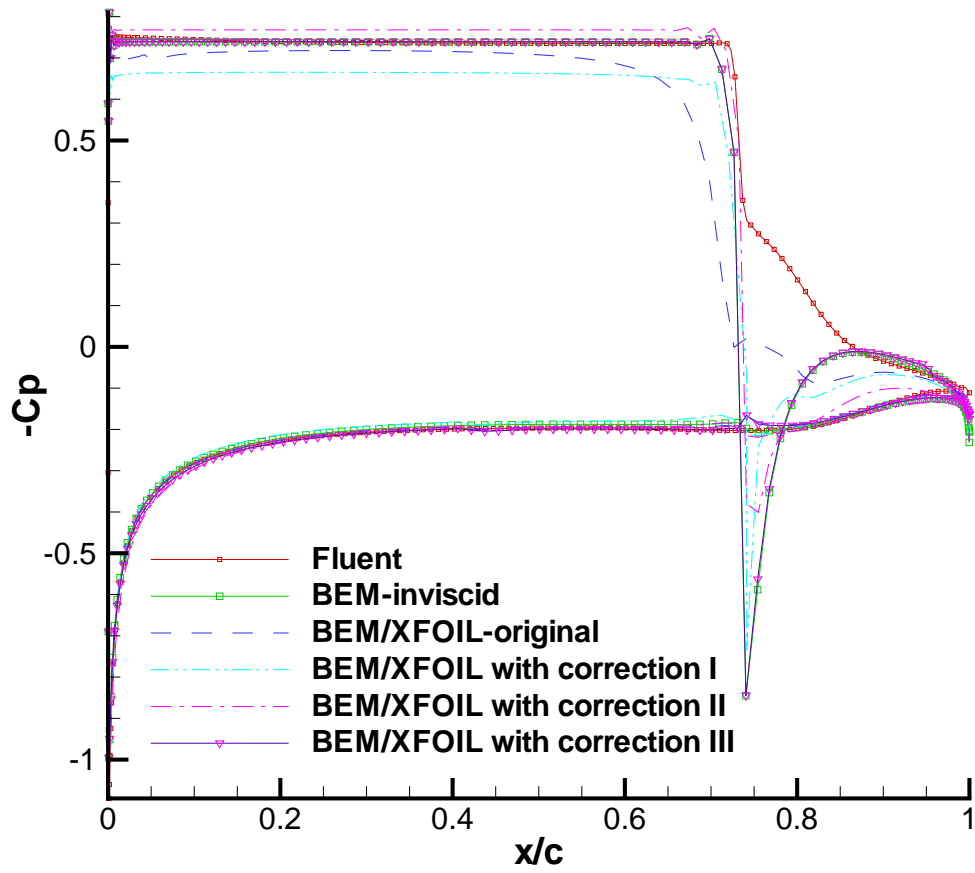


Figure 5.18: Summary of pressure distributions predicted by all schemes for $\sigma = 0.754$

Chapter 6

Conclusions and recommendations

6.1 Conclusions

This thesis can be divided into two parts.

In the first part of the thesis, the viscous/inviscid interactive approach and its application to hydrofoils and propellers with non-zero trailing edge thickness are addressed. The investigation starts from a 2D hydrofoil. Two kinds of iteration methods are coupled with the VII BEM solver to find a non-lifting extension behind the finite trailing edge, which is used as an approximation of the flow separation zone. The flow around a hydrofoil with non-zero trailing edge thickness is modeled in Fluent and by the current approach. The correlation of the results show that the current methods provide acceptable results, with the computational cost reduced significantly. The two degrees of freedom iteration method and the cavity-like scheme provide more “accurate” results (relative to those from Fluent) than the one degree of freedom iteration method. The one and two degrees of freedom models are then extended to 3D propeller flows. They are first coupled with the BEM inviscid solution. The predicted K_Q is close to the experimental data but the predicted K_T is lower. The results are no better than those from an approximation where

the aft part of the thickness of the foil is altered so that it closes at the trailing edge. Considering that viscous effects are important in flow separation, the one degree of freedom model with non-lift condition is then coupled with the VII BEM solver, and results closer to those measured are obtained.

In the second part of the thesis, the application of the inviscid/viscous interactive approach to partial-cavitating hydrofoils are addressed. A RANS solver (Fluent) coupled with a mixture model is first used to model the flow around a hydrofoil with partial-cavitation at given cavitation numbers. The hydrofoil with the same cavity extent is then modeled using BEM. The cavitating pressure predicted by Fluent agrees well with the BEM inviscid theory. However, coupling of BEM with XFOIL introduces viscous effects, which increase and “perturb” the cavitation pressure. Three schemes are developed to include the effects of viscosity in BEM and results comparable to those of Fluent are obtained. Finally, the predicted pressure distributions by Fluent and BEM have a relatively larger discrepancy near the cavity closure region, especially for a long cavity length. This is due to the cavity termination model used in BEM solver. It should be noted that the BEM/XFOIL with the effects of the boundary layer fully included would produce a smaller cavity than that predicted by Fluent. At this point we do not know which prediction is correct.

The main contributions of the research are:

- The present work provides a method to predict the viscous flow around hydrofoils and propellers with non-zero trailing edge thickness. In recent

years, there are an increasing number of propellers which are designed to have a finite trailing edge, including some super-cavitating and fully submerged propellers. Previously Two approaches were used to deal with a finite trailing edge. The first one is to force the section to close at the trailing edge, which is the approximation 1 in present work, and is found to fail to give reasonable results. The second method assumes an arbitrary separation zone on which the pressure is equal to the vapor pressure, which is non-physical and not applied to fully wetted hydrofoils and propellers. The present method gives better results than the previous approaches and can be used commonly for the treatment of non-zero trailing edge thickness.

- The flow around a partial-cavitating hydrofoil is modeled using the VII BEM solver and a RANS mixture model. A correlation study between these two methods was performed.

6.2 Recommendations

One improvement and two applications of the current scheme are recommended for future work.

- Improvement of viscous results for a closed section: There are three deficiencies for the viscous part of CAV2DBL and PROPCAV. (1) For some cases, the results fail to converge by increasing the number of elements. However, this feature does not exist in the original version of XFOIL.

Fixing this problem could help improve the convergence behavior of the VII BEM solver in 3D. (2) For some non-standard 2D sections, there are some discrepancies between the results from CAV2DBL and XFOIL. Looking into these discrepancies might help to improve the performances of the viscous parts of CAV2DBL and PROPCAV. (3) In 3D application (PROPCAV), the cross flow is neglected based on an assumption that it is small enough. This assumption is not always true and it is worthwhile to find a way to include the effect of cross flow.

- Backing condition: Treatment of backing condition involves two difficulties. (1) The boundary layer theory fails at the sharp leading edge and it is hard to find the stagnation point even for the inviscid theory. (2) Flow separates at the rounded trailing edge and the position of detachment position of the boundary layer is unknown. The problem at the leading edge might be avoided by rounding the leading edge by a small arc, which is consistent with the real case. Sharp leading edges are never applied on propeller because they are easily damaged. For the problem at the trailing edge, applying the current approach might help to overcome the difficulty. A separation zone is needed behind the round trailing edge, as shown in Figure 6.1. However, determining the starting position of separation remains to be a problem. The shape factor H might help to solve this problem. [Simpson 1989] suggests that for near-equilibrium flows satisfying the Coles velocity profile model, intermittent transitory detachment occurs at $H = 2.70$.

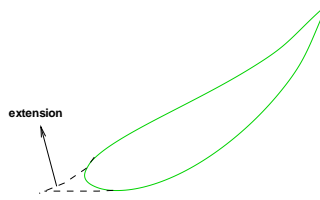


Figure 6.1: Separation zone for backing condition

- Super cavitation: Most super-cavitating propellers have finite trailing edges. In a super-cavitating propeller, there are some strips near the hub where only partial cavitation happens. The previous treatment is to use an arbitrary separation zone on which the pressure is set to be vapor pressure, which is non-physical. The current approach can be applied to solve this problem and might help to improve the prediction of the performances of such propellers.

Bibliography

- Brewer, W. H. and Kinnas, S. A. (1997). Experiment and viscous flow analysis on a partially cavitating hydrofoil. *Journal of Ship Research*, 41(3):161–171.
- Coney, W. B. (1989). Some notes on the calculation of viscous effects on lift. Technical report, Technical Report 89-8, Department of Ocean Engineering, Massachusetts Institute of Technology.
- Drela, M. (1989). XFOIL- An analysis and design system for low Reynolds number airfoils. *Low Reynolds Number Aerodynamics*, pages 1–12.
- Fine, N. E. and Kinnas, S. A. (1993). A boundary element method for the analysis of the flow around 3-d cavitating hydrofoils. *Journal of Ship Research*, 37:213–224.
- Fluent, F. (2007). Fluent 6.3 User’s Manual. *Fluent Inc., Lebanon, NH, USA*.
- Groves, N. C. and Chang, M. S. (1984). A differential method for three dimensional laminar and turbulent boundary layers of rotating blades. In *The Fifteenth ONR Symposium on Naval Hydrodynamics*, Hamburg, Germany.
- Hufford, G., Drela, M., and Kerwin, J. (1994). Viscous flow around marine propellers using boundary-layer strip theory. *Journal of ship research*, 38(1):52–61.

- Jessup, S. D. (1989). *An Experimental Investigation of Viscous Aspects of Propeller Blade Flow*. PhD thesis, The Catholic University of America.
- Keller, A. and Rott, H. (1997). The Effect of Flow Turbulence on Cavitation Inception. In *ASME Fluids Engineering Division Summer Meeting, Vancouver*.
- Kerwin, J. E., Kinnas, S. A., Lee, J.-T., and Shih, W.-Z. (1987). A surface panel method for the hydrodynamic analysis of ducted propellers. *Transactions of Society of Naval Architects & Marine Engineers*, 95.
- Kinnas, S. and Fine, N. (1991). Non-Linear Analysis of the Flow Around Partially or Super-Cavitating Hydrofoils by a Potential Based Panel Method. In *Boundary Integral Methods-Theory and Applications, Proceedings of the IABEM-90 Symposium, Rome, Italy, October 15-19, 1990*, pages 289–300, Heidelberg. Springer-Verlag.
- Kinnas, S. A. and Fine, N. E. (1992). A nonlinear boundary element method for the analysis of unsteady propeller sheet cavitation. In *Nineteenth Symposium on Naval Hydrodynamics*, pages 717–737, Seoul, Korea.
- Kinnas, S. A. and Fine, N. E. (1993). A numerical nonlinear analysis of the flow around 2-d and 3-d partially cavitating hydrofoils. *Journal of Fluid Mechanics*, 254:151–181.
- Kinnas, S. A. and Hsin, C.-Y. (1992). A boundary element method for the

- analysis of the unsteady flow around extreme propeller geometries. *AIAA Journal*, 30(3):688–696.
- Kinnas, S. A., Mishima, S., and Brewer, W. H. (1994). Nonlinear analysis of viscous flow around cavitating hydrofoils. In *Twentieth Symposium on Naval Hydrodynamics*, pages 446–465, University of California, Santa Barbara.
- Kudo, T. and Kinnas, S. A. (1995). Application of unsteady vortex/source lattice method on supercavitating propellers. In *Twenty-Fourth American Towing Tank Conference*, pages 33–40, Texas A&M University.
- Kudo, T. and Ukon, Y. (1994). Calculation of supercavitating propeller performance using a vortex-lattice method. In *Second International Symposium on Cavitation*, pages 403–408, Tokyo, Japan.
- Lee, H. S. and Kinnas, S. A. (2004). Application of boundary element method in the prediction of unsteady blade sheet and developed tip vortex cavitation on marine propellers. *Journal of Ship Research*, 48(1):15–30.
- Lee, H. S. and Kinnas, S. A. (2005). Unsteady Wake Alignment for Propellers in Nonaxisymmetric Flows. *Journal of Ship Research*, 49(3).
- Lee, H. S. and Kinnas, S. A. (2006). Prediction of cavitating performance of ducted propeller. In *The Sixth International Symposium on Cavitation*, Wageningen, The Netherlands.

- Lee, J.-T. (1987). *A Potential Based Panel Method for The Analysis of Marine Propellers in Steady Flow*. PhD thesis, Department of Ocean Engineering, Massachusetts Institute of Technology.
- Lemonnier, H. and Rowe, A. (1988). Another approach in modelling cavitating flows. *Journal of Fluid Mechanics*, 195.
- Lighthill, M. (2006). On displacement thickness. *Journal of Fluid Mechanics Digital Archive*, 4(04):383–392.
- Nishida, B. and Drela, M. (1995). Fully simultaneous coupling for three-dimensional viscous/inviscid flows. In *AIAA Applied Aerodynamics Conference, 13 th, San Diego, CA*, pages 355–361.
- Rhee, S. H., Kawamura, T., and Li, H. Y. (2005). Propeller cavitation study using an unstructured grid based navier-stokes solver. *Journal of Fluids Engineering*, 127:986–994.
- Rice, J. (1991). Investigation of a two-dimensional hydrofoil in steady and unsteady flows. Master’s thesis, Massachusetts Institute of Technology, Dept. of Ocean Engineering.
- Russel, A. (1958). Aerodynamics of wakes, existence of unsteady cavities. *Engineering*, 186:pp. 701–702.
- Simonin, O. and Viollet, P. (1990). Prediction of an oxygen droplet pulverization in a compressible subsonic coflowing hydrogen flow. In *Numerical*

methods for multiphase flows: presented at the 1990 Spring Meeting of the Fluids Engineering Division, held in conjunction with the 1990 Forum of the Canadian Society of Mechanical Engineers, University of Toronto, Toronto, Ontario, Canada, June 4-7, 1990, page 73. Amer Society of Mechanical.

Simpson, R. L. (1989). Turbulent boundary-layer separation. *Annual Review of Fluid Mechanics*, 21(1):205–232.

Singhal, A., Athavale, M., Li, H., and Jiang, Y. (2002). Mathematical basis and validation of the full cavitation model. *Journal of Fluids Engineering*, 124:617–624.

Singhal, A., Vaidya, N., and Leonard, A. (1997). Multi-dimensional simulation of cavitating flows using a PDF model for phase change. In *ASME Paper FEDSM97-3272, The 1997 ASME Fluids Engineering Division Summer Meeting*.

Sun, H. (August, 2008). *Performance Prediction of Cavitating Propulsors using a Viscous/Inviscid Interactive Method (also UT-OE Report No. 08-2)*. PhD thesis, Ocean Engineering Group, Department of Civil, Architectural and Environmental Engineering, University of Texas at Austin, Austin.

Sun, H. and Kinnas, S. A. (2008). Performance prediction of cavitating water-jet propulsors using a viscous/inviscid interactive method. In *Proceedings, 2008 SNAME Annual Meeting and Ship Production Symposium*, Houston, USA.

- Tulin, M. and Hsu, C. (1980). New applications of cavity flow theory. In *Proceedings: 13th Symposium on Naval Hydrodynamics*.
- Watanabe, M. and Prosperetti, A. (1994). The effect of gas diffusion on the nuclei population downstream of a cavitation zone. In *Cavitation and gas-liquid flow in fluid machinery and devices: presented at the 1994 ASME Fluids Engineering Division Summer Meeting, Lake Tahoe, Nevada, June 19-23, 1994*, page 211. American Society of Mechanical Engineers.
- Young, Y. L. and Kinnas, S. A. (2003a). Numerical analysis of surface piercing-propellers. In *Propellers/Shafting '03 Symposium*, pages 1–20 (paper No. 4), Virginia Beach, VA. The Society of Naval Architects & Marine Engineers.
- Young, Y. L. and Kinnas, S. A. (2003b). Numerical modeling of supercavitating propeller flows. *Journal of Ship Research*, 47(1):48–62.

Vita

Yulin Pan was born on February 21st, 1985 in Yantai, Shandong Province, P.R. China, the son of Zhigang Pan and Peixuan Ma. He studied in the No. 2 High School of Yantai from 2000 to 2003. In the fall of 2003, he entered the Department of Naval Architecture and Ocean Engineering at Huazhong University of Science and Technology, Wuhan, Hubei. After receiving his Bachelor of Engineering Degree in July, 2007, he joined the University of Texas at Austin for his Master's education, focusing on Ocean Engineering.

Permanent address: 17 Xinyuan Road
Laishan District, Yantai, Shandong Province
264003
People's Republic of China

This thesis was typeset with L^AT_EX[†] by the author.

[†]L^AT_EX is a document preparation system developed by Leslie Lamport as a special version of Donald Knuth's T_EX Program.